

**UNIVERSITÀ
DEGLI STUDI
DI PADOVA**

UNIVERSITÀ DEGLI STUDI DI PADOVA

Sede Amministrativa: Università degli Studi di Padova
Dipartimento di Ingegneria Industriale

Scuola di Dottorato di Ricerca in Ingegneria Industriale
Indirizzo: Ingegneria Chimica, dei Materiali e Meccanica
Ciclo XXVIII

Quality control of freeform parts at elevated temperature

Direttore della Scuola: Prof. Paolo Colombo
Supervisore: Prof. Enrico Savio
Correlatori: Prof. Dr. Claus Keferstein,
Prof. Simone Carmignato

Dottorando: Alexander Schöch

To my parents

Acknowledgements

This thesis resulted from my research between 2012 and 2015, performed in Italy and Switzerland during my time at the University of Padua and as a research associate at the University of Applied Sciences NTB, respectively.

I am deeply grateful to my advisor Prof. Enrico Savio for making this thesis possible, for enlightening discussions, for motivating encouragement and for his invaluable years-long support. My special thanks go to Prof. Dr. Claus Keferstein for encouraging me to start a Ph.D. and for evaluating several initial ideas. Moreover, I want to thank him and Prof. Simone Carmignato for encouraging discussions and for co-supervising my work. Also, I want to express my gratitude to the two professors who evaluated this work as part of the requirements for the European Doctorate, namely, Prof. Dr. Leonardo De Chiffre and Prof. Dr. Klaus Frick. I wish to express my appreciation to Prof. Andrea Ghiotti and Prof. Stefania Bruschi from the University of Padua for very inspiring discussions and their support. I thank my colleagues Alessandro Salvadori, Fabrizio Medeossi and Enrico Simonetto for the great working atmosphere and the motivating, informal knowledge transfer. Thanks go to my colleagues from the University of Applied Sciences NTB, namely, Marc Honegger, Andreas Brunn, Mehmet Demirel, Patric Perez, Sabine Linz-Dittrich, Michael Kahl, Christoph Battaglia and Roman Kuster for interdisciplinary exchange of ideas and personal motivation. For their frequent support and valued expert knowledge, I want to thank Prof. Dr. Carlo Bach, Prof. Dr. Michael Marxer, Prof. Dr. Nikolaus Herres and Prof. Dr. Andreas Ettemeyer.

In private sphere, I thank my fabulous girlfriend Isabelle Dorsch for her motivation and endurance during these years. Finally, I want to thank my parents Silvia and Günter for everything. In this context especially for their help, patience, trust and encouragement during my Ph.D. studies.

Abstract

Modern industries operate under high cost pressure coupled with ever increasing demands on their processes and products. Production processes are e.g. increasingly complex while the permitted tolerances, batch sizes and time-to-market times decrease. These partly contradictory trends require sophisticated production processes with advanced strategies for quality assurance and process control. The aim of this work is to analyse such a complex, multi-stage production process, the production of turbine blades, in terms of quality, process adjustment for small batch sizes and cost.

In the considered process, turbine blades are manufactured by forging and are cooled down in calm air to ambient temperature for subsequent machining. This significantly impedes quality control during the process due to the prevailing elevated temperature of workpieces and the consequential need for several hours of cooling before measurements can be performed. Due to small batch sizes, forging of one batch is completed within hours, possibly before quality control at the first produced workpiece takes place. This results in late verification of tolerances when all workpieces are already produced and potentially violate their tolerance limits. After forging, the focus is on verification of dimensional forging tolerances. These asymmetric tolerances allow only for additional material that is to be subsequently removed by machining. Equivalent asymmetry is encountered in the incurred cost, positive deviations increase machining cost while negative deviations cause high cost due to classification as defective.

Analysis of the production process indicated substantial process optimisation opportunities by quality control during the process. However, not only measurements at elevated workpiece temperature have to be performed, also the cooling influence on the workpiece must be predicted to make early conformance statements. This is especially crucial for the thin freeform aerofoil of turbine blades that is subject to complex geometrical distortions during cooling. Additionally, if the process parameters shall be adjusted according to measurement results, appropriate methods to account for asymmetric tolerances and cost are necessary. Adjusting process parameters during the ramp-up of a batch is necessary

to setup the process for the specific product. Such adjustments slow down the production, can be costly and may require a considerable period of the production time, especially for small batches. Therefore, a method shall be developed to determine when to stop initial adjustments.

In this work, a multisensor light sectioning coordinate measuring system for dimensional measurements *at elevated temperature* is presented and discussed. For visualisation and measurand evaluation, an existing heuristic surface reconstruction method is adapted for enhanced surface quality on partly concave freeform workpieces as turbine blades. Its low time complexity enables realtime visualisation during measuring, allowing operators to monitor and qualitatively verify measurement results quickly. Main uncertainty contributors on the system are identified, quantified and, where necessary, corrected. In particular for freeform workpieces, the requirement for improved sensor adjustment is demonstrated. A novel method for sensor adjustment and multisensor registration is proposed, yielding a five times improvement in experiments compared to manual methods.

By the discussed corrections, process adjustment for small batch turbine blade manufacturing becomes feasible. A method to obtain the optimal number of adjustments is available from literature for a specific combination of symmetric cost model and process variation by analytic evaluation of *expected cost*. A novel formulation and appropriate numerical methods are proposed to evaluate expected cost with arbitrary, possibly asymmetric, cost models and process variation models. Based on this formulation, two generalised criteria when to stop adjustments optimally are presented, each exhibiting distinct advantages for specific application cases. Their performance is compared to a state-of-the-art deadband model for process adjustment, yielding down to 90% lower cost for the evaluated cases if measurements are performed during the adjustment phase only. Eventually, a novel comprehensive framework for process adjustment, incorporating the proposed methods, is discussed.

Sommario

Le moderne industrie manifatturiere si trovano ad operare in una condizione di forte stress economico, ma allo stesso tempo con richieste dal mercato sempre più complesse. Ad esempio, se da un lato i processi produttivi aumentano la propria complessità, dall'altro, le tolleranze richieste, le dimensioni dei lotti e il "time-to-market" si riducono sempre più. Questo andamento, per certi versi contraddittorio, richiede l'adozione di processi produttivi sempre più sofisticati e tecniche avanzate per il controllo della qualità e del processo. L'obiettivo di questo lavoro è di analizzare, in un processo produttivo complesso come quello delle palette per turbina, il controllo qualità e l'ottimizzazione di processo per lotti ridotti col fine di abbassare i costi legati alla produzione. Nel processo in analisi, le palette per turbina vengono forgiate a caldo e poi raffreddate in aria calma fino al raggiungimento della temperatura ambiente in modo da poter essere successivamente lavorate tramite macchine a controllo numerico. Le attuali tecnologie di misura rendono possibile il primo controllo dimensionale solo a valle del completo raffreddamento, che può richiedere fino a diverse ore. Date le dimensioni dei lotti tipicamente ridotte, spesso, la forgiatura di un intero lotto viene completata prima che sia stato possibile verificare la geometria del primo pezzo; ciò implica che potenzialmente può essere prodotto un intero lotto fuori tolleranza. Dopo la fase di forgiatura, il controllo dimensionale viene focalizzato alla ricerca dei sovrametalli, che, nel caso siano superiori al valore imposto in fase di progetto comporteranno un aumento dei costi di lavorazione a macchina, diversamente, qualora siano inferiori, porteranno a scartare il pezzo appena prodotto.

A seguito di queste considerazioni si comprende l'importanza di anticipare la fase di controllo qualità, ma per fare ciò, non solo è importante essere in grado di misura ad elevate temperature occorre anche sviluppare dei modelli per la comprensione degli effetti distorsivi indotti dal raffreddamento così da prevedere la geometria finale. Ciò diventa un punto cruciale per le geometrie sottili e "freeform" che caratterizzano la foglia di una palette per turbina. Inoltre, per ottimizzare il processo in base ai risultati delle misurazioni, è necessario comprendere le tolleranze e i costi legati all'ottimizzazione. Infatti, l'ottimizzazione

dei parametri di processo durante le fasi iniziali di produzione di un lotto, essenziali per la corretta lavorazione di un componente, comportano rallentamenti e conseguenti costi. Lotti di ridotte dimensioni ne vengono maggiormente penalizzati. Di conseguenza è necessario sviluppare una procedura per determinare quando valga la pena fermare il processo di ottimizzazione.

In questo lavoro, un sistema di misura basato sulla triangolazione laser per misura dimensionale di pezzi *ad elevata temperatura* viene presentato e discusso. Per ragioni di visualizzazione e misurazione, un algoritmo euristico, per la ricostruzione di superfici a partire da nuvole di punti, è stato adattato per superfici libere e concave come quelle che caratterizzano le palette per turbina. Data la rapidità dell'algoritmo è possibile visualizzare la geometria in contemporanea alla misura, permettendo all'operatore di monitorare qualitativamente l'andamento della misura. Le cause di incertezza principali del sistema di misura sono state identificate, quantificate e, se necessario, corrette. In particolare, nel caso di geometrie tipo "freeform", è stata dimostrata l'importanza di una miglior procedura di settaggio dei sensori. Un nuovo metodo per la taratura di sistemi multisensore è stato sviluppato ed è in grado di garantire tempi di settaggio cinque volte inferiori rispetto ai metodi manuali.

Grazie alle correzioni proposte, l'ottimizzazione di processo per piccoli lotti di palette per turbina diventa possibile. Un metodo per la valutazione del numero ottimale di iterazioni durante il processo di ottimizzazione è disponibile in letteratura per una specifica combinazione di così asimmetrici e variabilità del processo tramite la valutazione del costo atteso ("*expected cost*"). Una nuova formulazione e un appropriato approccio numerico sono proposti per valutare i costi attesi con variabilità di processo e modello di costo arbitrari. A partire da queste considerazioni, due criteri generalizzati per decidere quando fermare l'ottimizzazione sono proposti, ognuno con particolari vantaggi in specifiche applicazioni. Le prestazioni di queste procedure sono comparate ad un esistente modello allo stato dell'arte, portando una riduzione dei costi pari al 90% quando le misurazioni vengono effettuate solamente durante la fase di ottimizzazione. Infine, una procedura complessiva per l'ottimizzazione di processo, incorporando i metodi proposti, verrà discussa.

Contents

1	Introduction	3
2	Quality control at elevated temperature	9
2.1	Metrology at elevated temperature	10
2.1.1	Traditional contact-based methods	11
2.1.2	Traditional defect-detection methods	11
2.1.3	Optical technologies	11
2.1.4	Lacks and motivation	14
2.2	Forging process optimisation	15
2.2.1	Offline optimisation	15
2.2.2	Online optimisation	15
2.2.3	Lacks and motivation	18
2.3	Work structure and scientific contributions	18
3	Prototype coordinate measuring system description	21
3.1	Overview	21
3.1.1	2D scanner	21
3.1.2	Linear motion system	25
3.2	Measurement process and dataflow	25
3.2.1	Coordinate measuring system setup	26
3.2.2	Sensor-wise data processing	30
3.2.3	Data fusion for constant cross-sectional workpieces	33
3.2.4	Data fusion for non-constant cross-sectional workpieces	48
3.3	Applicability of data fusion concepts	62
3.4	Conclusion	63

CONTENTS

4	System characterisation	65
4.1	Measurand definition	65
4.2	Identification of dominant error sources	66
4.3	Multisensor data fusion	68
4.4	Temperature	71
4.4.1	Refractive index gradient	73
4.4.2	Metrology frame expansion	77
4.4.3	Influence on sensors	78
4.5	Influence on the linear motion system	81
4.6	Noise and sampling analyses	84
4.6.1	Noise evaluation for workpieces at elevated temperature	84
4.6.2	Measurement time vs. sampling density	86
4.6.3	Sensor resolution analysis	88
4.7	Testing at elevated temperature	92
4.8	Conclusion	95
5	Production process optimisation	97
5.1	Optimisation aims	98
5.2	Quality characteristics for process optimisation	98
5.3	Process steps	102
5.3.1	Forging	102
5.3.2	Cooling	104
5.4	Forging process adjustment	106
5.4.1	Assumptions and model selection	107
5.4.2	Process capability	108
5.4.3	A numerical approach to the setup adjustment problem	108
5.4.4	A generalised stopping criterion for setup adjustment	120
5.4.5	Coupled process adjustment	127
5.5	Conclusion	135
6	Conclusions	137
	References	141

List of abbreviations

Table 1: List of abbreviations

Abbreviation	Description
CAD	Computer-Aided Design
CCD	Charge-Coupled Device
CMOS	Complementary Metal-Oxide-Semiconductor
CMS	Coordinate Measuring System
CT	Computed Tomography
CTE	Coefficient of Thermal Expansion
DSC	Dynamic Stopping Criterion
EPC	Engineering Process Control
FEM	Finite Element Method
FPGA	Field Programmable Gate Array
FWHM	Full Width at Half Maximum
IASD	Integrated Absolute Setpoint Deviation
ICP	Iterative Closest Point
IRC	Integrated Real Cost
LSL	Lower Specification Limit
MCS	Machine Coordinate System
PCI	Process Capability Index
RSM	Response Surface Methodology
SA	Setup Adjustment
SPA	Statistical Process Adjustment
SPC	Statistical Process Control
SSC	Static Stopping Criterion
TOF	Time Of Flight
USL	Upper Specification Limit
VIM	International Vocabulary of Metrology

CONTENTS

Chapter 1

Introduction

The ongoing globalisation and rapid advances in information technology ease the access for companies to the global market compared to just about 20 years ago. For customers, this means an enormous variety of potential suppliers. For manufacturers, this results in a more intense competitive situation. To stand out from competing companies, various strategies are pursued to produce goods of higher quality, less expensive and to decrease delivery time and time to market.

Traditionally, quality can be defined as "fitness for use" [1]. In other words, a product that is more suitable for a certain use than others has superior quality. A more modern definition of quality is "Quality is inversely proportional to variability" [1]. Thus, the variability in quality characteristics of a produced good is accounted for. Quality characteristics can be classified into variables data (continuous quantities, e.g. length, hardness, temperature, luminous intensity) and attributes data (discrete quantities, e.g. "good", "bad", "number of emergencies") [1]; or, according to the International Vocabulary of Metrology (VIM), ordinal quantities and nominal properties [2]. Within the variety of quality characteristics, geometrical characteristics are one key factor for a products functionality [3]. This work focuses on geometrical quality characteristics with variables data and the term *quality characteristic* is used to refer to such.

Product miniaturisation and the trend towards higher product quality lead to continuously decreasing geometrical dimensions and tolerances. Consequently, demands on production and quality assessment processes are increasing. Even if the reduction in product size is excluded, geometrical characteristics become increasingly complex. Many products, e.g. car bodies, airplane wings, mobile phones, optical components or turbine blades, employ complex shaped geometries to optimise their application specific performance. For many goods – especially consumer products – not only technical but also aesthetic perfor-

mance is of great importance. To create aesthetically attractive products, designers often incorporate free formed surfaces [4]. Freeforms (also called sculptured surfaces or curved surfaces [4]) are defined by having no invariance degree [5]. Similar to the degree of freedom in kinematics, the invariance degree is the number of principle rotations (rotations around coordinate system axes) and translations for which an ideal feature is kept identical [4]. Another definition describes freeforms as arbitrary complex surfaces without rotational or translational symmetries [6, 7].

In the broad range of modern quality management methodologies (e.g. Six Sigma, ISO 9000 family), process improvement is a key factor for increasing quality [1]. The technical foundations for such can be found in the disciplines of Statistical Process Control (SPC), Engineering Process Control (EPC) and Statistical Process Adjustment (SPA).

Based on the modern definition of quality, the objective is to minimise the variability in the output of a production process. In SPC, this is achieved by identifying and eliminating *assignable causes*, i.e. avoidable effects that cause relatively large variations. If such causes are not present, the process is said to be *in statistical control*, and only *chance causes*, i.e. unavoidable inherent background noise, of variation are present [1]. Processes that operate in statistical control exhibit increased product quality and reduced cost. In contrast, EPC methods adjust process parameters online, such that the process output is as close to the target as possible [8]. SPA is a set of statistical techniques for modelling, forecasting and controlling dynamic processes with focus on adjustments [9], i.e. when and by what quantity process parameters shall be adjusted.

Important output quantities of a production process, e.g. geometrical quality characteristics, are a necessary input to the statistical framework of process control and process adjustment. Such quality characteristics are acquired by means of measurements. Consequently, the measurement trueness and precision [2] are important influence factors for process control and adjustment methodologies.

A simple example of a process control is brewing coffee. A process variable is e.g. the amount of water in the process of brewing coffee. The less water runs through the coffee powder, the stronger the taste of the coffee. The measurement process in this example is tasting the coffee. If it is perceived as too weak or too strong, the amount of water can be adjusted accordingly. For the adjustment of the process, a relationship between the measured values and control variables must be established. By exploitation of this relationship, a feedback into the process is enabled. In the simple example of brewing coffee, this relationship is rather trivial: less water leads to stronger coffee and vice versa. However, for complex manufacturing processes the relationship is not always evident and has to be determined.

For economic reasons, measurements should be performed as early as possible in the production process (e.g. [3, 10, 11]). If a defective part can be identified early, there is no reason for further processing. Further, the economic impact of defective parts rises as the production process progresses, e.g. a final product exhibits higher economical value than its raw materials. From the viewpoint of productive metrology [12], early measurements allow to gain knowledge about specific production process steps and about the feasibility of subsequent steps. Also for process optimisation, it is reasonable to acquire measurement data not only at the end of the entire production process, especially for complex, multi-step production processes. Measurements directly after a production process step, i.e. *process-intermittent measurements* [13], when the process is "momentarily halted", allow for selective optimisation of the individual step. Therefore, process optimisation can be broken down into simplified subtasks. Moreover, effects of a production process step on the geometry after subsequent process steps could be assessed, given that models of the involved steps are available.

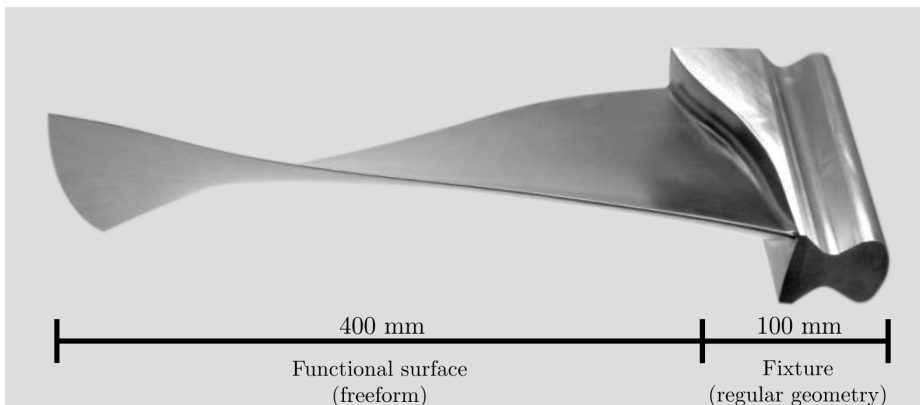


Figure 1.1: A typical turbine blade with functional surface and fixture indicated. Source: Pietro Rosa TBM s.r.l. [14].

As an example in industry, where such an optimisation would be particularly effective, a complex multi-step production process is analysed in this work, namely, manufacturing of gas turbine blades.

Turbine blades are used in a variety of industrial products [4], e.g. cooling fans, turbo charger systems and jet engines. They have both, freeform geometries and regular geometries; tolerances are between 0.1 mm and 0.5 mm profile tolerance on the freeform aerofoil and between 0.02 mm and 0.05 mm on regular geometries, where coupled to the turbine rotor (figure 1.1). The function of the freeform surface is optimisation of flow characteristics in the turbine [3]. The production of gas turbine blades is a multi-step process (figure 1.2).

CHAPTER 1. INTRODUCTION

In a first step, the raw material is preformed to a billet at elevated temperature in order to obtain an optimal spatial distribution of material for forging. The billet then is heated again and forged. Next, the forged workpiece is cooled in calm air when its material passes through microstructural phase transformations. These transformations cause changes in the specific volume and take place at different times during the cooling, depending on the local thickness of the workpiece and heat exchange conditions. Therefore, they cause unwanted changes in the geometry of the workpiece, most evident at the thinner freeform shape [15–18]. The next step is machining, which has two functions: refinement of geometry and surface finishing. The refinement of geometry is necessary because available forging and cooling processes cannot generate the desired final geometry. The last step is quality control, to check for conformity of the produced gas turbine blade.

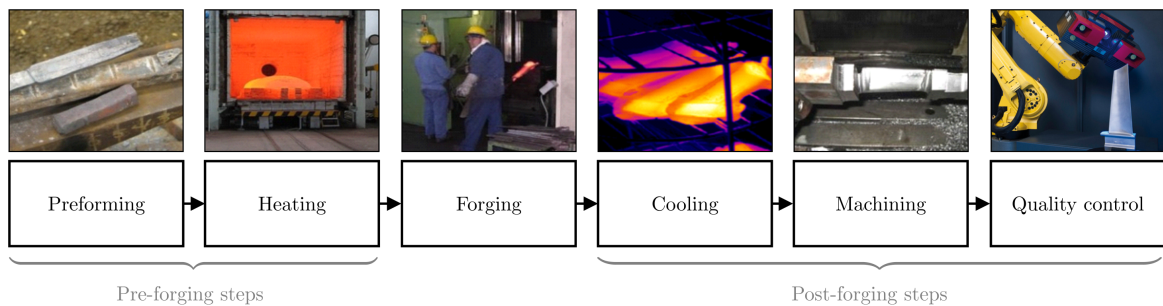


Figure 1.2: Schematic representation of the phases of the process-chain for production of gas turbine blades.

The imperfect forging process results in a significant waste of energy, material, time and money [19]. Machining is particularly costly for the area of the freeform surface [20, 21] and in relation to the usage of difficult-to-cut materials. Optimally, the machining step should only consist of surface finishing with limited removal of material. Efforts were made to reach near net-shape (final shape) products by forging processes [22–24]. However, forging tolerances [22] (i.e. tolerances after the forging process, also forging allowances [15]) are typically in the order of 10^{-3} m, one to two orders of magnitude higher than tolerances specified on the final product.

For measurements on turbine blades, a workpiece coordinate system at the root of the blade (figure 1.1) is used and a series of two-dimensional (2D) cross-sections along the freeform surface (aerofoil region) is extracted. Quality characteristics on sections are e.g. rotation (twist), translation (bow), radii, maximum thickness and chord length [4]. Note that only a subset of the typical measurands are feasible to be evaluated by process-intermittent measurements, e.g. radii of edges are not well defined after the forging process since they are connected to flash, i.e. excess material created by the forging process (figure 1.3).

Measurements on turbine blades can be performed only several hours after forging, when the workpiece has cooled down, as conventional measurements are performed at 20 °C [25]. Thus, optimisation of the process based on measured quality characteristics is feasible only with considerable dead time. In addition, measurements after cooling of the workpiece reflect joint geometrical errors, induced by forging and cooling, thus yielding no information about the distinct production steps contributions.

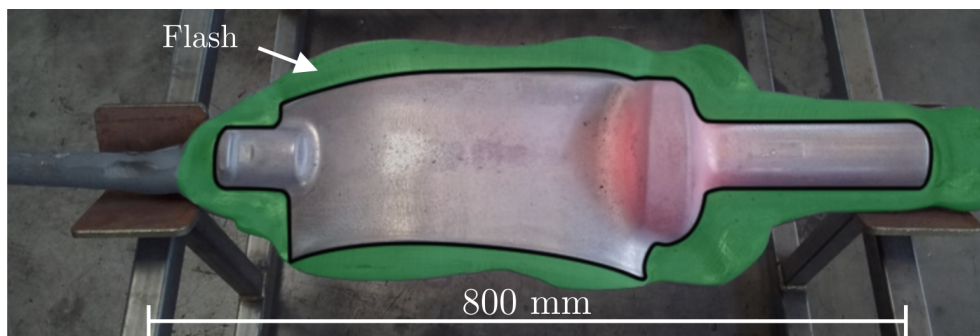


Figure 1.3: Gas turbine blade made of stainless steel X20Cr13 at elevated temperature after forging. The flash is highlighted in green and the contour of the blade is accentuated in black.

To enable a separate assessment of individual production steps, it can be necessary to measure a workpiece before and after a production process step. However, for forging, the actual forging process step can be considered as the first step that defines workpiece geometry, regardless of the billet geometry. Thus, a measurement before forging is not required.

Process-intermittent measurements would allow for online feedback into the production process, which is especially crucial during ramp-up of small batch processes. For this feedback, a relationship between measured quality characteristics and the forging process parameters is to be made. If nominal values for quality characteristics directly after a production process step would be available, the step could be selectively optimised, without considering the entire process. This can be the case for forging processes where a near-net shape production is aimed for – with the net shape known. However, for turbine blade production, the cooling process has significant influence on the aerofoil geometry and must be taken into account [15–18].

Due to inherent uncertainties in the measurement data and process variation, process parameters are determined with some degree of uncertainty and the effectiveness of optimisation is thereby limited [26]. By incorporating such variations, a task specific limit for process optimisation could be determined.

CHAPTER 1. INTRODUCTION

Returning to the example of brewing coffee: the measurement uncertainty is the uncertainty of the human sense of taste. This could be e.g. ± 1 cl ($k = 3$) water per cup. If the machines process parameter is set to 5 cl water, and does not deviate from this setting, a value between 4 cl and 6 cl is measured, i.e. tasted. If the optimal amount of water is known to be e.g. 5.5 cl, based on the uncertainty in the measured values, is not trivial to state whether more or less water is to be used.

Optimisation of industrial production processes suffer from the same limitation: due to measurement uncertainty and process variations, adjustments to the process are determined by uncertain information. Incorporating those could accelerate and simplify the process adjustment in terms of a task specific stopping criterion, what leads to economic advantages.

For process-intermittent measurements after forging, a system that is capable of measuring at elevated temperature is required. Thus, in the next chapter, a review of the state-of-the-art in metrology at elevated temperature is given. Moreover, the state-of-the-art in statistical process adjustment, a domain concerned with adjusting processes, e.g. during ramp-up, is reviewed. Clearly, the former is a requirement for the latter and both are necessary to optimise the production process of turbine blades economically.

Chapter 2

Quality control at elevated temperature

In the context of geometrical quality characteristics, technical designers are provided with a wide set of dimensioning and tolerancing possibilities [27]. Tolerancing of freeforms can be done by defining profile tolerances for surfaces [4, 27], possibly with reference to a datum.

There exist two fundamentally different approaches to assess such tolerances: direct and indirect comparison [4]. The direct approach employs gauging with dedicated measurement equipment, what does not yield a quantitative deviation but rather a yes/no assertion about conformance. This comparison is clearly not very flexible and can be time consuming. Note however, that profile tolerances are thereby assessed in an integral sense, in contrast to indirect comparison. This work concentrates on the indirect comparison approach that replaces the hardware gauge(s) by a digital model of the nominal geometry, e.g. a Computer-Aided Design (CAD) model. This model is compared against measurement results by means of a computer program. Measurement results can be obtained by any kind of appropriate measuring system. To retain the flexibility of this approach, typically very flexible measuring systems, i.e. Coordinate Measuring Systems (CMS), are employed. CMS digitise the physical geometry by pointwise sampling. The sampled point coordinates are then combined appropriately to calculate geometrical features of interest [3, 10]. Clearly, only a finite number of points can be acquired, whereas the geometry specification refers to a complete profile or surface. This well-known fact is called *method divergence* [28–31] and is taken into account by appropriate statistical methods and uncertainty statements.

Depending on the workpiece, its manufacturing process and tolerance limits, it can be inevitable to sample freeforms densely, in order to allow for sufficiently low uncertainty statements. Moreover, tolerances of freeform surfaces are defined by means of profile tolerances (for surfaces) and a single measurement point outside the tolerance causes non-

conformity of the workpiece. Consequently, for sufficiently high probability to capture crucial regions, adequate dense surface sampling is necessary. Based on these considerations, it can be stated that quality assurance for freeforms requires flexible and highly efficient CMS to maintain an economically feasible measurement process.

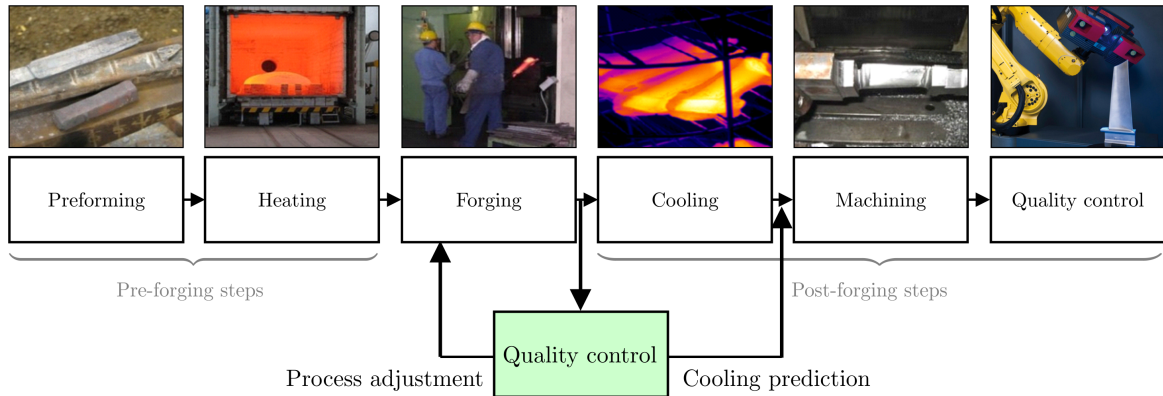


Figure 2.1: Schematic representation of the phases of the process-chain for production of gas turbine blades, including process-intermittent measurements (quality control).

Process-intermittent measurements at elevated temperature have several advantages as compared to post-process measurements. If the final geometry can be predicted, conformance statements can be made before the workpiece is actually finalised. Additionally, if other process steps follow, a statement about their feasibility can be given (figure 2.1, cooling prediction). In addition, specific process steps can be optimised (figure 2.1, process adjustment), given that the desired output of the step is known or models of subsequent steps are available. If measurements are made after separate production steps e.g. after forging but before cooling, errors originating from the different production steps can be separated. Thus enabling a distinct assessment of production steps regarding their respective influence.

Although, process-intermittent measurements in hot working processes are exposed to the extreme environment of a production plant [19, 32], e.g. high temperature gradients, heat radiation, vibrations, and are not widely used.

2.1 Metrology at elevated temperature

Measurements of forged freeform workpieces are nowadays only feasible after cooling, what introduces hours of dead time for feedback into the production process. Measuring workpieces at elevated temperature is complex and subject of current research. There exist both, commercial systems [33–41] as well as scientific publications [19, 32, 42–51]

for measuring profiles, rods and other regular geometries at elevated temperature. In the following sections, the state-of-the-art metrology at elevated temperature is presented.

2.1.1 Traditional contact-based methods

Traditional methods are e.g. manual measuring using callipers, what requires operators to be near to the workpiece where they are exposed to immense heat [19, 49, 52]. An alternative approach is a comparison of a measuring rod with chalk marks that is held in front of the forging and compared to its dimensions [32, 49]. This approach has obviously only limited accuracy due to operator influence, e.g. due to subjective perception and the parallax effect between the measuring rod and workpiece. It shall be emphasised that traditional contact based methods are dangerous, considering the immediate proximity of the operator, and may cause serious injuries [19, 49, 52]. Additionally, they may inflict damage to the measuring device.

2.1.2 Traditional defect-detection methods

Before optical technologies emerged, defect detection on workpieces at elevated temperature, mostly hot rolled bars, was conducted by inline systems based on Eddy-Current Testing (ECT) technology [53]. Examples are products from Institut Dr. Förster GmbH & Co. KG [33] or Prüftechnik Dieter Busch AG [34]. Such systems detect defects on ferromagnetic workpieces indirectly and they are not to be classified as coordinate measuring systems; no geometrical quantities are obtained but electrical quantities. From variations in the measurement results, surface defects are inferred.

2.1.3 Optical technologies

Most recently, optical technologies are utilised for dimensional measurements at elevated temperature. Therein, three different technologies are mainly reported: time of flight (TOF), optical triangulation and image processing. An overview of scientific reports and commercial products is given in the following. For a general overview of optical methods in dimensional metrology see [54].

To classify the type of measurement result, 1D, 2D, 2.5D and 3D are defined here as follows: the number of dimensions of a measurement result, which values are non-restricted. Thus, a distance measurement is defined as 1D, since its scalar value can vary arbitrary. A 2D measurement can be represented by Cartesian coordinates (x, y) for which both, x and

y can have any value. 2.5D is a special case and is defined in this work as in [55]: the z -coordinate depends on the (x, y) position, i.e. $z = f(x, y)$. Consequently, the z value is not arbitrary, since only a single z value for a given (x, y) exists. 3D type measurement results remove this constraint and are typically represented as a 3D pointset. Note that fused datasets from multiple 2.5D measurements are also classified as 3D in this work, though such 3D coordinates may not be completely arbitrary.

Please note that the terminology from reviewed reports is adopted in this section and may not be consistent nor correct. If stated in the reports, an uncertainty value of measurement results is given here; otherwise, no statement is made.

Time of flight

Fu et al. [44] use two laser scanners to measure outer diameters of hot cylindrical shells with a standard diameter of 5.75 m and combine them with infrared temperature measurements to calculate inner their diameters. Workpieces are reported to have a temperature of approx. 870 °C. They also show a 3D model, generated from the sparse point-cloud of the measured convex parts. By combination of two laser scanners, 3D measurement data is generated. A deviation of the outer diameter to the standard size of less than 15 mm is stated.

Bokhabrine et al. [47, 48] utilise two commercial Leica ScanStation2 TOF sensors to measure the outer diameter (nominally up to 6 m) of hot cylindrical shells at 700 °C to 1000 °C. By carrying out three measurements, they reconstruct the 3D surface of the regular shell geometry.

He et al. [45] adopt a similar approach by using two TOF sensors and rotary tables to measure the outer diameter of hot cylindrical shells with diameters of approx. 5.7 m at 850 °C to 1250 °C. By the chosen sensor setup, 2.5D measurement data is created. They simulate the shrinkage of the workpiece after measurement what yields an estimate of the diameter at ambient temperature. A maximum error of 0.235 % of the estimated diameter compared to an accurate CMS measurement of the workpiece is reported.

Du et al. [32] measure hot forgings, using a commercial TOF sensor (Sick LMS100). Due to the use of a single sensor, the system is limited to depth measurements, i.e 2.5D. Tian et al. [19] use a TOF sensor to measure large workpieces, e.g. crankshafts over 20 m of length.

Määttä et al. [51] discuss the use of TOF systems for thickness measurements of endless products in steel production plants at 1100 °C to 1400 °C. They primarily focus on the TOF sensor construction and its electronics. A total accuracy of the system of ± 10 mm is stated. The measurement time for a single point 1D measurement is 0.5 s.

2.1. METROLOGY AT ELEVATED TEMPERATURE

The LaCam Forge product from Ferrotron/Minteq [37] is a TOF based system that measures distances by deflecting a laser beam in two axes, thus yielding 2.5D measurement results. Additionally to geometrical measurement, the heat distribution is measured by the system.

The 3D Portal from MERMEC S.p.A. [38] is designed to measure open-die forgings up to 1250 °C by means of the TOF principle. By combination of multiple sensors, 3D measurement data is obtained. Their software can evaluate diameter, thickness, length, straightness and eccentricity. The measurement range is 1 m to 120 m.

Optical triangulation

Bernstein [42] analysed an optical multisensor CMS consisting of a triangulation and shadow system. By the use of multiple sensors, measurement results are 3D. A standard uncertainty [2] of 12 μm is reported for length measurements. Measurements were performed on profiles in a range up to 80 mm under shop floor conditions at profile temperatures up to 840 °C. The systems temperature is controlled by a water-cooling system. For laboratory conditions, with artificially generated disturbances (vibration, sensor orientation, external light, contamination of optical sensors), depending on the measurement range and evaluation method, standard uncertainties in the range from 12 μm to 122 μm are reported.

Zhang et al. [56] show a triangulation based system for measuring hot forgings. A measurement of a cylinder under controlled environment yields a maximum deviation of 3 mm from a reference value. The single triangulation sensor is moved on two orthogonal axes to combine measurements to a 3D model.

Liu et al. [46] present an active stereo-vision system composed of two cameras and of a digital light projector (DLP). They reduce the effect of emitted radiation of hot steel workpieces by using an optical filter and extract 1D distance measurements in the range of 800 mm from the recorded data.

Stöbener et al. [50] investigate the usability of laser triangulation for workpieces at approx. 900 °C. By using a point laser, 1D distance measurements are obtained. They state an accuracy, i.e. range of repeated measurements, of $\pm 20 \mu\text{m}$. The application of an optical bandpass filter is proposed, to filter infrared light radiation emanating from the hot workpiece.

LIMAB [39] offers triangulation sensors and triangulation systems for 2D measurements of profiles at elevated temperature. A measurement system accuracy down to 0.03 mm ($k = 2$) is stated, depending on the bar size. No statement is made about how this performance specification was evaluated.

The Danieli HiPROFILE [36] is a triangulation-based system, made for measuring profiles of steel bars at approx. 1000 °C. The system can evaluate measurands on several profile classes.

NEXTSENSE GmbH [40] offers commercial systems to measure profiles at elevated temperature by use of multiple laser triangulation sensors. By their software, operators can specify application specific measurands on the profile. They state "highest accuracy" and "unprecedented accuracy".

Zumbach Electronic AG [41] offers systems for complex 2D measurements of convex section profiles with different optical technologies, e.g. triangulation and shadow systems. For their Steelmaster systems, they state a measurement repeatability of 10 µm up to temperatures of 1200 °C.

Image processing

Dworkin & Nye [49] use the combination of a Charge-Coupled Device (CCD) sensor with an optical infrared bandpass filter to measure 2D geometries of hot workpieces at 900 °C to 1300 °C. By image thresholding, the workpieces silhouette is extracted on which measurements are performed on. It is interesting to note that they make actual use of the infrared radiation of the workpiece to determine its silhouette, whereas others try to reduce its influence [46, 50].

The HotEye system from OG Technologies, Inc. [35] is an image based defect detection system that is designed for hot rolled bars and rods at up to 1450 °C. The systems purpose is detection of defects like seams, overfills, laps, slivers, tears and roll cracks.

2.1.4 Lacks and motivation

The literature review indicates that there was no measuring system reported, capable of measuring freeform shaped workpieces at elevated temperature. Most of the above-mentioned systems measure profiles or cylindrical shells. Measurements of spherical shell covers [43] are closest to freeform surfaces, though only diameters were measured on different heights at the cover.

Moreover, for most of the systems mentioned above, no quantitative statements about errors, e.g. in terms of Maximum Permissible Error (MPE) of length measurement [57], are declared. If an error statement is made, applied procedures, normatives and/or measurands are not thoroughly stated.

2.2 Forging process optimisation

In this section, the state-of-the-art in process optimisation for hot working, specifically for forging, is discussed. The topic is split into: offline optimisation, based on assumptions and models of the process and applied before the actual production starts; and online optimisation, based on the measured output of a process and applied while the production process runs. This subdivision highlights that much scientific effort was made in offline optimisation, but online optimisation was practically not addressed for hot working processes.

2.2.1 Offline optimisation

To characterise the forging process, typically, Finite Element Method (FEM) simulations are utilised (e.g. [23, 24, 58–61]). For optimisation, parameters settings that produce the best FEM model, in terms of material properties or geometry, are found by appropriate methods [60]. With the offline approach, even parameters that remain fixed during production can be considered variable, e.g. the geometry of dies is sometimes treated as such [22–24]. The calibration of FEM simulations by data from real experiments, which is a necessity for feasible FEM simulations [58], is rarely addressed in the literature.

Although offline methods have demonstrated their ability to improve forging processes, online process optimisation methods have the advantage to react on variations of e.g. environmental disturbances during production. Such variations are not directly measurable but can influence quality characteristics and their effect should therefore be taken into account.

2.2.2 Online optimisation

According to a recent review of closed-loop control in metal forming [62], there has been little research efforts into online optimisation for forging processes. The research from Recker et al. [63] describes models to predict the microstructure properties of incrementally forged blocks, although no experiments were yet carried out.

In this work, the focus is on discrete manufacturing processes, e.g. the production of gas turbine blades by forging. Since batches are typically small, e.g. 50 products, the ramp-up of the production process is crucial. Due to customer specific products, optimal production parameters may differ from batch to batch and must thus be reset. Consequently, the focus is on parameter adjustment during the ramp-up phase. This consideration leads into the domain of Statistical Process Adjustment (SPA), a set of statistical techniques for mod-

elling and hence, forecasting and controlling dynamic processes [9]. State-of-the-art SPA procedures, for possible use in forging process adjustment, are reviewed in the following.

The production of discrete goods can be considered as a *setup dominant* [64] process, i.e. quality characteristics of interest have a high stability during the production of a batch. The mean of quality characteristics is only influenced by the setup process, and is not subject to drift during production. Due to typically small batch sizes and short production runs of several hours in the considered application, this assumption is made in this work.

On that condition, an imperfect setup operation, i.e. initial setting of process parameters, will lead to a systematic error during production, evident by a persistent offset of the quality characteristic. The initial adjustment of a process is therefore considered as crucial for discrete-part manufacturing [9]. To adjust the quality characteristic mean during the setup phase, proposed methods in the literature can be split into two classes [65]:

- Methods that assume a priori knowledge about parameter influence on quality characteristics on a specific product is available, e.g. due to historical data. Based on that information, a process model is developed and possibly refined online [66, 67].
- Procedures that adjust a process without (or with incomplete) knowledge about the process parameters and their influence on quality characteristics on a specific product, but assume a general process model. Under these conditions, the problem of process adjustment is known as *setup adjustment problem* (e.g. [9, 26, 65, 68]).

Approaches from the first class rely on historical data for the initial creation of the process model, which led to an adjusted process in a prior (similar) batch. Clearly, such modelling does not account for unpredictable changes in the production process, e.g. different environmental influences. Updating the model online during production, by information from the current batch, then does account for such variations. However, in discrete manufacturing, this can be infeasible due to the amount of process information necessary to estimate a sufficiently accurate model. With the model from Nembhard & Birge [67], as an example, the variation of quality characteristics has to be estimated at each optimisation step. This is impractical for discrete manufacturing processes where only one piece at a time is produced. In addition, process parameters are modelled as known parameters, without any uncertainties [66, 67]. Moreover, uncontrollable and possibly unknowable parameters, e.g. material properties, environmental influences, are sometimes treated as known [69].

Concerning the second class, pioneering work by Grubbs [68] yielded a simple adjustment rule. His rule is based on observations of the quality characteristic for a specific combination of *off-target cost function*, i.e. costs caused by deviations from a nominal value,

2.2. FORGING PROCESS OPTIMISATION

and process variation model, i.e. characteristic variation due to the production process and measurement uncertainty. Some authors (e.g. [65, 70–73]) utilise models to dynamically estimate process parameters, e.g. by sequentially applying Bayes' theorem. Thereby, knowledge about process parameters is updated each time when measuring quality characteristics and become more and more precise during production.

Unfortunately, the process is mostly modelled as an identity relation, i.e. a change of x units in the process parameters yields a change of x units in the quality characteristic. However, recent publications introduce more elaborate process models, e.g. a linear relationship between parameter adjustment and quality characteristic [70, 74].

An interesting development for setup adjustment are asymmetric off-target cost functions [43, 65, 73]. For such, the optimal process setpoint shifts towards the lower cost side; e.g. if the cost for violating a Lower Specification Limit (LSL) are less than the cost for violation of the Upper Specification Limit (USL), it may not be the optimal choice to set the quality characteristic mean in the centre between the limits. This was proven by Ladany for constant asymmetric off-target cost functions and a normally distributed quality characteristic [75]. Therefore, the optimal *process setpoint*, i.e. a value by which the quality characteristic is to be shifted, must be determined. For this, closed-form solutions for different off-target cost functions and quality characteristics can be found in literature [43, 65, 73, 76–78]. Although for some combinations, e.g. a quadratic asymmetric off-target cost function and normal quality characteristic distribution, no closed form solution for the optimal process setpoint exists and numerical treatment is required [43, 65, 73].

For process-intermittent measurements with focus on forging tolerances, asymmetric off-target cost functions are necessary. Descriptively, suppose the thickness of the blades' aerofoil at a specific position is a quality characteristic. If thickness is too high, the machining step is more expensive since more material is to be removed. However, if thickness is below its nominal value, the workpiece must be classified as defective.

Independently of the above classification, an implicit question, accompanying the adjustment during ramp-up, is: when to stop this initial procedure? The question when to adjust, and when not doing so is actually more advantageous, is addressed by deadband adjustment models, e.g. [72, 79–81]. In such models, the cost for process adjustment are non-zero, what results in a temporally varying deadband rule. If the quality characteristic mean is out of the bands limits, the process is to be adjusted. If it is inside the bands limits, an adjustment is not feasible, since the cost for adjustment are higher than the average cost due to the non-optimal process setpoint. Although such models optimise cost by leaving out adjustments, they do not limit the number of adjustments and hence do not provide a stopping criterion.

Trietsch [82, 83] proposed a rule of thumb of five or ten adjustments. This somewhat arbitrary choice is justified by three arguments: many workers are trained to take five samples, as they do with control charts; multiples of five are easy to calculate, also without calculator; and a sample size of five allows checking for excessive variability by classical statistical methods. He also determined the number of adjustments to make, i.e. he provided a stopping criterion, for quadratic off-target cost and a normal quality characteristic distribution [26], based on results from Grubbs [68].

2.2.3 Lacks and motivation

To adjust production processes during their ramp-up, many approaches exist. However, no application on hot worked, freeform workpieces was reported. Moreover, determination of the optimal process setpoint for asymmetric off-target cost functions is only reported for a subset of cost functions and process variation models.

Concerning the setup adjustment problem, only few authors addressed a non-identity relation between process parameter adjustment and quality characteristic. Since the forging process may exhibit a complex relationship, this is possibly to be accounted for in the adjustment procedure.

Several models to minimise cost by leaving out adjustments were reported. However, such methods do not state a definite number of workpieces, after which to stop adjusting. The inherent purpose of process adjustment, i.e. setting up a process, implies that it shall be performed during setup of the process and not for the duration of a whole batch (or possibly multiple batches). The solution by Trietsch is limited to a specific off-target cost function and process variation model. Consequently, if asymmetric off-target cost functions are to be used, an adequate stopping criterion is missing.

2.3 Work structure and scientific contributions

In the context of the Eurostars HOTGAUGE (E!6692) research project, a prototypical CMS for measurements of freeform workpieces at elevated temperature was developed. The CMS was partly built by Zumbach Electronic AG [41] in cooperation with the University of Padua. It was tested under shop floor conditions at a gas turbine manufacturer's site, namely, Pietro Rosa TBM s.r.l. [14]. Metrological data processing and testing of the system was conducted by members of the University of Padua and the University of Applied Sciences NTB. The participation in this project provided the author an opportunity to address

2.3. WORK STRUCTURE AND SCIENTIFIC CONTRIBUTIONS

above-mentioned lacks and conduct real experiments to verify the methods proposed in this work.

In the beginning of chapter 3, a brief overview of the prototypical CMS is given. The remainder of the chapter discusses the measurement data processing and multisensor data fusion concepts of the system. The author's main contributions are:

- A fast heuristic surface reconstruction procedure that approximates the workpiece surface based on a set of measurement points.
- A 2D data fusion method based on the envelope method that also allows for detection of high measurement point dispersion.
- A method for automatic determination of sensors positions and orientations in multisensor laser triangulation coordinate measuring systems that allows for improved sensor adjustment and 3D data fusion.

Major influences on single point distance measurements at elevated temperature are identified and discussed in chapter 4. Moreover, a testing procedure to evaluate the performance, in terms of MPE of length measurements, of the CMS at elevated temperature is presented. The author's main contribution is:

- Assessment of selected influences on measurements at elevated temperature, based on experimental data.

In chapter 5, process adjustment, based on measurements at elevated temperature, is discussed. Therein, appropriate quality characteristics, off-target cost functions, the determination of the optimal process setpoint and a generalised stopping criterion are discussed. Based on those results, a coupled adjustment approach is proposed. Contributions of the author are:

- A numerical method to determine the optimal process setpoint. The approach enables the use of arbitrary cost functions and quality characteristic distributions.
- Two stopping criteria for arbitrary cost functions and quality characteristic distributions, with distinct advantages for specific application cases.
- Proposal of a coupled adjustment approach, comprising process characterisation and adjustment of the forging process, including sensitivity analyses and an example of turbine blade forging.

Finally, in chapter 6, conclusions are drawn.

CHAPTER 2. QUALITY CONTROL AT ELEVATED TEMPERATURE

Chapter 3

Prototype coordinate measuring system description

3.1 Overview

The CMS, developed in the context of the Eurostars HOTGAUGE (E!6692) project [18, 84, 85], is composed of two main subsystems: a 2D scanner by Zumbach Electronics AG [41] and a custom linear motion system (figure 3.1). The scanner nominally acquires 2D cross-sections of a workpiece in the XY-plane by means of multiple light sectioning sensors, i.e. active triangulation sensors, projecting a laser line [86]. The linear moving system drives a workpiece through the 2D scanner (Z-axis). The Machine Coordinate System (MCS, 3.1) is obtained by combining the 2D scanner coordinate system (2D) with the linear motion system axis (1D). From multiple cross-sections with their corresponding z-positions, a 3D pointset, and eventually a surface representation is generated. In the following sections, the 2D scanner and the linear motion system are described. A summary of the main technical data of the CMS is given in table 3.1.

The aimed MPE of length measurements was declared a priori to be 0.2 mm. Recall that the systems purpose are process-intermittent measurements, directly after the forging step (chapter 1). At that stage, forging tolerances to be verified are in the order 10^{-3} m.

3.1.1 2D scanner

The 2D scanner has a modular design to mount up to eight light sectioning sensors. Each sensor, consisting of a line laser, a Complementary Metal-Oxide-Semiconductor (CMOS)

CHAPTER 3. PROTOTYPE COORDINATE MEASURING SYSTEM DESCRIPTION

Table 3.1: Summary of main technical data of the prototype CMS. Camera and laser emitter product specifications are omitted due to a non-disclosure agreement.

Characteristic	Value
Dimensions ($H \times W \times D$)	2.6 m \times 2.5 m \times 1 m
Measurement speed	320 Hz, 1 000 000 points/s (typical)
Measurement time	< 10 s (for 800 mm long parts)
Measurement volume	860 mm \times disc with \varnothing 800 mm (cylindrical)
Sensor camera type	CMOS sensor, 2048 \times 1088, global shutter, GigE interface, 5.5 μ m \times 5.5 μ m pixel size
Sensor depth resolution	0.03 mm (typical)
Sensor sampling distance	0.3 mm (typical)
Laser emitter	laser diode with cylindrical lens
Laser wavelengths	405 nm, 450 nm, 640 nm and 670 nm
Optical bandpass filters	FWHM = 20 nm, centred at the respective laser wavelength
Internal air temperature	20 \pm 1 $^{\circ}$ C
Pyrometer type	Optris CTlaser 3M [87]
Pyrometer accuracy	\pm (0.3 % of reading + 2 $^{\circ}$ C)
Declared MPE of length measurement	0.2 mm

camera and optical bandpass filter, is arranged on an octagonal frame, termed *metrology frame* (figure 3.1, top right and figure 3.2). Eight sensors are used to obtain complete surface information, even for partly concave cross-sections. Using the maximum number of sensors, the measurement area of the 2D scanner is defined by the manufacturer to be a disc of 800 mm diameter.

To keep sensors free from dust in the harsh shop floor environment, an integrated blowing system is providing a constant flow of clean air in front of each of the sensor windows. Pt100, class B temperature sensors are installed on the top of the octagonal frame, on the housing and inside the housing to monitor the temperature of the respective components. Special attention was given to the thermal insulation of the metrology frame from the heat radiation caused by workpieces at elevated temperature. In particular, the metal plates protecting the system from radiation are water-cooled by cooling coils. Moreover, the temperature inside the housing is stabilised. The inside air temperature of the housing is kept

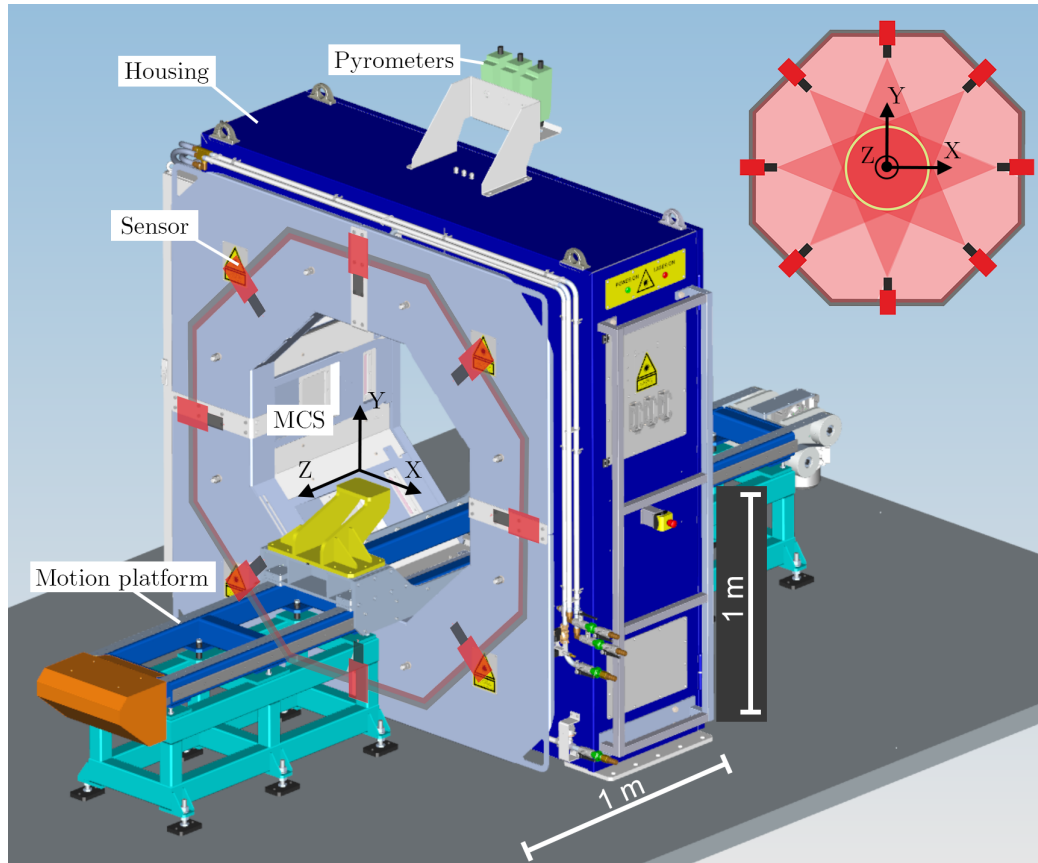


Figure 3.1: CAD model of the CMS with machine coordinate system and sensor arrangement as overlay. Top right: sketch of the metrology frame with measurement area of the 2D scanner inside the yellow circle.

within 20 ± 1 °C. This is achieved by two conditioning systems: an air chiller and an auxiliary water flow inside the metrology frame. The latter is enabled only if the chiller is not sufficient to maintain the temperature within the specified range. Additionally, shield plates are mounted on the front side of the measurement system in order to protect the system from accidental impacts during handling of workpieces. The workpiece temperature is measured at each z-position by multiple pyrometers mounted on top of the system (figure 3.1).

Each sensors laser plane is generated by a point laser emitter (laser diode) using optics that contain a cylindrical lens. Laser emitters have four different wavelengths (405 nm, 450 nm, 640 nm and 670 nm) where opposite lasers are sharing the same wavelength (figure 3.2). An optical bandpass filter is installed in front of each camera to minimise the interference with other lasers, ambient light and the infrared radiation originating from the

CHAPTER 3. PROTOTYPE COORDINATE MEASURING SYSTEM DESCRIPTION

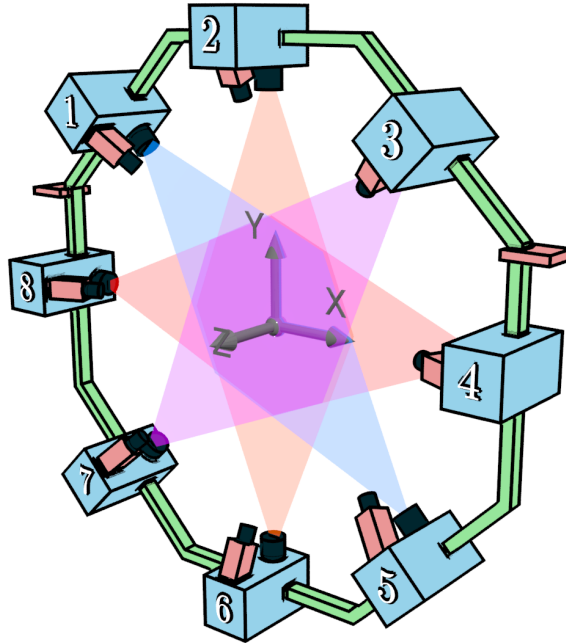


Figure 3.2: 3D sketch of the metrology frame. Laser wavelengths are in the respective colours and sensors are schematically shown with their numbering. Two red cuboids on the frame corners indicate the mounting position of the frame.

workpiece at elevated temperature (section 4.6.1). This setup was chosen to separate data between sensors, i.e. each camera acquires only light from its laser emitter. Opposite laser light is assumed invisible to a sensor due to the presence of an opaque workpiece between them.

The laser plane generates a line (mathematically speaking a curve, although here the term *laser line* is used) on the surface of a workpiece. The CMOS cameras record this laser line and extract its positions on the image sensor by means of a Field Programmable Gate Array (FPGA) and appropriate algorithms. The baseline, i.e. the distance between camera and laser emitter, has a nominal length of 300 mm and the angle α between optical axis of camera and laser emitter is nominally 30 deg (figure 3.2). Laser line positions in pixel coordinates are then transformed into coordinates of the laser plane to obtain a set of distance measurements (section 3.2.2). The datasets from all sensors are appropriately combined to achieve holistic measurements (section 3.2.3 and section 3.2.4).

In addition to light sectioning sensors, up to three pyrometers can be installed on top of the 2D scanner (figure 3.1). They measure the workpiece surface temperature at the cross-section with an accuracy of $\pm(0.3\% \text{ of reading} + 2\text{ }^\circ\text{C})$, as stated by the manufacturer.

3.1.2 Linear motion system

The linear motion system (figure 3.1) is providing z-position information by a magnetic encoder system with a resolution of $2\text{ }\mu\text{m}$. A crucial advantage of a magnetic encoder system, in contrast to an optical encoder system, is its resistance to harsh industrial environment conditions (e.g. dusty air). The magnetic scale is protected from heat radiation in order to reduce elongation due to temperature gradients. To avoid occlusion by the linear motion system, it was designed such that its two rails are located outside the measurement area of the laser scanner.

The maximal travel distance is 860 mm what is also the measurement range of the CMS along the Z-axis. Combining the circular measurement area of the laser scanner with this measurement range yields a cylindrical measurement volume as specified in table 3.1. The terms *measurement area*, *measurement range* and *measurement volume* are used in the following to refer to the 2D scanner, linear motion system and CMS measurement field, respectively.

3.2 Measurement process and dataflow

In this section, the measurement process with its result, a holistic 3D surface representation of the workpiece, is discussed. The focus is on the sophisticated dataflow, digital processing of measurement data (figure 3.3) and data fusion concepts.

First, the necessary setup of the CMS is described, then common procedures for all involved sensors are outlined (figure 3.3). Finally, two adequate data fusion approaches for the case of constant cross-sectional and non-constant cross-sectional, e.g. freeform shaped, products are discussed in-depth. Two distinct approaches are proposed since data fusion requirements for constant cross-sectional workpieces and non-constant cross-sectional workpieces differ significantly in terms of realtime capability and effects from deviations of laser planes coplanarity.

CHAPTER 3. PROTOTYPE COORDINATE MEASURING SYSTEM DESCRIPTION

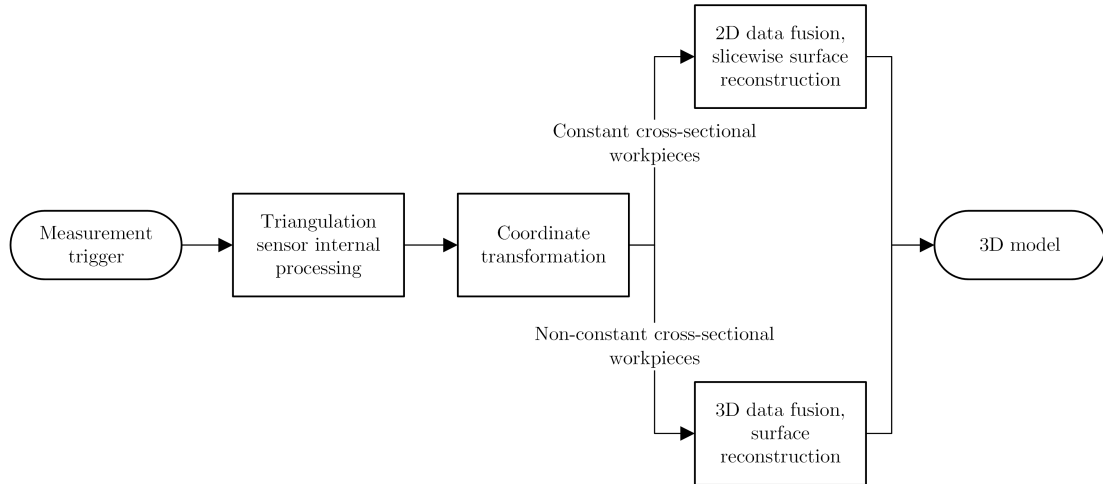


Figure 3.3: Dataflow of measurement data processing in the prototype CMS with two distinct paths for constant cross-sectional (top) and non-constant cross-sectional (bottom) workpieces.

3.2.1 Coordinate measuring system setup

In advance to any measurements, several procedures are to be performed to bring the CMS into expected operating condition. Besides elementary procedures, as adjusting the camera focus and laser focus, more sophisticated procedures are necessary, namely, the adjustment and calibration of sensors, which are discussed in this section.

Sensor adjustment

To obtain measurements of complete cross-sections in a single shot, the measurement areas of all sensors must be aligned to one cross-section of the workpiece, i.e. the laser planes of all sensors must be coplanar (all laser planes are in the same plane). Adjusting sensors by mechanical means, using classical tools, e.g. a goniometer, is state of the art for measurements on constant cross-sectional workpieces with multiple sensors [42]. To approach coplanarity, a sophisticated procedure from Zumbach Electronics AG [41] is used. The procedure guides the mechanical adjustment and is based on a sufficiently known, constant cross-sectional workpieces, a dedicated lighting setup and image processing algorithms.

In reality, perfect coplanarity between laser planes cannot be reached. Consequently, the resulting datasets do not originate from a single cross-section. Depending on the workpiece geometry, this results in differently severe effects. These are discussed in section 3.2.4, together with a novel method for improved sensor adjustment.

Sensor calibration

To obtain distance information from image data, a mapping between the image coordinate system (in pixels) and a real world coordinate system must be available [88]. Establishing this mapping is known as geometrical camera calibration (e.g. [88–90]). To understand geometrical camera calibration, it is helpful to start with its inverse, the geometrical image formation process. Thereby, imaging of a 3D scene on a discrete 2D imaging sensor is modelled. This process is often separated into multiple steps [90]: rigid transformation, perspective transformation, lens distortion and sampling. In the first two steps, an ideal pinhole camera model is assumed, the third step then explicitly accounts for distortion effects originating from the non-perfect lens system.

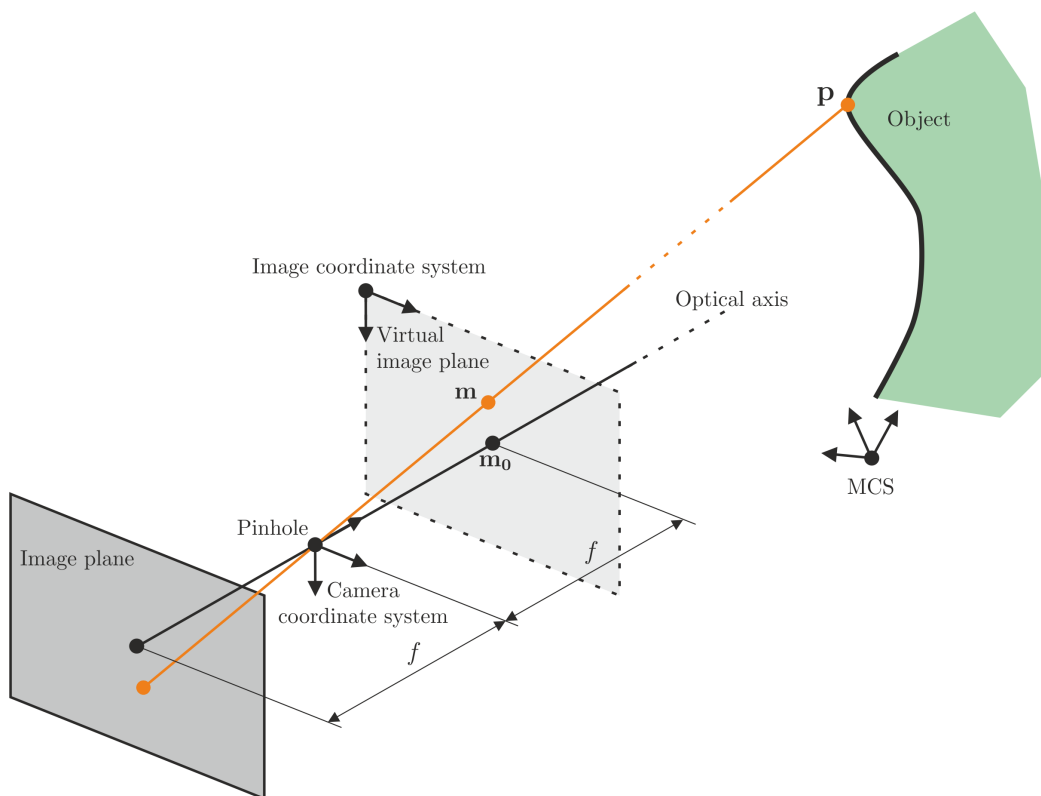


Figure 3.4: Sketch of projective mapping of an object point p to point m in image space. For simplicity, the virtual image plane is used for projection.

The first step represents the coordinate transformation from the world coordinate system to the camera coordinate system. The term "world coordinate system" is commonly used

CHAPTER 3. PROTOTYPE COORDINATE MEASURING SYSTEM DESCRIPTION

in the computer vision [89] and computer graphics [91] domain. It describes a global coordinate system where possible other local coordinate systems are embedded in. However, in metrology, coordinate frames of subsystems are typically related to a MCS that is the global machine-wide coordinate frame [3]. Therefore, the term MCS is used in this work.

The 3D camera coordinate system is centred at the thought pinhole of the camera and oriented along the cameras optical axis and the chip axes (figure 3.4). The transformation can be described as a rigid 3D transformation with six parameters, named *external camera parameters* (e.g. [89, 92]). In principle, a point $\mathbf{p} = [p_x, p_y, p_z]^\top$, where \mathbf{x}^\top designates the transpose of \mathbf{x} , in the MCS is firstly negatively translated by the camera position vector \mathbf{t} and then negatively rotated by the camera rotation matrix \mathbf{R} . Using homogeneous coordinates, i.e. $\mathbf{p}^h = [p_x^h, p_y^h, p_z^h, 1]^\top = [p_x, p_y, p_z, 1]^\top$, this can be written as a single matrix multiplication [89, 92]

$$\mathbf{c} = \begin{bmatrix} c_x \\ c_y \\ c_z \end{bmatrix} = (\mathbf{R}^\top \mid -\mathbf{R}^\top \mathbf{t}) \begin{bmatrix} p_x^h \\ p_y^h \\ p_z^h \\ 1 \end{bmatrix}, \quad (3.1)$$

where \mid denotes horizontal matrix concatenation. Note that the resulting point \mathbf{c} in the camera coordinate system is not in homogeneous coordinates.

Next, a projective mapping converts 3D camera coordinates to 2D image coordinates. For simplicity, the projection of points onto the virtual image plane is considered here, instead of projecting onto the image plane (figure 3.4). By doing so, the point reflection of the image is avoided. The transformation is modelled by multiplication with the camera calibration matrix \mathbf{K} as

$$\mathbf{m}^h = \begin{bmatrix} m_x^h \\ m_y^h \\ m_z^h \end{bmatrix} = \begin{bmatrix} fk_x & fs & m_{x0} \\ 0 & fk_y & m_{y0} \\ 0 & 0 & 1 \end{bmatrix} \begin{bmatrix} c_x \\ c_y \\ c_z \end{bmatrix} = \mathbf{K}\mathbf{c}. \quad (3.2)$$

Its parameters are called *internal camera parameters* (e.g. [89, 92]), i.e. focal length f in mm; pixel format k_x, k_y in $\frac{1}{mm}$; pixel skew s , dimensionless; and principal point $[m_{x0}, m_{y0}]$, in pixel [92].

3.2. MEASUREMENT PROCESS AND DATAFLOW

Cartesian coordinates are then recovered through division with m_z^h as

$$\mathbf{m} = \begin{bmatrix} m_x \\ m_y \end{bmatrix} = \begin{bmatrix} m_x^h/m_z^h \\ m_y^h/m_z^h \end{bmatrix}. \quad (3.3)$$

In the case of light sectioning, points in the measurement area of a sensor are assumed coplanar, since they originate from the reflection of a laser plane. Thus, for this specific case, real world coordinates are restricted to an embedded 2D coordinate frame inside the MCS. This 2D coordinate frame is termed *laser plane coordinate system* in the following.

Let, without loss of generality, $p_z = 0$ for all points in the laser plane, i.e. the laser plane is located in the XY-plane of the MCS. Denote the i th column of \mathbf{R}^\top by \mathbf{r}_i , then [92]

$$\begin{aligned} \mathbf{m}^h &= \mathbf{K} (\mathbf{r}_1 \mid \mathbf{r}_2 \mid \mathbf{r}_3 \mid -\mathbf{R}^\top \mathbf{t}) \begin{bmatrix} p_x \\ p_y \\ 0 \\ 1 \end{bmatrix} = \mathbf{K} (\mathbf{r}_1 \mid \mathbf{r}_2 \mid -\mathbf{R}^\top \mathbf{t}) \begin{bmatrix} p_x \\ p_y \\ 1 \end{bmatrix} \\ &= \mathbf{H} \begin{bmatrix} p_x \\ p_y \\ 1 \end{bmatrix}. \end{aligned} \quad (3.4)$$

It can be observed that the relation between laser plane coordinates and ideal image coordinates is modelled as a 2D homography \mathbf{H} , i.e. a transformation from one 2D space into another one. This projective transformation combines the first two steps of the image formation process. The resulting 2D image coordinates \mathbf{m} are in pixels and ideal in a sense that they are not influenced by effects of lens imperfections, e.g. barrel or pincushion distortions. Those two types of geometrical distortions are accounted for in the third step, where the radially symmetric part of Brown's distortion model [93] is applied as

$$\tilde{\mathbf{m}} = \frac{\mathbf{m} + \mathbf{m}_0(\kappa_1\rho^2 + \kappa_2\rho^4)}{1 + \kappa_1\rho^2 + \kappa_2\rho^4}. \quad (3.5)$$

Here $\mathbf{m}_0 = [m_{x0}, m_{y0}]^\top$ denotes the principle point coordinates, $\tilde{\mathbf{m}}$ the distorted point coordinates and ρ the Euclidean distance from the image centre, all in the image coordinate system. It can be observed that only the first two terms of radial distortion are considered. Zhang [88] points out that the distortion is likely entirely dominated by radial components, specifically by the first term, and more sophisticated models would cause numerical insta-

CHAPTER 3. PROTOTYPE COORDINATE MEASURING SYSTEM DESCRIPTION

bility. In the last step, sampling, the discrete nature of the sensor is modelled, i.e. point coordinates in image space are rounded to integers.

The internal camera parameters are determined by camera datasheet information and external camera parameters are estimated by a variant [94] of the Direct Linear Transform (DLT), also known as eight-point algorithm [95]. By experiments, results with datasheet information were compared to results obtained by classical calibration of internal camera parameters [88]. It was found that differences were negligible and thus datasheet information was declared sufficiently accurate. An adapted variant [94] of the plumed line method [93] is used for lens distortion estimation. During experiments, values in the order of 10^{-8} for the first radial distortion term and of order 10^{-15} for the second order term were observed.

With radial distortion terms, internal camera parameters and external camera parameters available, the image formation process can be inverted to obtain distance measurements from image data as discussed in the next section.

3.2.2 Sensor-wise data processing

The following sections describe data processing steps, to be applied for all sensors separately (figure 3.5). First, the triggering methodology, i.e. the signalling to start a measurement, is shortly outlined, then laser line extraction and coordinate transformation are described.

Measurement trigger

In order to initiate a measurement with the laser scanner, a trigger signal is sent to all light sectioning sensors. The same signal is used to read the z-position from the linear motion system and temperature information from the pyrometers. By using a single electrical signal, a nearly contemporary data acquisition from all subsystems can be guaranteed. This synchronisation between data acquisition from sensors and z-position readout is crucial to assign each sensors dataset, i.e. a cross-sectional measurement, a corresponding z-position. The trigger signal is generated by dedicated hardware to ensure a fixed time interval between measurements, e.g. 320 Hz for the discussed application. In contrast, software based triggering does not ensure a constant measurement frequency if the operating system does not provide realtime capability. Typical operating systems, such as the utilised Microsoft Windows XP Embedded, do not guarantee such determinism.

3.2. MEASUREMENT PROCESS AND DATAFLOW

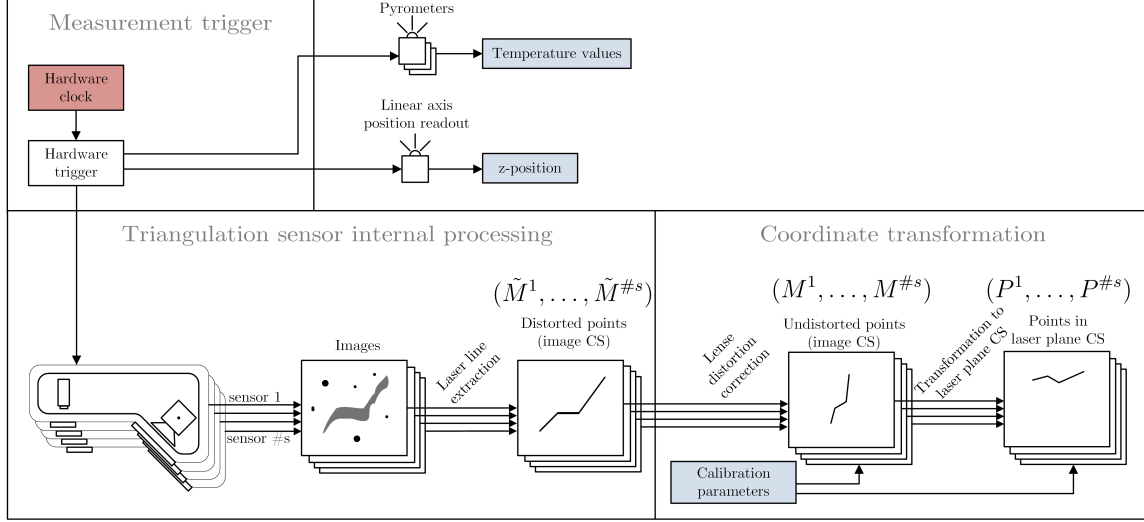


Figure 3.5: Dataflow of sensor-wise measurement data processing, including triggering.

Laser line extraction

As a first data processing step, the laser line is extracted from the recorded intensity image. This is typically done column-wise, i.e. the position of the laser line in each column of the image matrix is calculated [96] (figure 3.6). In the prototype CMS, a proprietary algorithm named "Peak Detector" from Aqsense [97] is used. The algorithm is readily implemented on a FPGA inside each sensor. Such a hardware implementation allows to circumvent the bottleneck of the cameras GigE Vision interface [98], since only the calculated line positions (2048 double precision values) and not whole images (1088 x 2048 byte values) are transferred from the sensor to the computer. This corresponds to approx. 7% of the amount of data and allows for the high measurement frequency of 320 Hz (table 3.1). A drawback of such an integration is the fixed line extraction algorithm for which only a limited set of parameters can be adjusted.

After this step, the imaged laser line is represented by an ordered pointset $\tilde{M}^s = (\tilde{\mathbf{m}}_1, \tilde{\mathbf{m}}_2, \dots, \tilde{\mathbf{m}}_{\#p^s})$ of $\#p^s$ points $\tilde{\mathbf{m}}_i = [m_x, m_y]^\top$ in the camera coordinate system of sensor s . The set is ordered by ascending x-values. The x-coordinates m_x are integers and the y-coordinates m_y are, due to the sub-pixel accuracy of the algorithm, double precision values. Note that the distance between two adjacent x-coordinates is related to the sensors lateral resolution and the distance between neighbouring y-coordinates relates to the sensor depth resolution, i.e. the depth resolution is enhanced by the sub-pixel accuracy.

CHAPTER 3. PROTOTYPE COORDINATE MEASURING SYSTEM DESCRIPTION

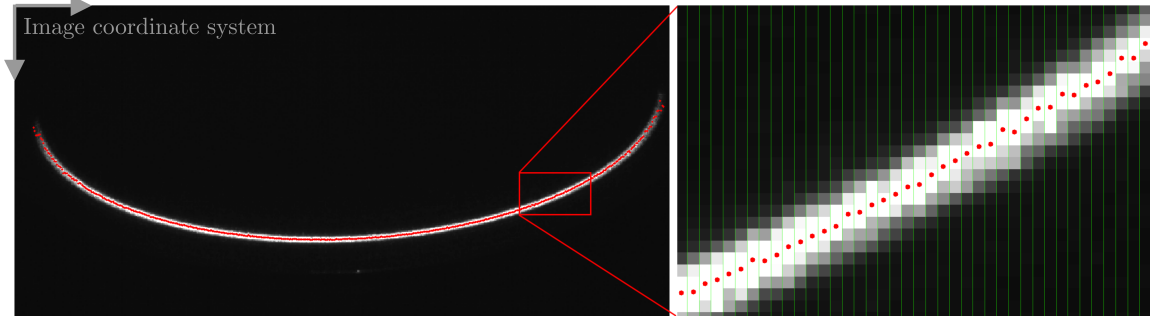


Figure 3.6: Laser line extraction. Left: image with extracted points in red. Right: detail with overlaid green lines that indicate column borders.

Coordinate transformation

Based on results from the camera calibration, points \tilde{M}^s from the image coordinate system are transformed into the laser plane coordinate system. As briefly described in section 3.2.1, the image formation process is applied inversely. The first step is correcting the radial lens distortion by the estimated parameters κ_1 and κ_2 . The corrected coordinates are calculated as

$$\mathbf{m} = \mathbf{m}_0 + (\tilde{\mathbf{m}} - \mathbf{m}_0)(1 + \kappa_1\rho^2 + \kappa_2\rho^4) \quad (3.6)$$

that is equation 3.5 solved for \mathbf{m} . To apply the estimated homography inversely, the undistorted image coordinates \mathbf{m} are firstly converted to homogeneous coordinates as $\mathbf{m}^h = [m_x^h, m_y^h, 1]^\top = [m_x, m_y, 1]^\top$. Then, the inverse homography is applied as

$$\mathbf{p}^h = \begin{bmatrix} p_x^h \\ p_y^h \\ p_z^h \end{bmatrix} = \mathbf{H}^{-1} \cdot \mathbf{m}^h. \quad (3.7)$$

The inverse \mathbf{H}^{-1} is well-defined as long as the camera position is not in the laser plane. Finally, Cartesian point coordinates are recovered as

$$\mathbf{p} = \begin{bmatrix} p_x \\ p_y \end{bmatrix} = \begin{bmatrix} p_x^h/p_z^h \\ p_y^h/p_z^h \end{bmatrix}. \quad (3.8)$$

After this step, sampled laser line positions, i.e. points, are corrected for lens distortion and transformed to the laser plane coordinate system, yielding a pointset $P^s = (\mathbf{p}_1, \dots, \mathbf{p}_{\#p^s})$ for each sensor s . At this stage, sensors are capable of distance measurements.

3.2.3 Data fusion for constant cross-sectional workpieces

The process of combining information from multiple sensors to improve metrological evaluation is termed data fusion. The following procedures are involved in data fusion: pre-processing, registration, optimisation, data fusion, data reduction, meshing (optional) and data format conversion (optional) [99]. From that, it can be seen that the term data fusion is also used for the actual procedure of fusing datasets, i.e. creating one dataset from multiple.

The prototype CMS exhibits a mixture of complementary and competitive sensor configurations [99]. In a complementary configuration, sensors record different regions of a workpiece and their data complements to each other. In contrast, in overlapping regions, where data from different sensors represents the same physical geometry, the configuration is competitive as redundant data is present.

In this section, fusing pointsets P^s from different sensors into a single pointset Q is described for constant cross-sectional products (figure 3.7). First, necessary assumptions are discussed which enable a simplified registration and fusion process. The next sections then discuss these processes.

Prerequisites and assumptions

For the application on "endless" constant cross-sectional workpieces, e.g. profiles from extrusion lines, the meshing procedure must be able to work in realtime to obtain a live view of the measurement result. Moreover, the meshing frequency must be at least as high as the frequency of the laser scanner. If this requirement is not met, the delay between measurement of cross-sections and surface reconstruction steadily increases what is unacceptable for live viewing purposes. Consequently, the performance of data fusion and meshing processes for "endless" products is paramount.

It shall be pointed out that, for constant cross-sectional workpieces, laser planes are assumed perfectly coplanar after manual adjustment of sensors. This assumption does not hold in reality, due to imperfections in the sensors mountings and finite precision by manual adjustment.

Although, it was shown that, for constant cross-sectional workpieces, adjustment of sensors by mechanical means with classical tools, e.g. a goniometer, to reach approximate

CHAPTER 3. PROTOTYPE COORDINATE MEASURING SYSTEM DESCRIPTION

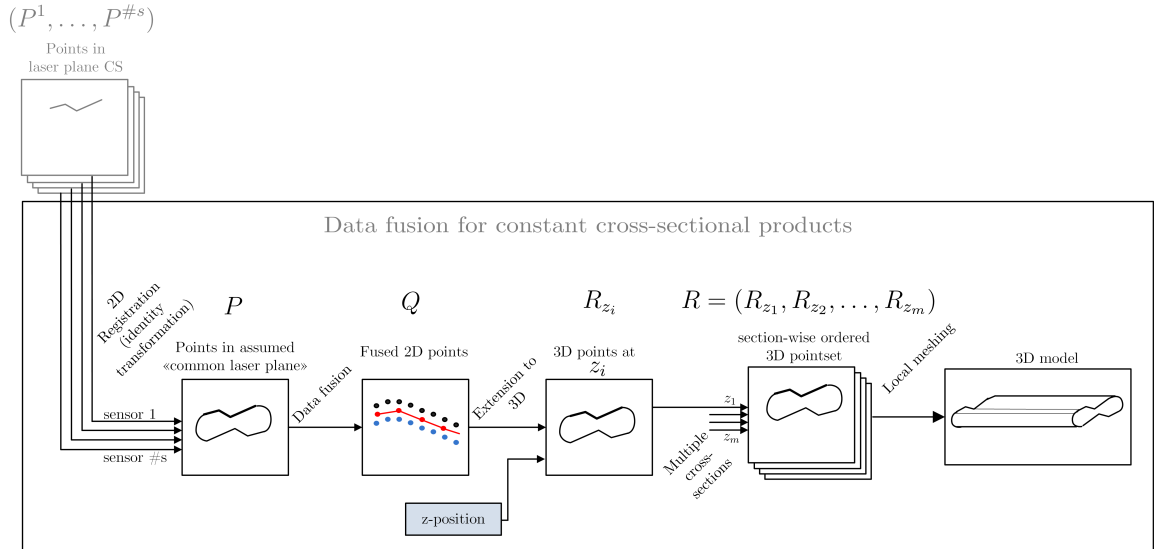


Figure 3.7: Dataflow of data fusion for constant cross-sectional products. Inputs are measurement points from all sensors, the output is an approximation of the workpiece’s surface.

coplanarity and assuming perfect coplanarity is sufficient [42]. By subsequent 2D registration, a negligible influence of sensor alignment on diameter measurements was shown. Experiments were conducted on a similar system with 100 mm measurement area, on a workpiece with diameter of approx. 19 mm with 0.6 deg of sensor misalignment, where an influence of less than 20 μm was concluded [42]. For the target MPE of length measurement of 0.2 mm, this effect can be neglected, especially since the sensor misalignment for constant cross-sectional workpieces on the prototype CMS was below 0.6 deg for all involved sensors (section 3.2.4).

Moreover, orthogonality between all laser planes and the linear motion system axis is assumed. By this, all points in sets P and Q have the same z -value. This arrangement is approximated by proper mechanical setup of the CMS. Further, it is presumed that each cross-section consists of a single, closed contour, i.e. there is only a single workpiece in the measurement volume, without holes or branches. This restriction is feasible for the typical geometries of constant cross-sectional products like profiles or bars and significantly simplifies the fusion and meshing steps.

If measuring constant cross-sectional products and the coplanarity assumption is violated by mutual translation of laser planes along the linear motion system axis, i.e. the MCS Z -axis, this effect is not necessarily visible in the measurement data (figure 3.8). Since nominal cross-sections are constant, i.e. they have one degree of invariance, in contrast to

3.2. MEASUREMENT PROCESS AND DATAFLOW

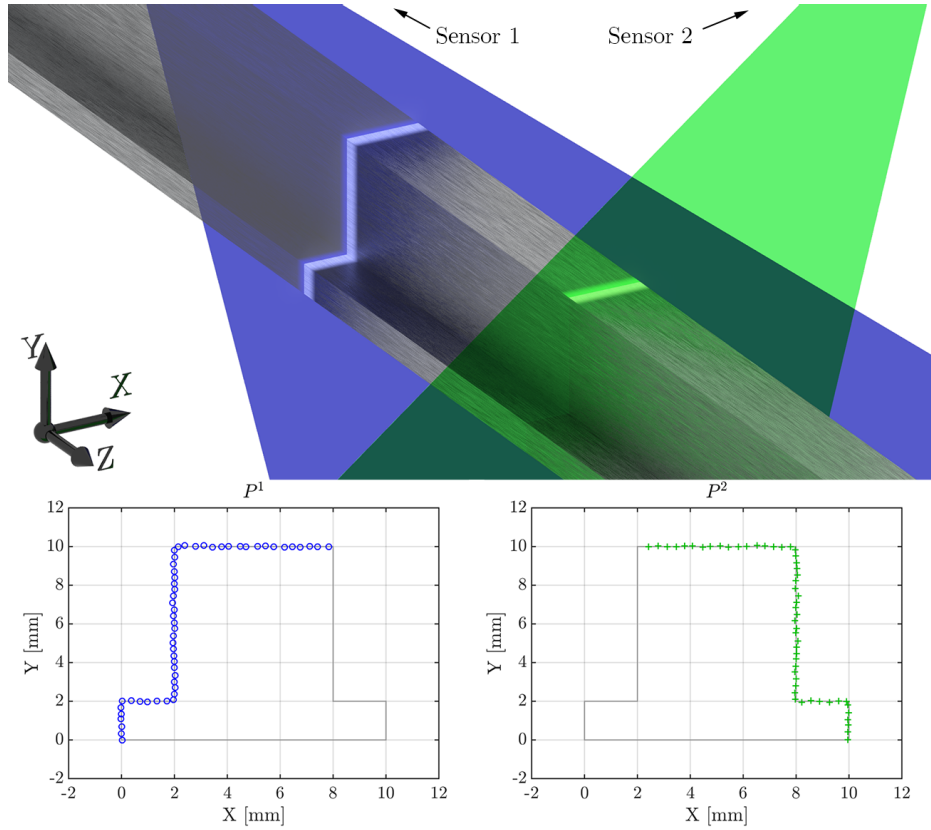


Figure 3.8: Top: render of two laser planes with different position on the Z-axis. Bottom: the resulting pointsets P^1 and P^2 for the two sensors. The discrepancy in the z-position is not visible in the data.

freeform workpieces, ideal features on different cross-sections are identical and pointsets from different cross-sections fit seamlessly together.

In section 3.2.4, it will be demonstrated that the outlined procedure of manual sensor adjustment combined with 2D registration is not sufficient for the intended measurements on non-constant cross-sectional workpieces.

Data registration

Typically, camera calibration is done independently per sensor. Thus, registration of datasets from multiple sensors is necessary to represent all datasets in a single coordinate system [99]. With the assumption of coplanar laser planes, a 2D registration is sufficient, e.g. by the Iterative Closest Point (ICP) algorithm [100].

CHAPTER 3. PROTOTYPE COORDINATE MEASURING SYSTEM DESCRIPTION

Due to the proprietary external camera parameter estimation (section 3.2.1), however, this step is not required. By simultaneous calibration of multiple sensors with one single artefact, the laser plane coordinate systems from all sensors coincide. Thus, measurement data from all sensors is already represented in a common 2D coordinate system and the registration is performed by creating the union of all datasets as $\check{P} = \{P^1 \cup P^2 \cup \dots \cup P^{\#s}\}$ where $\#s$ denotes the number of sensors in the system. Additionally, the set of sensor sets is utilised when appropriate, i.e. $P = \{P^1, P^2, \dots, P^{\#s}\}$.

Data fusion

The CMS uses an averaging filter for fusing sensor datasets, i.e. for the extraction of a single dataset that represents the cross-section. An optimisation step is not performed, thus, all measurement points have equal influence on the fused result.

The averaging filter searches, e.g. for each point \mathbf{p} in P^1 , neighbouring points from other sensors, i.e. in $P \setminus P^1$, in an adjustable radius. From the found points, an averaged point \mathbf{q} is calculated. Iteratively calculating such averages for each sensors pointset P^s eventually yields a new pointset $Q = (\mathbf{q}_1, \dots, \mathbf{q}_{\#q})$ with $\#q$ points. Usually, $\#q \ll |\check{P}|$, where $|X|$ denotes the cardinality of set X , due to averaging.

This filter is conceptually simple but has some limitations. If applying it to high curvature regions, the surface is over- or underestimated, depending on the sign of curvature (figure 3.10, left). If pointsets from multiple sensors deviate sufficiently, e.g. due to inaccuracies in sensor registration, the filter may produce multiple points for the same surface location (figure 3.10, right); this effect is termed *double lines* in this work.

As an alternative to the simple averaging filter, a data fusion method based on the envelope method [101] was developed by the author. The proposed method is based on the alpha shape [102], which is a generalisation of the convex hull and is applied in e.g. surface metrology [103]. Intuitively, it can be thought of rolling a sphere with radius α over a pointset and thereby creating connectivity information between the points that touch the sphere. The only parameter of this method is the radius α . For $\alpha \rightarrow \infty$, the result approaches the convex hull, for $\alpha = 0$, the result is the pointset itself.

For the considered application on cross-sectional data, the alpha shape is applied on 2D pointsets, specifically over the combined pointset \check{P} from all sensors (figure 3.9, top left). For dispersed, mutually not perfectly matching pointsets, this generates an inner and outer alpha hull around the points (figure 3.9, top right). These hulls, i.e. polylines, can be used twofold, (i) to generate a fused dataset and (ii) to estimate the local dispersion of measurement data.

3.2. MEASUREMENT PROCESS AND DATAFLOW

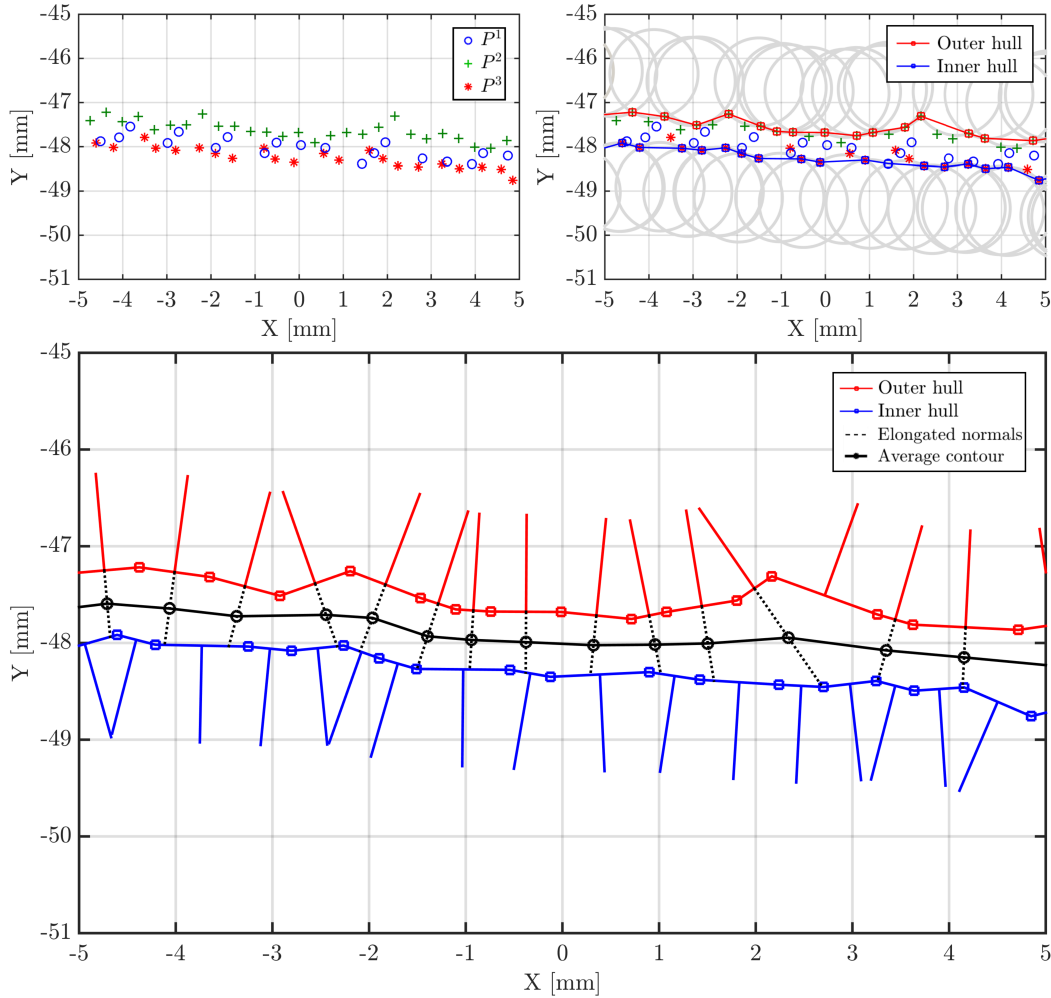


Figure 3.9: Top left: pointsets P^1, P^2, P^3 from three different sensors. Top right: visualisation of the alpha shape construction. Bottom: elongated normals as dashed black line and the resulting average contour as solid bold black line.

The fused dataset Q is generated by elongating the normals from the inner hull towards the outer hull, or vice versa, for each line segment j of the respective polyline, and generating a point q_j at the centre between the hulls (figure 3.9, bottom). This eventually yields an averaged contour, represented as a polyline. Utilisation of more robust methods to extract the average contour, like the Medial Axis Transform (MAT) [104], was considered. Although, elongation of normals was found to be sufficient for the aimed application.

CHAPTER 3. PROTOTYPE COORDINATE MEASURING SYSTEM DESCRIPTION

If more than two alpha hulls are created, e.g. caused by missing points or density variations, a post-processing step connects the generated contours. Connections are constructed by finding the endpoint of another contour with minimal Euclidean distance. As long as the previous assumption of a single, closed contour per cross-section is valid, this step efficiently closes holes in contours.

As shown in figure 3.10, the proposed method outperforms the average filter in terms of contour preservation (figure 3.10, detail 1) and double line averaging (figure 3.10, detail 2). Equal radii for the averaging filter and alpha shape method were used. Nevertheless, due to the respective nature of the algorithms, the alpha shape method typically generates more points along the contour. Moreover, if the radius is chosen sufficiently small, both methods fail at averaging the exemplary double line (figure 3.10, second row). On the other hand, a sufficiently large radius leads to an averaged double line for both methods, but the alpha shape approach is still able to preserve edges to some degree while the averaging filter produces a very coarse result (figure 3.10, last row).

It shall be highlighted that for the discussed application, the produced connectivity information in the fused pointset can be used to traverse Q clockwise or counter-clockwise. This is a convenient result for the meshing step, as will be discussed in the corresponding paragraph.

The second result, dispersion estimation, is evaluated by computing the length of elongated normals between the two hulls. This length is an estimate of the local data dispersion. Figure 3.11 shows a colour-coded scatterplot of this dispersion for multiple cross-sections of a non-constant cross-sectional workpiece, i.e. a gas turbine blade. This workpiece was chosen for demonstration purposes because high dispersion is visible in steep areas, whereas on relatively flat regions the dispersion is moderate.

By the proposed method, applied on a non-constant cross-sectional workpiece, it can be observed, that the previously discussed approach for data fusion is not sufficient for non-constant cross-sectional workpieces, since differences between sensor data up to 2 mm for steep details are present.

Due to the necessary Delaunay triangulation [105] involved in the construction of the alpha shape, the asymptotic time complexity of this method is $\mathcal{O}(n \log n)$, where n is the number of points from all sensors. The potential time complexity of the averaging filter is also $\mathcal{O}(n \log n)$, limited by a nearest neighbour search operation.

3.2. MEASUREMENT PROCESS AND DATAFLOW

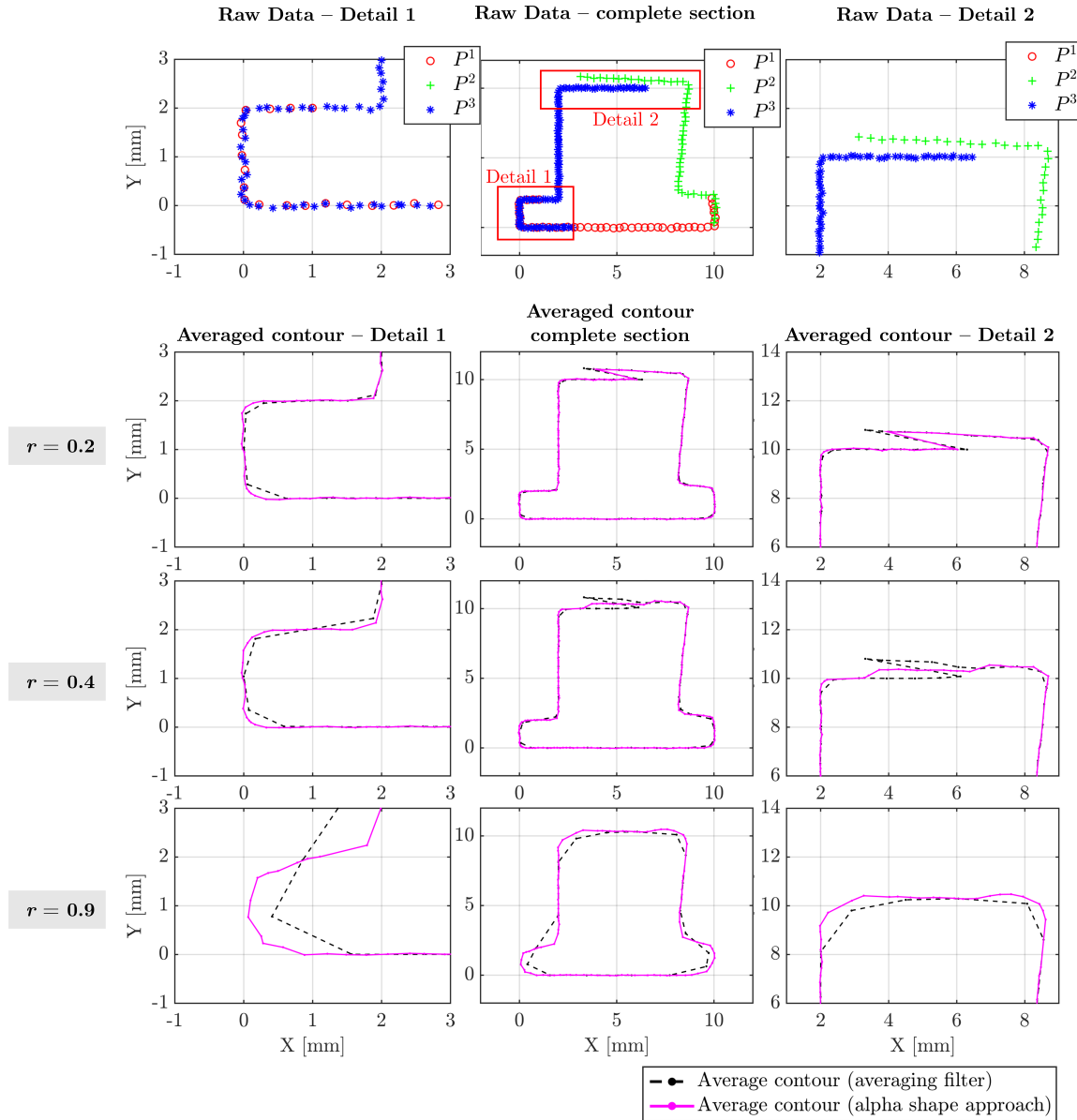


Figure 3.10: Resulting contours for the averaging and alpha shape methods with different filter radii. Measurement points are shown in the top row. The lower rows show results for different radii. The left column shows the behaviour of the methods on edges, the right column depicts a detail where double lines are present.

Extension to 3D

At this point, a fused 2D pointset Q exists, which represents a cross-section of the workpiece. By moving the workpiece with the linear moving system through the 2D scanner, m

CHAPTER 3. PROTOTYPE COORDINATE MEASURING SYSTEM DESCRIPTION

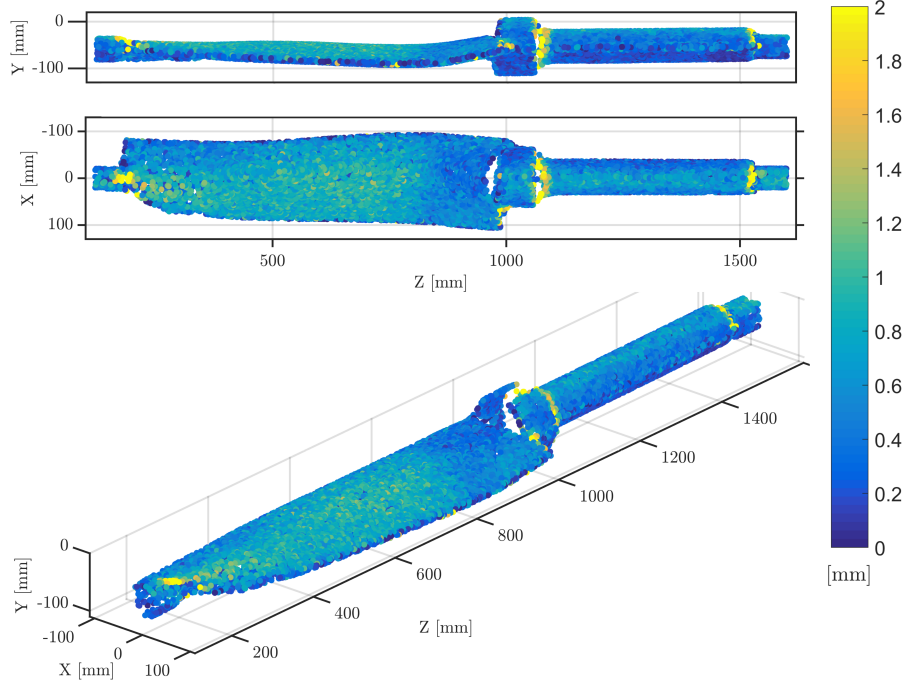


Figure 3.11: Scatterplot of distances between alpha hulls on a turbine blade. Distances are colour-coded.

cross-sections on distinct z -positions are measured, yielding the pointsets $(Q_{z_1}, Q_{z_2}, \dots, Q_{z_m})$. By the orthogonality assumption, the z -coordinate for all points in Q_{z_i} is equal to the position z_i of the linear motion system axis. Thus, the extension to 3D coordinates is simply

$$\mathbf{r} = \begin{bmatrix} q_x \\ q_y \\ z_i \end{bmatrix}, \quad \begin{bmatrix} q_x \\ q_y \end{bmatrix} = \mathbf{q} \in Q_{z_i}. \quad (3.9)$$

The set of all \mathbf{r} 's, from all z -positions, is the final pointset, i.e. $\check{R} = (R_{z_1} \cup R_{z_2} \cup \dots \cup R_{z_m})$ which represents the 3D workpiece surface. Again, also a set-wise representation shall be defined as $R = (R_{z_1}, R_{z_2}, \dots, R_{z_m})$.

Meshing

For measurements in-between cross-sections and for visualisation purposes, a 3D pointset is typically not sufficient. Representation of the surface would improve the visualisation for

operators and yields interpolated holistic information, regarding surface geometry. Moreover, for "endless" constant cross-sectional workpieces, e.g. application in an extrusion line, a live visualisation of the workpiece surface is desirable.

To generate a linearly approximated surface from the measurement points, a fast heuristic meshing method was developed by the author and is discussed in this section. Only triangle meshes, which approximate the surface with many triangles, are considered. The focus is on triangles due their simplicity and widespread support in modern software packages, e.g. represented in the STL file format [106]. In order to avoid confusion with optical triangulation, the more general term *meshing* is used here, instead of *surface triangulation*, to refer to surface reconstruction with triangles.

A triangle surface is typically rendered only on its front side, which is in direction of the triangle normal and defined by its orientation [107]. The orientation, and thereby the direction of its normal, is usually specified by the order of its *vertices*, i.e. triangle corners defined by points [107] and can be found by applying the right-hand rule. Or, more formally, the normal of a triangle $\triangle(\mathbf{p}_1, \mathbf{p}_2, \mathbf{p}_3)$, with points \mathbf{p}_1 , \mathbf{p}_2 and \mathbf{p}_3 as its vertices, is given by $\frac{\mathbf{p}_3 - \mathbf{p}_2}{|\mathbf{p}_3 - \mathbf{p}_2|} \times \frac{\mathbf{p}_2 - \mathbf{p}_1}{|\mathbf{p}_2 - \mathbf{p}_1|}$, where \times denotes the cross product. The vectors $(\mathbf{p}_3 - \mathbf{p}_2)$ and $(\mathbf{p}_2 - \mathbf{p}_1)$ make up two *edges*, i.e. sides, of the triangle and their direction is also defined by the vertex order.

It should be noted that some of the discussed methods in this chapter do not only create a surface approximation, but also perform tetrahedralisation [108, 109], i.e. they subdivide the volume inside an object into tetrahedra. Though volumetric subdivision is necessary in several fields, e.g. as input for FEM simulations, it is not discussed here. For the aimed metrological application, the surface geometry is sufficient.

A variety of methods for meshing 3D pointsets exists: power crust [110], ball-pivoting algorithm [111] and Poisson surface reconstruction [112], to name only a few. For such methods, the input is an unordered 3D pointset. However, with points that are grouped per cross-section, additional information is implicitly available, i.e. by assuming a single workpiece, adjacent cross-sections are connected to each other.

This special case, where data is available section-wise, is encountered in Geographical Information Systems (GIS) [113, 114], medical technologies (e.g. Magnetic Resonance Imaging (MRI) with Multi-Slice 2D Imaging [115], serial section Transmission Electron Microscopy (ssTEM) [116], Serial Block Face Scanning Electron Microscopy (SBF-SEM) [117], Computed Tomography (CT) [118] (in configuration: line sensor and non-helical scanning) and obviously technologies from optical metrology, e.g. confocal microscopy [10], focus variation [10], CT for dimensional metrology [118] (in configuration: line sensor and non-helical scanning) and light sectioning [56]. With some of these technologies,

CHAPTER 3. PROTOTYPE COORDINATE MEASURING SYSTEM DESCRIPTION

cross-sections are initially not represented by contours but e.g. images, from which isolines must be extracted. However, this step is not necessary in the case of light sectioning.

Triangular meshing methods for parallel cross-sections (also serial parallel contours [119] or serial planar contours [120]) exploit this additional information of connectivity between cross-sections. Pointsets from two adjacent cross-sections are taken as input and triangles with their vertices at the point locations are generated between them (figure 3.12). This process is iterated for all cross-sections to generate a complete surface approximation. However, even for the relatively simple case, where each involved cross-section consists of only one contour, the solution is not trivial. Meshing from parallel cross-sections can be subdivided into three fundamental problems [121]:

- The *tiling problem* is defined as the construction of a triangular mesh between two adjacent contours in order to generate a "good" topological adjacency. The problem is severely underconstrained since many different meshes are feasible to connect two contours. Thus, an objective function to quantify the "goodness" of the mesh has to be defined e.g. by volume [122], surface area [123] or span length [108, 119, 124, 125].
- Cases where cross-sections consist of multiple disconnected contours pose the *correspondence problem*, i.e. which contour of a cross-section should be connected to which one in the next cross-section?
- Additionally, if there exists a different number of contours in adjacent cross-sections, connections from one to multiple contours may become necessary. Meshing one-to-many contours is known as the *branching problem*.

To solve these problems, optimisation (e.g. [122, 123]), heuristic (e.g. [108, 119, 124–126]) and hybrid approaches (e.g. [120, 127, 128]) were proposed. Optimisation methods use global objective functions (e.g. for the tiling problem: maximise global volume between contours [122]) that are optimised and are thus usually computationally expensive [119, 124]. In contrast, heuristic methods use local objective functions (e.g. for the tiling problem: minimise span of the next triangle to construct [108, 119, 124, 125]) which are relatively cheap to compute.

To guarantee maximum performance in meshing of relatively simple workpieces¹, a heuristic approach was chosen by the author. Additionally, the branching and correspon-

¹In computer graphics, very complex geometries as the Stanford Bunny or Stanford Dragon are typically used to demonstrate the performance of meshing algorithms. In relation to such geometries, constant cross-sectional workpieces have a simple geometry.

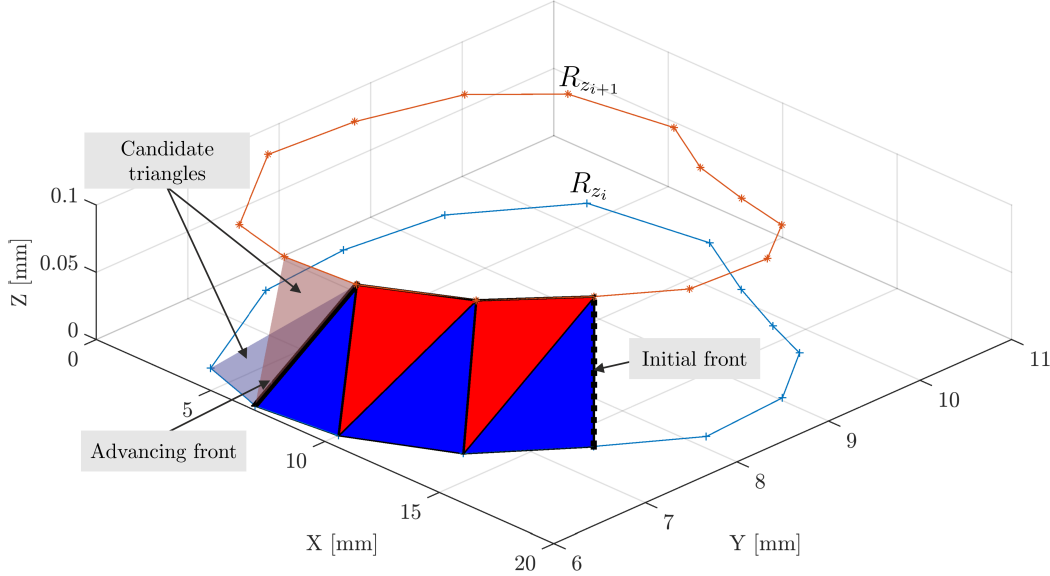


Figure 3.12: Pointsets R_{z_i} (blue) and $R_{z_{i+1}}$ (red) as polygons during the meshing process. Based on the local objective function, one of the two candidate triangles is created and the advancing front is updated.

dence problems between contours do not occur, as it is assumed that each cross-section consists of only one closed contour. Both problems are therefore intentionally not addressed to maximise performance.

One advantage of meshing methods for parallel cross-sections, in contrast to global meshing algorithms, that is known [129] but barely considered in literature, is the possibility of simple parallelisation. Since meshing of pointset R_{z_i} with the adjacent pointset $R_{z_{i+1}}$ is independent of meshing $R_{z_{i+1}}$ with $R_{z_{i+2}}$, a coarse parallelisation is achievable with little effort. Parallelism in computer programs is inevitable to utilise the computing power of modern systems since Moore's law does not hold any more for single processing units [130].

For a solution of the tiling problem, heuristic approaches usually use one or more so-called *advancing fronts*, i.e. a line connecting two points of the respective pointsets involved (figure 3.12). Taking two adjacent clock-wise ordered pointsets, say R_{z_i} and $R_{z_{i+1}}$, the initial advancing front is e.g. generated by finding the point in $R_{z_{i+1}}$ which has minimal Euclidean distance to $\mathbf{r}_{z_i,1}$, i.e. an arbitrary starting point in cross-section R_{z_i} . The line between them is used as initial front (figure 3.12). Starting with these two points as triangle vertices, the third vertex for the triangle to create is the next point in R_{z_i} or $R_{z_{i+1}}$. The decision between the two candidates is made by a local objective function. The advancing

CHAPTER 3. PROTOTYPE COORDINATE MEASURING SYSTEM DESCRIPTION

front is updated to the newly created edge between the two contours (figure 3.12) and the process repeats.

Next points in each contour, e.g. in a clock-wise sense, are known due to available connectivity information, generated by the alpha shape method for data fusion. If the averaging filter in combination with an advancing front heuristic is used, an additional, non-trivial point sorting step is required.

One prominent and simple local objective function is taking the point with minimum span length [108, 119, 124, 125]. The *span* is defined as the next advancing front, generated by the respective point. Additional to the minimum span length, Chae & Lee [124] use a so-called *warping criterion* that approximates local volume maximisation. For that purpose, define the angle α_{i+1} between a candidate triangle normal, with its new vertex from $R_{z_{i+1}}$, and the vector from its centre to the next point in R_{z_i} (figure 3.13). If $\alpha_{i+1} > 90$ deg, the candidate triangle is in front of the alternative one, and the volume is locally maximised by choosing $R_{z_{i+1}}$. Chae & Lee [124] use the criterion $\alpha_{i+1} > (90 + \epsilon)$ deg though, where ϵ was set by the authors to 40 deg. The purpose of this offset is to maintain well-conditioned triangles, as reported by the authors.

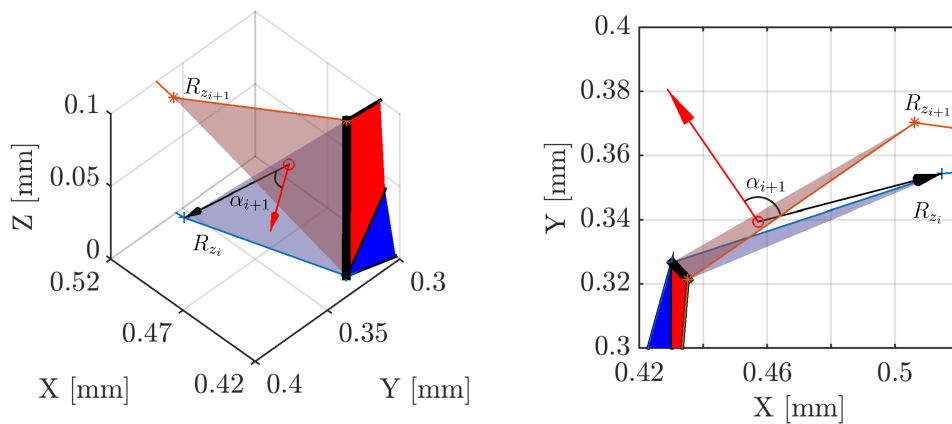


Figure 3.13: Warping criterion visualisation for the candidate triangle with its vertex from $R_{z_{i+1}}$ (light red). The angle between its normal (red vector) and the vector from its centre to the next point in R_{z_i} (black vector) is α_{i+1} . Left: view of the candidate triangles. Right: top view.

Maximisation of volume produces well-conditioned surfaces in convex regions, but not in concave regions as discussed by Keppel [122] in his pioneering work about meshing for parallel cross-sections. He separates contours into convex and concave regions and then finds a surface reconstruction with maximal and minimal volume, respectively. Therefore, he formulates the meshing problem as a computationally intensive combinatorial optimisa-

3.2. MEASUREMENT PROCESS AND DATAFLOW

tion problem. This idea of locally constrained volume maximisation was incorporated into the heuristic algorithm of [124] by the author. The resulting adapted algorithm is described in the following.

The advancing front procedure iterates over all adjacent pairs of contours. For each pair, the initial advancing front is determined. Then triangles are created, based on the local objective function, until all points are visited. The result is an unordered set of triangles that represents the approximated surface.

Algorithm 1 lists the modified local objective function, which returns `true` if the next point in contour R_{z_i} is to be used as triangle vertex and `false` if the next vertex is to be taken from $R_{z_{i+1}}$. As parameters, the previous, current and next contour points from both, R_{z_i} and $R_{z_{i+1}}$ are provided to calculate the local curvature. Note that the unit radiant is used in the algorithm. The notation $\perp \Delta(\mathbf{p}_1, \mathbf{p}_2, \mathbf{p}_3)$ denotes the normal vector of triangle $\Delta(\mathbf{p}_1, \mathbf{p}_2, \mathbf{p}_3)$, as defined by the vertex order. Define $\angle(\mathbf{v}_1, \mathbf{v}_2)$ as the angle between vector \mathbf{v}_1 and \mathbf{v}_2 with target set $[0, \pi]$. Further define the angle between a vector \mathbf{v}_1 , projected onto the XY-plane, and the X-axis by $\sphericalangle(\mathbf{v}_1)$ with target set $[0, 2\pi]$.

Algorithm 1 Adapted local objective function, based on [124].

The author's contribution is highlighted with shaded background.

```

1: function LOCALOBJECTIVE( $\mathbf{r}_{z_i, k-1}, \mathbf{r}_{z_i, k}, \mathbf{r}_{z_i, k+1}, \mathbf{r}_{z_{i+1}, l-1}, \mathbf{r}_{z_{i+1}, l}, \mathbf{r}_{z_{i+1}, l+1}$ )
2:    $N_i \leftarrow \perp \Delta(\mathbf{r}_{z_i, k}, \mathbf{r}_{z_i, k+1}, \mathbf{r}_{z_{i+1}, l})$ 
3:    $N_{i+1} \leftarrow \perp \Delta(\mathbf{r}_{z_i, k}, \mathbf{r}_{z_{i+1}, l+1}, \mathbf{r}_{z_{i+1}, l})$ 
4:    $\alpha_{i+1} \leftarrow \angle((\mathbf{r}_{z_i, k+1} - \mathbf{r}_{z_i, k}), N_{i+1})$ 
5:    $\alpha_i \leftarrow \angle((\mathbf{r}_{z_{i+1}, l+1} - \mathbf{r}_{z_{i+1}, l}), N_i)$ 
6:    $\beta_i \leftarrow (\sphericalangle(\mathbf{r}_{z_i, k+1} - \mathbf{r}_{z_i, k}) - \sphericalangle(\mathbf{r}_{z_i, k} - \mathbf{r}_{z_i, k-1}) + \pi) \bmod (2\pi) - \pi$ 
7:    $\beta_{i+1} \leftarrow (\sphericalangle(\mathbf{r}_{z_{i+1}, l+1} - \mathbf{r}_{z_{i+1}, l}) - \sphericalangle(\mathbf{r}_{z_{i+1}, l} - \mathbf{r}_{z_{i+1}, l-1}) + \pi) \bmod (2\pi) - \pi$ 
8:    $\epsilon_i \leftarrow (1 - b \cdot \tanh(a\beta_i))$ 
9:    $\epsilon_{i+1} \leftarrow (1 - b \cdot \tanh(a\beta_{i+1}))$ 
10:  if  $\alpha_i > (\pi/2 + \epsilon_i)$  then return true
11:  else if  $\alpha_{i+1} > (\pi/2 + \epsilon_{i+1})$  then return false
12:  else if  $\|\mathbf{r}_{z_i, k+1} - \mathbf{r}_{z_{i+1}, l}\| < \|\mathbf{r}_{z_{i+1}, l+1} - \mathbf{r}_{z_i, k}\|$  then return true
13:  else return false

```

Following [124], the candidate triangle normals and the angles α_i and α_{i+1} are determined (algorithm 1, line 2 to 5).

CHAPTER 3. PROTOTYPE COORDINATE MEASURING SYSTEM DESCRIPTION

Instead of plugging those values directly into the warping criterion, as in [124], the local curvature of both contours is calculated as β_i and β_{i+1} (line 6 and 7). Note that β is the signed angular difference and comprised between $-\pi$ and π . The respective offsets, ϵ_i and ϵ_{i+1} are then evaluated by use of a sigmoidal, i.e. hyperbolic tangent function (line 8 and 9) with parameters β_i , β_{i+1} and two tuning parameters, a and b .

If α_i is larger than $(\pi/2 + \epsilon_i)$ rad, the next point in R_{z_i} is chosen by use of the warping criterion (line 10). If this expression is false, the warping criterion for contour $R_{z_{i+1}}$ is checked (line 11). If none of the previous expressions evaluates to true, the minimum span length criterion is applied (line 12 and 13).

Exemplary meshing results by applying minimum span length criterion, the method from [124] and the proposed adapted method are shown in figure 3.14. The light green triangles display usage of the warping criterion. In the shown example, it is evident that the minimum span length criterion does not produce well-conditioned surfaces (figure 3.14, top). Chae & Lee’s method (figure 3.14, middle) performs better but still produces rather artificial surfaces, visible e.g. in the concave region at $(x = 50, y = 25)$ where the warping criterion is applied. By the proposed modification, the warping criterion is applied locally adaptive and the artefacts that originate from volume maximisation in concave regions vanish (figure 3.14, bottom). The improved quality of generated surfaces by the proposed approach was assessed empirically by multiple real workpieces.

It should be pointed out that the curvatures β_i and β_{i+1} are approximated in a highly local sense, i.e. by the current point and two directly neighbouring points. Experiments with up to four neighbours were conducted and no significant improvement was evident in meshing typical workpieces.

The asymptotic time complexity of this heuristic method is relatively low, i.e. $\mathcal{O}(n)$, where $n = |\tilde{R}|$. A C++ implementation meshes approx. 210 000 points per second on a state-of-the-art commercial laptop². With typical geometries, the number of points per contour after data fusion is approximately 500. Thus, the performance is in the order of 420 contours per second, what is sufficient for the measurement frequency of 320 Hz. Note that this implementation is not yet parallelised, what would increase the performance by a factor in the order of available processing units.

The algorithm was implemented in Scilab 5.5.0 [131] and MATLAB 2015a [132] for laboratory use. It was verified and adopted by Zumbach Electronic AG [41] during experiments in the context of the Eurostars HOTGAUGE (E!6692) project and is now implemented in C++ language into their proprietary CMS software.

²Intel Core i7-4700MQ @2.4 GHz, 8 GB RAM, Windows 7

3.2. MEASUREMENT PROCESS AND DATAFLOW

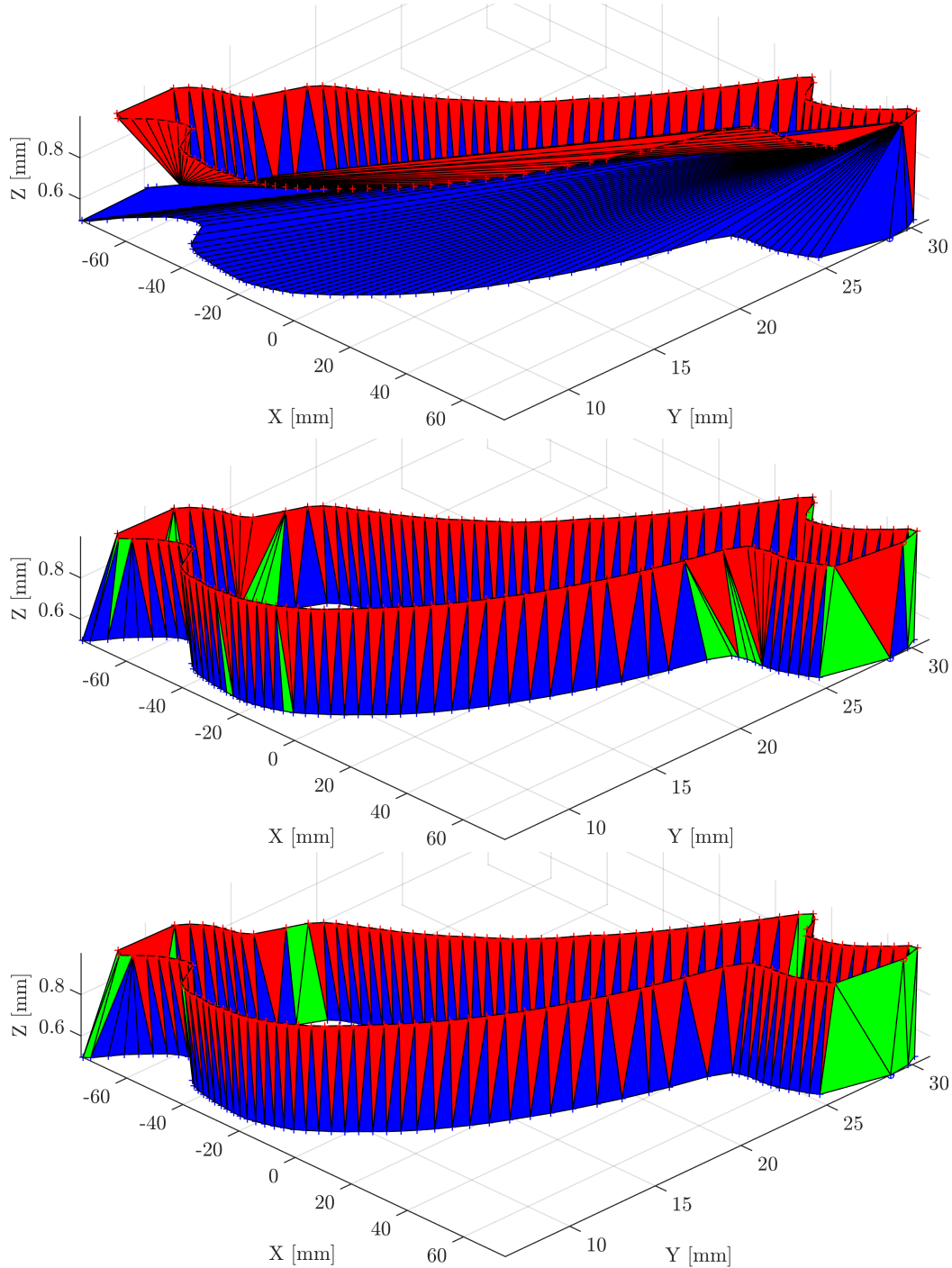


Figure 3.14: Meshes generated by different local objective functions. Light green triangles indicate usage of the (modified) warping criterion, red and green triangles indicate the use of the minimum span length criterion. The Z-axis is magnified for better clarity. Top: minimum span length. Middle: Chae & Lee [124]. Bottom: proposed method.

3.2.4 Data fusion for non-constant cross-sectional workpieces

As briefly discussed in the previous section, sensor alignment, manually optimised by an experienced operator, as conventionally done for constant cross-sectional products, was not sufficient for the application on non-constant cross-sectional workpieces, e.g. gas turbine blades [18, 84].

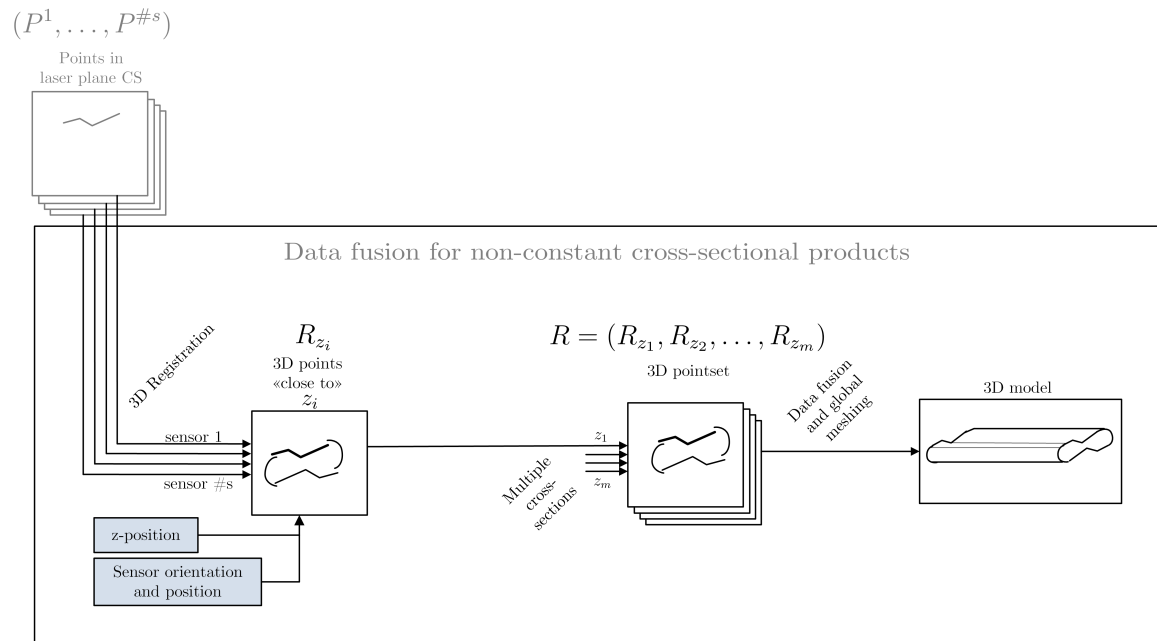


Figure 3.15: Dataflow of data fusion for non-constant cross-sectional products. Inputs are measurement points from all sensors, the output is an approximation of the workpiece’s surface.

In this section, a method for automatic determination of sensors positions and orientations in multisensor laser triangulation CMS is presented. Based on a series of measurements on a conical artefact without the use of external light sources, the approach allows for both, optimised adjustment of the physical sensors and improved 3D data registration by software (figure 3.15).

For non-constant cross-sectional workpieces, the effect of sensor misalignment is more severe since the slope of the workpiece along the linear motion system axis directly affects its sensitivity. A schematic representation of a conical workpiece with high slope is shown in figure 3.16, where an offset normal to the nominal measurement area results in a different measured radius (figure 3.16, left) and a rotational misalignment results in a distorted dataset (figure 3.16, right). This correlation will be formalised in chapter 4.

3.2. MEASUREMENT PROCESS AND DATAFLOW

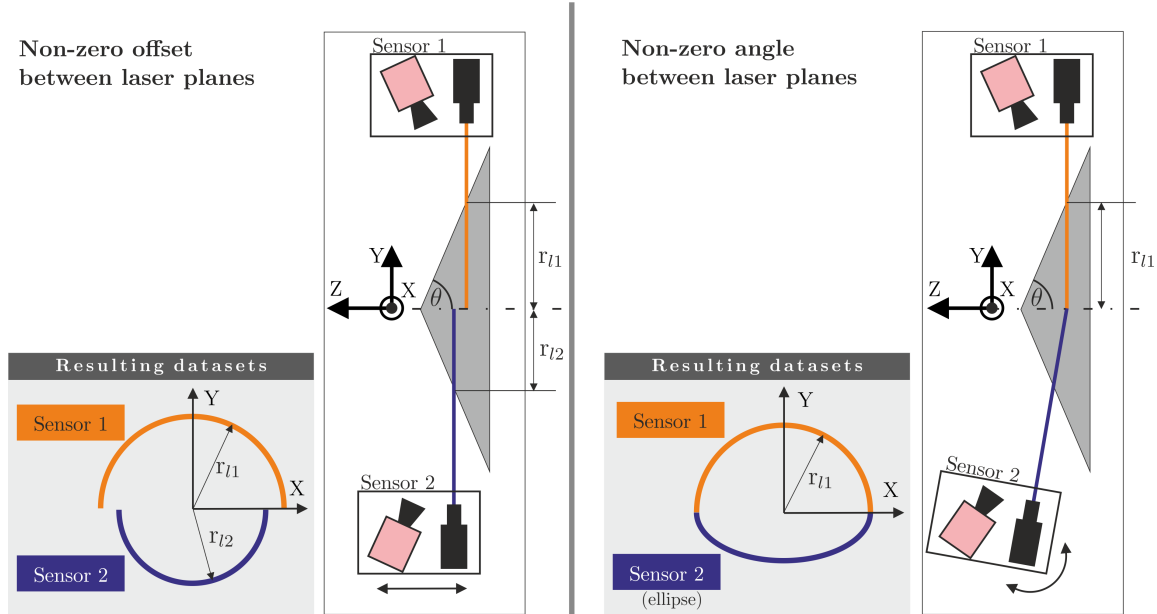


Figure 3.16: Sensor misalignments. Left: translational misalignment. Right: rotational misalignment.

The sensor alignment is particularly important for systems with a large measurement area, in which small misalignments result in large deviations between laser planes. To minimise the imperfect alignment effects for measurements on non-constant cross-sectional workpieces, a method that improves the adjustment process is necessary. Alternatively, a method that allows for accurate 3D data registration of sensor data could be used to minimise the misalignment effects by software means.

The registration of data from multiple sensors (transformation into a common coordinate system) can be obtained by different methods: (i) knowledge about the relative sensor positions and orientations, (ii) application of markers on the workpiece or (iii) numerical optimisation methods to minimise the distances between datasets [99].

To estimate rigid 3D transformations by method (ii) and (iii), 3D sensor coordinate systems are necessary. The discussed triangulation sensors work, however, with 2D coordinate systems. The linear axis can be considered as a third axis, jointly for all sensors but orthogonality between these axes is not guaranteed. Furthermore, for industrial application, a moving axis is not necessarily available at the manufacturers' site. Therefore, for initial adjustment by the manufacturer, a method that works without linear axis is required.

If the sensors coordinate systems are considered instead as 2D spaces, i.e. without additional linear axis, methods (ii) and (iii) become infeasible to estimate a 3D transformation. Due to the 2D nature of the sensor datasets, corresponding data from sensors in the common

CHAPTER 3. PROTOTYPE COORDINATE MEASURING SYSTEM DESCRIPTION

3D coordinate system are in almost all cases collinear (corresponding data lying on a line) or there is no correspondence at all. Thus, methods (ii) and (iii) are typically not sufficient to determine the six degrees of freedom of a rigid 3D transformation for 2D sensor data. Consequently, the focus is on method (i) and the sensors coordinate systems are considered as 2D spaces.

Tratnig et al. [133] propose two methods to determine the relative position and orientation of multiple light sectioning sensors. Results are given for bidirectional length measurements on a constant cross-sectional part. They state a deviation of $24\ \mu\text{m}$ and $28\ \mu\text{m}$ respectively for the two methods w.r.t. a reference workpiece, as evaluated by a single measurement. Both methods use, additionally to the laser light, an external light source. However, in order to reduce the influence of extraneous light, triangulation sensors often use short exposure times and optical bandpass filters. In consequence, a high-energy light source or changing the sensors exposure time become necessary.

Zhang et al. [134] use a calibration plane to estimate extrinsic camera parameters of light sectioning sensors. Subsequently, they use a custom artefact to adjust a laser plane to coincide with this calibration plane by moving the artefact along an additional axis. The laser light coming from four to six sources is considered as a single plane.

The present work describes an algorithmic procedure and an appropriate physical artefact to estimate the sensor alignment without need for an additional linear axis and without an external light source. The results can be used twofold: (i) to guide the manual adjustment process and quantify the residual error due to misalignment and (ii) to register the sensor datasets ($P^1, \dots, P^{\#s}$) by software means.

In the next section, the proposed method is described. Then, a sensitivity analysis by means of simulation is presented and experimental results are discussed.

Method description

The method assumes a coarse manual pre-adjustment of sensors to ensure the lateral surface of the artefact is inside the measurement area of all sensors at once. Further, the internal (e.g. focal length, principle point) and external (position and orientation w.r.t. laser plane) camera parameters must have been determined for each sensor [89]. I.e., the light sectioning sensors must be calibrated. Thus, a correlation between a point $\mathbf{m} = [m_x, m_y]^T$ in the camera coordinate system (2D, in pixel) and the corresponding point $\mathbf{p} = [p_x, p_y]^T$ in its laser plane coordinate system (2D) is available.

Preliminary registration Firstly, the laser planes of all sensors are assumed coplanar and a constant cross-sectional part is placed in the measurement area, so that its cross-section is orthogonal to the linear axis. This can be achieved by a linear axis in still stand or a surrogate setup, which has a sufficiently known spatial relation to the linear axis. For 2D registration of the datasets and the nominal cross-section of the part, rigid transformations (x/y-translation ν_x, ν_y and z-rotation α) are estimated, e.g. by the ICP algorithm [100]. In case of sufficiently overlapping datasets, datasets can alternatively be registered to each other without information about the parts nominal cross-section [42]. With the briefly discussed proprietary sensor calibration method (section 3.2.1), this step is rendered redundant.

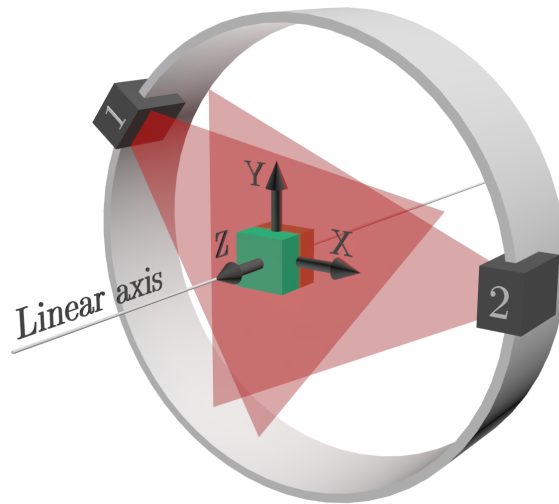


Figure 3.17: 3D sketch of a radial arrangement of two triangulation sensors with additional linear axis together with a constant cross-sectional part at the centre of the MCS.

The centre of the part thereby defines the centre of the MCS (figure 3.17) with the Z-axis orthogonal to its cross-section (along the linear axis). The Y-axis can be appropriately chosen.

The coplanarity assumption is feasible during this first step because the parameters that were forced to zero by this assumption (z-translation, x/y-rotation) have little influence on the 2D registration. E.g., assume that a cuboid with side lengths of 10 x 10 x 10 mm at the centre of an 800 mm diameter measurement field is used. Then, the y-translation error in the registration introduced by a sensor, violating the assumption by 0.1 deg rotational misalignment around the X-axis, is below 0.7 μm . Analogue errors result from rotational misalignment around the Y-axis. A violation by a z-translation has no influence on the 2D registration due to the constant cross-section of the cuboid.

CHAPTER 3. PROTOTYPE COORDINATE MEASURING SYSTEM DESCRIPTION

With the estimated parameters, a point \mathbf{p} from the sensor 2D laser plane coordinate system is then transformed to a point \mathbf{l} in the common 2D coordinate system by

$$\mathbf{l} = \begin{bmatrix} l_x \\ l_y \end{bmatrix} = \mathbf{t}_{xy} + \mathbf{R}_z(\hat{\alpha}) \cdot \mathbf{p}, \quad (3.10)$$

where $\mathbf{t}_{xy} = [\hat{\nu}_x \ \hat{\nu}_y]^\top$ is the translation vector and $\mathbf{R}_z(\hat{\alpha})$ the 2D rotation matrix with estimated angle $\hat{\alpha}$.

Alignment estimation To estimate the parameters of the sensor alignment, i.e. x/y-rotations γ , β and z-translation ν_z , the use of a right circular conical artefact with large aperture angle is proposed. For a high sensitivity to misalignments a large aperture angle is necessary (figure 3.16), e.g. a measured radius changes by $\tan(\theta) \cdot z$ where z is a z-offset. The artefact is placed n times $cp \in \{1, 2, \dots, n-1, n\}$, where n is at least three. Thereby the cone apex is at different positions \mathbf{t}^{cp} in the MCS and the direction of the cone axis for each placement is denoted as \mathbf{a}^{cp} (unit vector towards the inside of the cone, orthogonal to its base, figure 3.18). For each placement, all laser planes must intersect the lateral surface of the cone. Additionally, the positions, projected on the xy-plane, must not be collinear to achieve a robust parameter estimation. A schematic example for three placements with constant \mathbf{a}^{cp} for all positions is shown in figure 3.19.

The positions \mathbf{t}^{cp} and orientations \mathbf{a}^{cp} must be known relative to each other to estimate the sensor alignment parameters in a relative way. However, the spatial relation to the linear axis must be taken into account to avoid distortions due to rotational misalignment (figure 3.16). For this, the absolute x/y-orientations in the MCS have to be sufficiently known. Furthermore, the absolute x/y-positions in the MCS are necessary if manual adjustment of the sensors is the aim. This is required to enable evaluation of the alignment parameters at the sensor positions. Knowledge of the absolute positions along the Z-axis is not necessary since a shift along this axis does not affect the relative deviation between sensors nor the orientation w.r.t. the linear axis. Effects of inevitable positioning inaccuracies are discussed in section 3.2.4.

The further steps of the process are equivalent for all involved sensors and are described here for a single one. For each placement cp , a measurement is acquired. The resulting dataset consists of N^{cp} points in the common 2D coordinate system: $\mathbf{l}_i^{cp}, i = 1 \dots N^{cp}$.

The recorded 2D points are then converted into points in the 3D MCS by adding a third coordinate with value equal to 0 as

3.2. MEASUREMENT PROCESS AND DATAFLOW

$$\mathbf{k}_i^{cp} = \begin{bmatrix} \mathbf{l}_i^{cp} \\ 0 \end{bmatrix}. \quad (3.11)$$

Thus rigidly transforming the 2D points to 3D space onto the xy-plane. This constitutes the initial state ($\hat{\gamma} = \hat{\beta} = \hat{\nu}_z = 0$) for the parameter estimation.

Since the measurement points are on the intersection between the laser plane and cone artefact, the parameter estimation process can be thought of as transforming the laser plane, so that these points fit best to the cone surface at the different placements (figure 3.19). Thereby all points \mathbf{k}_i^{cp} are transformed by the same γ , β and ν_z as

$$\mathbf{j}_i^{cp}(\beta, \gamma, \nu_z) = \begin{bmatrix} 0 \\ 0 \\ \nu_z \end{bmatrix} + \mathbf{R}_{yx}(\beta, \gamma) \cdot \mathbf{k}_i^{cp}, \quad (3.12)$$

where $\mathbf{R}_{yx}(\beta, \gamma) = \mathbf{R}_y(\beta) \cdot \mathbf{R}_x(\gamma)$ denotes the combined 3D rotation matrix around the X- and Y-axis by γ and β , respectively. $\mathbf{j}_i^{cp}(\beta, \gamma, \nu_z)$ is a transformed point, i.e. rotated by $\mathbf{R}_{yx}(\beta, \gamma)$ and shifted by ν_z along the Z-axis. To minimise the distance between points \mathbf{j}_i^{cp} and the nominal lateral cone surface, the distance between a single point and the cone surface must be quantified. For that purpose, the functional

$$f_i^{cp}(\beta, \gamma, \nu_z) = (\mathbf{j}_i^{cp}(\beta, \gamma, \nu_z) - \mathbf{t}^{cp}) \cdot \mathbf{a}^{cp} - |\mathbf{j}_i^{cp}(\beta, \gamma, \nu_z) - \mathbf{t}^{cp}| \cdot \cos(\theta) \quad (3.13)$$

is proposed, where $|\mathbf{x}|$ describes the magnitude of a vector \mathbf{x} and θ is the half aperture of the cone (figure 3.18). By subtraction of \mathbf{t}^{cp} , the dependence on the cone position is removed and the distance evaluation simplifies. Essentially, points \mathbf{j}_i^{cp} are shifted so that the cone apex is at the origin. From figure 3.18, it can be seen that the functional represents the difference between two projections: the projection of a shifted point \mathbf{j}_i^{cp} onto the cone axis \mathbf{a}^{cp} and a projection to a vector at angle θ . If \mathbf{j}_i^{cp} lies outside of the cone, this difference will be negative, zero on the cone surface and positive inside the cone.

The functional shown in equation 3.13 was chosen due to its simple and fast numerical evaluation. Alternative measures for the distance between point and cone surface, e.g. the Euclidean distance, were evaluated and found to have similar performance in terms of convergence and accuracy of the results.

CHAPTER 3. PROTOTYPE COORDINATE MEASURING SYSTEM DESCRIPTION

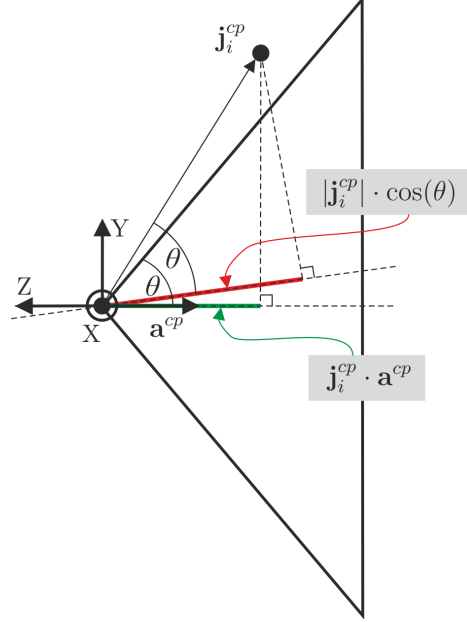


Figure 3.18: Visualisation of the proposed distance measure functional for the case $t^{cp} = 0$ (equation 3.13).

By minimising the sum of the square of equation 3.13 for all recorded points N^{cp} for all n placements, estimates for γ , β and ν_z are obtained by

$$(\hat{\beta}, \hat{\gamma}, \hat{\nu}_z) = \arg \min_{\beta, \gamma, \nu_z} \sum_{cp=1}^n \sum_{i=1}^{N^{cp}} [f_i^{cp}(\beta, \gamma, \nu_z)]^2. \quad (3.14)$$

The estimates can be used to minimise misalignments with a lower bound given by the estimation accuracy of the method, the positioning accuracy and the accuracy of the manual adjustment procedure.

Since the estimated parameters are related to the MCS that was defined by the preliminary registration step (section 3.2.4), $\hat{\nu}_z$ is the z -offset at the MCS centre. For practical adjustment, this offset has to be known at the sensor position. By transforming the origin of the laser plane coordinate system using the parameters obtained from the 2D registration, the z -offset of the sensor can be evaluated. Analogously, depending on the fixture of the sensors, an appropriate transformation of the estimated x/y -rotations can be necessary to guide the adjustment.

Alternatively, points from the common 2D coordinate system can be registered by 3D transformation with the estimated parameters by

3.2. MEASUREMENT PROCESS AND DATAFLOW

$$\mathbf{r} = \mathbf{R}_{yx}(\hat{\beta}, \hat{\gamma}) \cdot \begin{bmatrix} l_x \\ l_y \\ 0 \end{bmatrix} + \begin{bmatrix} 0 \\ 0 \\ \hat{\nu}_z \end{bmatrix}. \quad (3.15)$$

Obviously, this approach does not result in section-wise datasets. However, since the datasets are transformed for each cross-section separately, distortions originating from rotational misalignment (figure 3.16, right) are corrected by this approach.

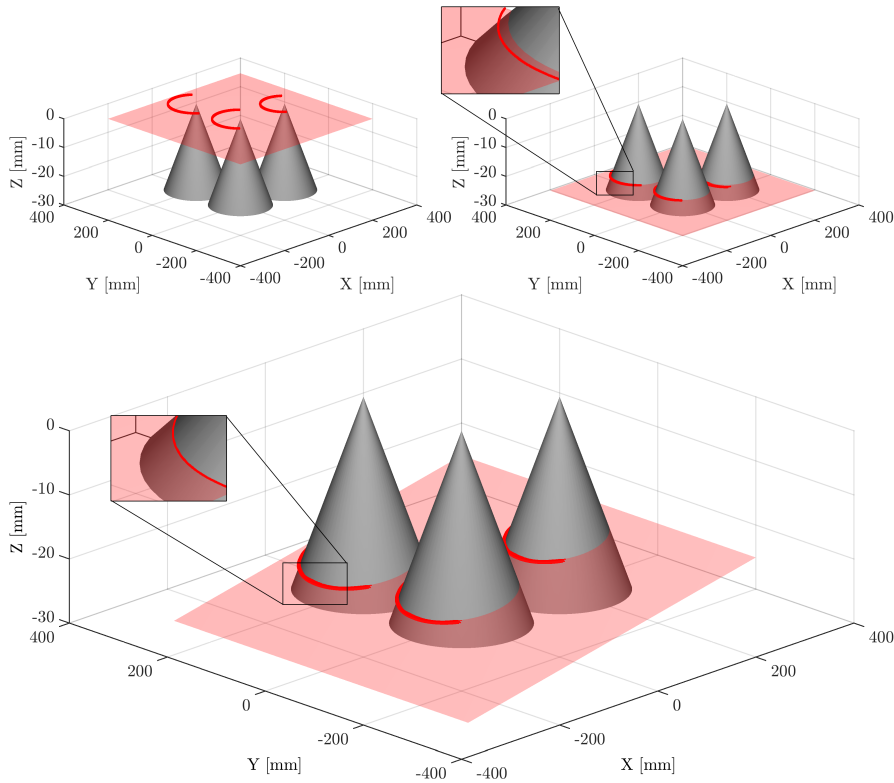


Figure 3.19: Simulated plane estimation for one misaligned sensor ($\gamma = 0 \text{ deg}$, $\beta = 1 \text{ deg}$, $\nu_z = -25 \text{ mm}$), acquired datasets as curves (red) for the three positions of the artefact. The Z-axis is magnified for clarity. Top: initial state ($\hat{\gamma} = \hat{\beta} = \hat{\nu}_z = 0$). Middle: result with estimated ν_z only. Bottom: result with estimated γ , β and ν_z .

Simulation and sensitivity analysis

The presented procedure and a corresponding simulation are implemented and verified using MATLAB 2014a [132]. Simulations were conducted to test the behaviour under practically present measurement noise and artefact positioning inaccuracies. For numerical evaluation of the optimisation problem (equation 3.14), the MATLAB `fsolve` function with the Levenberg-Marquardt optimisation algorithm was used. For eight involved sensors, three artefact positions and $N^{cp} \approx 500$ points per sensor and position, the process takes approx. 6 seconds, computed on a single core of a state-of-the-art commercial laptop³.

The three simulated artefact positions are shown in figure 3.19, with constant orientation for all positions $\mathbf{a}^{cp} = [0, 0, -1]^T$. The measurement area is not explicitly treated in the simulation but has to have at least 600 mm diameter to record datasets for all cone positions. Measurement noise was modelled as a 2D normal distribution in the laser plane coordinate system with $\Sigma(\mathbf{l}) = 0.15^2 \cdot \mathbf{I}^{2 \times 2}$ mm, as estimated from measurements on the physical artefact. For rotational (\mathbf{a}^{cp} rotated around X- and Y-axis, $\gamma^{a^{cp}}$ and $\beta^{a^{cp}}$, respectively) and translational (along X-, Y- and Z-axis, \mathbf{t}^{cp}) inaccuracies of the placement, normal distributions were used with $\text{Var}(\gamma^{a^{cp}}) = \text{Var}(\beta^{a^{cp}}) = 0.015^2$ deg and $\Sigma(\mathbf{t}^{cp}) = 0.025^2 \cdot \mathbf{I}^{3 \times 3}$ mm, respectively. Those values are chosen to represent usual manufacturing and positioning inaccuracies. Artefact imperfections were not explicitly considered, however, positioning inaccuracies capture some of them (base flatness, cone axis to base perpendicularity).

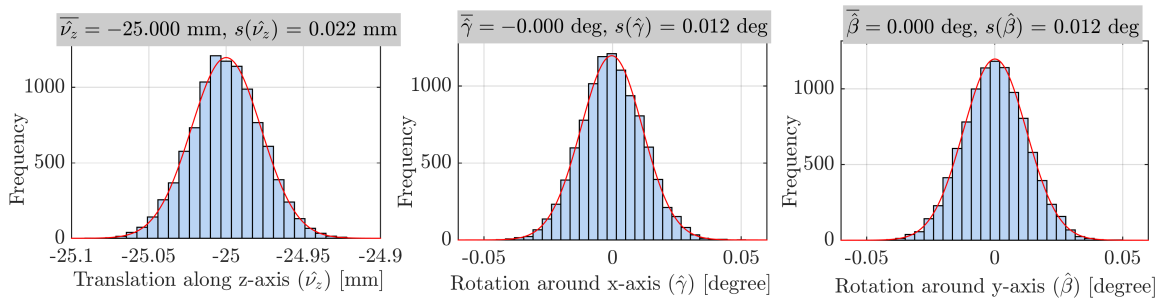


Figure 3.20: Simulation results with all parameters as random variables, evaluated by 10 000 runs as histograms (blue bars) and fitted normal distribution (red solid line) with nominally -25 mm z-translation and no x/y-rotations.

To estimate the influence of the described noise and inaccuracy factors, the simulation was run 10 000 times, with one or more inputs as random variables using the discussed probability distributions. Table 3.2 shows the results if no rotational misalignment exists ($\gamma = \beta = 0$ deg, also figure 3.20), with misalignment around one axis ($\gamma = 1$ deg) and both

³Intel Core i7-4700MQ @2.4 GHz, 8 GB RAM, Windows 7

3.2. MEASUREMENT PROCESS AND DATAFLOW

Table 3.2: Simulation results as evaluated by 10 000 runs. Nominal alignment parameters (γ, β, ν_z) , random variables as inputs and resulting sample standard deviations of estimated alignment parameters.

γ [deg]	β [deg]	ν_z [mm]	Randomised inputs [mm/deg]	$s(\hat{\gamma})$ [deg]	$s(\hat{\beta})$ [deg]	$s(\hat{\nu}_z)$ [mm]
0	0	-25	$\Sigma(\mathbf{1}) = 0.15^2 \cdot \mathbf{I}^{2 \times 2}$	0.001	0.001	0.002
1	0	-25	$\Sigma(\mathbf{1}) = 0.15^2 \cdot \mathbf{I}^{2 \times 2}$	0.001	0.001	0.002
1	1	-25	$\Sigma(\mathbf{1}) = 0.15^2 \cdot \mathbf{I}^{2 \times 2}$	0.001	0.001	0.002
0	0	-25	$\text{Var}(\gamma^{\text{a}^{cp}}) = \text{Var}(\beta^{\text{a}^{cp}}) = 0.015^2$	0.008	0.008	0.012
1	0	-25	$\text{Var}(\gamma^{\text{a}^{cp}}) = \text{Var}(\beta^{\text{a}^{cp}}) = 0.015^2$	0.008	0.008	0.012
1	1	-25	$\text{Var}(\gamma^{\text{a}^{cp}}) = \text{Var}(\beta^{\text{a}^{cp}}) = 0.015^2$	0.008	0.008	0.013
0	0	-25	$\Sigma(\mathbf{t}^{cp}) = 0.025^2 \cdot \mathbf{I}^{3 \times 3}$	0.009	0.009	0.018
1	0	-25	$\Sigma(\mathbf{t}^{cp}) = 0.025^2 \cdot \mathbf{I}^{3 \times 3}$	0.008	0.009	0.019
1	1	-25	$\Sigma(\mathbf{t}^{cp}) = 0.025^2 \cdot \mathbf{I}^{3 \times 3}$	0.008	0.009	0.019
0	0	-25	All above (figure 3.20)	0.012	0.012	0.022
1	0	-25	All above	0.012	0.012	0.023
1	1	-25	All above	0.012	0.012	0.024

axes ($\gamma = \beta = 1$ deg). For the case with all influences as random variables, in the worst case ($\gamma = \beta = 1$ deg) a sample standard deviation of 0.012 deg for $\hat{\gamma}$ and $\hat{\beta}$ and 0.024 mm sample standard deviation for $\hat{\nu}_z$ were obtained. The sample mean deviated from the nominal value in all cases less than 10^{-16} mm. Considering the size of the measurement area, the results indicate that the proposed method is sufficiently robust against expected measurement noise and inaccuracies in artefact positioning for the purpose of sensor adjustment.

Additionally, different cone aperture angles and nominal plane distances (i.e. distance of the laser plane from the cone apex along \mathbf{a}^{cp}) were simulated. For the cone half aperture angle, results indicate that the half aperture shall be as high as possible for estimating γ , whereas for estimating ν_z this does not apply (figure 3.21). For very large angles, variations in ν_z are increasing. It can be shown that this effect originates from the rotational inaccuracies of the cone ($\text{Var}(\gamma^{\text{a}^{cp}})$ and $\text{Var}(\beta^{\text{a}^{cp}})$). Their influence is amplified by very large aperture angles and with the assumed inaccuracies, the optimum half aperture angle is approx. 70 deg. The plane distance ν_z also affects the variation of results as shown in figure 3.22. This distance can be adjusted by appropriate placement and determines the

CHAPTER 3. PROTOTYPE COORDINATE MEASURING SYSTEM DESCRIPTION

minimum height of the conical artefact. The effect is lower though and caused by the decreasing number of recorded points if the plane is shifted towards the cone apex.

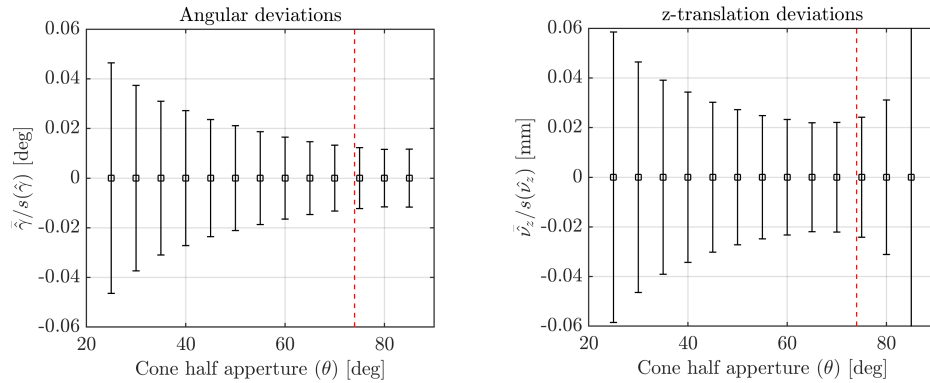


Figure 3.21: Simulation results (10 000 runs, all parameters as random variables). Half aperture angle θ vs. sample mean and sample standard deviation as error bars for angular deviations (left) and z-translation deviations (right). Dashed red line indicates the value from experiments.

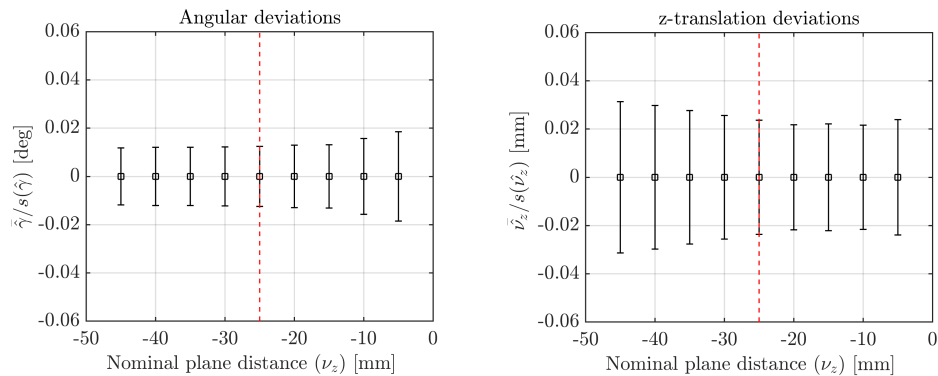


Figure 3.22: Simulation results (10 000 runs, all parameters as random variables). Nominal z-translation ν_z vs. sample mean and sample standard deviation as error bars for angular deviations (left) and z-translation deviations (right). Dashed red line indicates the value from experiments.

Experimental verification

The proposed conical artefact was made of aluminium and white coated to obtain an optically cooperative surface (figure 3.23, right). The nominal half aperture θ is 74 deg. This value was chosen to be equivalent to the maximum steepness along the axis of typical workpieces to be measured. Artefact conicity, perpendicularity of the cone axis to the base

3.2. MEASUREMENT PROCESS AND DATAFLOW

Table 3.3: Estimated parameters for eight triangulation sensors with sample standard deviations. Largest absolute values highlighted in bold.

#	$\hat{\gamma}$ [deg]	$\hat{\beta}$ [deg]	$\hat{\nu}_z$ [mm]
1	-0.030 ± 0.012	-0.053 ± 0.012	0.041 ± 0.030
2	0.028 ± 0.012	-0.026 ± 0.012	-0.472 ± 0.030
3	0.002 ± 0.012	0.031 ± 0.012	-0.179 ± 0.030
4	-0.065 ± 0.012	-0.091 ± 0.012	0.065 ± 0.030
5	-0.020 ± 0.012	-0.048 ± 0.012	0.291 ± 0.030
6	0.112 ± 0.012	-0.019 ± 0.012	-0.076 ± 0.030
7	-0.014 ± 0.012	0.068 ± 0.012	0.090 ± 0.030
8	-0.084 ± 0.012	0.092 ± 0.012	0.238 ± 0.030

and flatness of the base were identified as relevant parameters for the successful implementation of the method and calibrated using a tactile CMS (MPE of length measurement: $2.7 + L(\text{mm})/300 \mu\text{m}$). The results for cone perpendicularity and flatness are less than $10 \mu\text{m}$, while conicity is below $20 \mu\text{m}$.

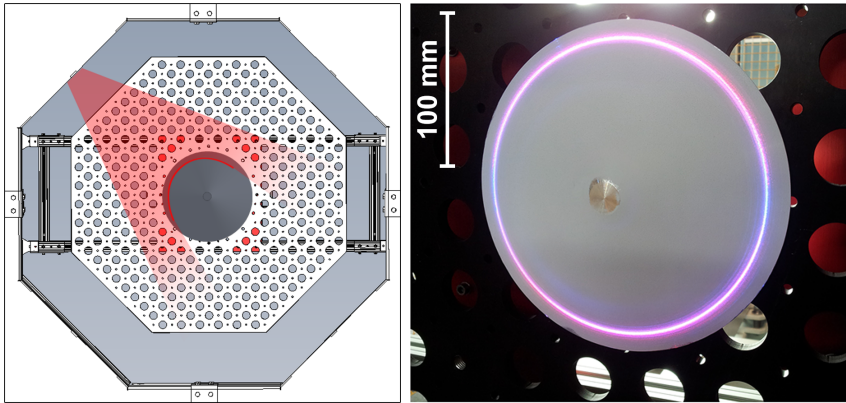


Figure 3.23: Left: drawing of the prototype CMS with perforated plate and fixed artefact, one sensor enabled. Right: close-up of the artefact with laser light reflection, all sensors enabled.

The positioning of the artefact was done by fixing the base of the cone to a perforated plate mounted inside the system (figure 3.23, right). The same positions and orientations as in the simulation were chosen (figure 3.19). The flatness of the perforated plate used as surrogate setup is in the order of $10 \mu\text{m}$. Perpendicularity of the plate to the linear axis was previously ensured.

CHAPTER 3. PROTOTYPE COORDINATE MEASURING SYSTEM DESCRIPTION

By conducting the described method four times for different artefact positioning, i.e. as shown in figure 3.19 and rotated around the Z-axis by 90, 180 and 270 deg, sample standard deviations of the estimated parameters were calculated. The mean sampled standard deviation over all eight sensors for z-translation is 0.03 mm and 0.012 deg for the x/y-rotations. These results correspond well with the previously shown sensitivity simulation results.

The estimates $\hat{\gamma}$, $\hat{\beta}$ and \hat{v}_z , obtained by the proposed method, are given in table 3.3, together with the experimentally determined sample standard deviations. Performing the procedure for three positions of the artefact and eight sensors takes approx. 2 min using an appropriate triggering of the sensors and laser diodes.

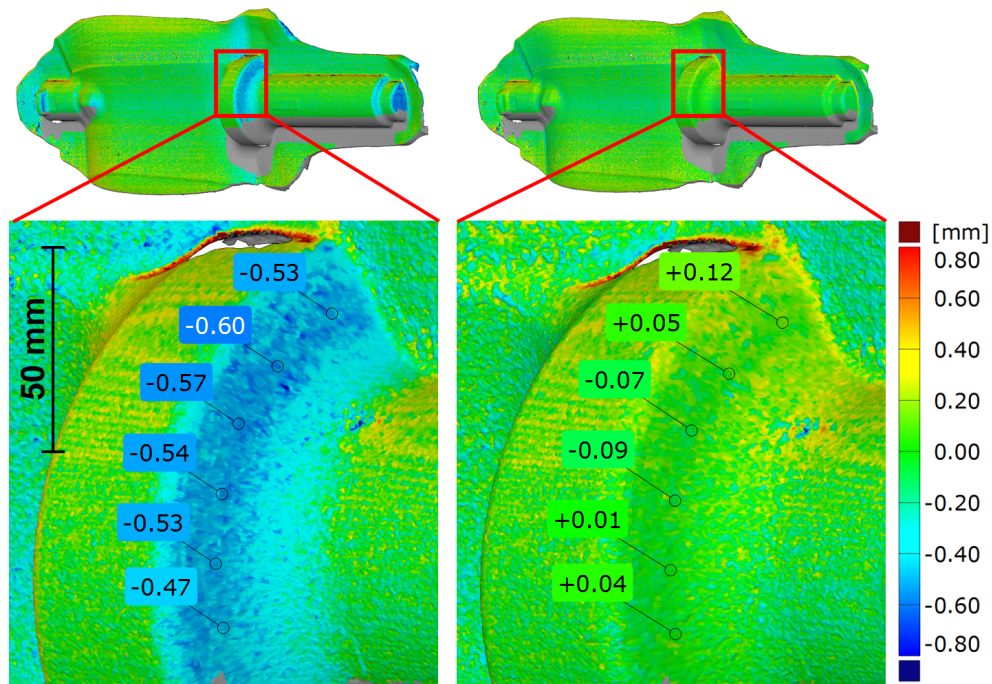


Figure 3.24: Deviation map of overlapping datasets from sensor #1 and #2 on a turbine blade foot. Left: before registration, manually adjusted. Right: after registration.

To demonstrate the accuracy improvement by the proposed method using 3D registration, several experiments were performed on parts featuring different geometry. In case of limited slope, the improvement is intrinsically small, while on steeper surfaces the advantage is evident: e.g. for the steepest details on turbine blades typical deviations between overlapping measurements of two adjacent sensors (#1 and #2) were reduced from 0.5 mm to 0.1 mm (figure 3.24). It should be noted, that the remaining 0.1 mm are within the measurement noise for single points and the systematic deviation could be largely removed.

Data fusion and meshing

If datasets are registered appropriately, typically the next step is fusing data into a single dataset [99] followed by – for this application – a surface reconstruction step. Note that the proposed section-wise surface reconstruction (section 3.2.3) is not applicable with the proposed adjustment method since sensor-wise datasets P^s do not represent regions of the same section nor are they necessarily parallel to each other. Thus, it was decided to utilise available commercial state-of-the-art metrology software, i.e. GOM Inspect V8 [135] for the data fusion and meshing steps.

The data fusion step is simplified w.r.t. the constant cross-sectional case: datasets from all sensors are simply merged into a single dataset as $Q = \check{P}$, since there is no sophisticated data fusion feature available in the software. However, a data reduction procedure is performed implicitly in the surface reconstruction step.

As surface reconstruction procedure, the GOM Inspect V8 [135] software algorithm was employed. Details about the algorithm are not available. Although, it can be stated that the algorithm works on unstructured 3D pointsets in contrast to the contour-wise approach (section 3.2.3). The algorithm does not necessarily use all points to approximate the surface, depending on the reconstruction parameters, i.e. the amount of vertices in the triangulated surface is possibly lower than the number of measured points.

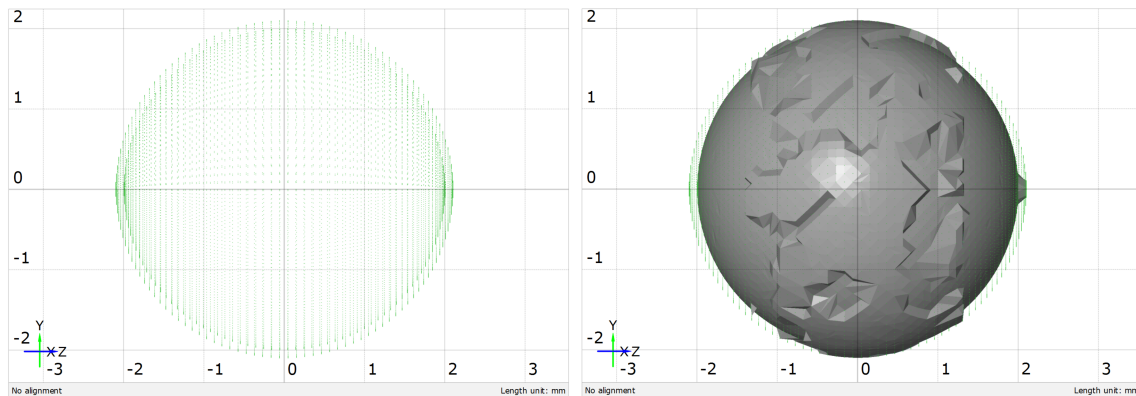


Figure 3.25: Surface reconstruction experiment in GOM Inspect V8 [135]. Left: 3D pointset of two spheres with equal centre and diameters $d_1 = 4$ mm, $d_2 = 4.2$ mm. Right: surface reconstruction, consisting of points from both spheres (Parameters: min. distance of points: 0.1 mm, max. noise: 0.5 mm, max. length of edges: 2.0 mm).

Experiments demonstrated that the available method does not include any averaging in case of deviations between the involved datasets. This was demonstrated by the author on 3D pointsets of two spheres with equal centre and differing diameter, e.g. 4 mm and

4.2 mm (figure 3.25, left). If all points are treated as one 3D pointset, the resulting surface consists of points of the smaller and larger sphere (figure 3.25, right). Thus, no averaging for competitive datasets is conducted.

3.3 Applicability of data fusion concepts

The author wants to highlight that the methodology proposed for non-constant cross-sectional workpieces, i.e. 3D data registration, is also applicable for constant cross-sectional workpieces if non-realtime meshing is acceptable. If realtime capability is a necessity, optimised physical adjustment, e.g. by the method proposed in this chapter, and section-wise meshing is recommended for constant cross-sectional workpieces.

On the other hand, for non-constant cross-sectional workpieces, experiments demonstrated that an improved physical adjustment or 3D data registration is necessary. If realtime capability is necessary, the section-wise meshing approach is to be used and sufficiently optimised physical adjustment is required.

The insensitivity to sensor misalignment for constant cross-sectional workpieces originates from the one degree of invariance along the Z-axis (section 3.2.3). Although such an invariance exists on the nominal geometry, it is not necessarily encountered in reality. E.g. let two local surface defects be mutually shifted by 0.5 mm along the Z-axis. With manual alignment, sensor measurement areas may have a distance of 0.5 mm along the Z-axis. Assume one sensor captures one of the defects and the other sensor records the other one. Thus, the result can be a cross-section, containing both defects at the supposed same z-position. In contrast, assume the two defects are at the same z-position and the sensors measurement fields are again 0.5 mm apart along the Z-axis. Consequently, the cross-section with both defects is never apparent in the measurement data. Depending on the measurand, this effect can cause type I errors (discarding conforming parts) or type II errors (accepting nonconforming parts) in conformity testing [11] and ultimately leads to economical loss. Thus, for both, constant and non-constant cross-sectional workpieces, adequately accurate aligned sensors or application of 3D registration is recommended.

3.4 Conclusion

In this chapter, an overview of the CMS was given and the internal measurement data processing was discussed. A clear distinction between constant cross-sectional workpieces and non-constant cross-sectional workpieces was made due to different requirements in terms of laser planes coplanarity and realtime capability.

For the case of constant cross-sectional workpieces, a 2D data fusion method based on the alpha shape was proposed. It has the same asymptotic time complexity as the readily implemented simple averaging procedure. The method was compared to the averaging procedure, yielding improved results in terms of double line handling and edge preservation on a typical dataset while having the same asymptotic time complexity. Additionally, the method allows quantifying the locally measurement point dispersion. This provides operators a quantitative assessment of deviations between sensors.

Moreover, a heuristic surface reconstruction method was proposed, based on earlier work in this field. The method from Chae & Lee [124] was combined with considerations about concave regions from Keppel [122]. The resulting algorithm has realtime capability due to its heuristic nature. By considering local curvature, concave regions are reconstructed better than with the original method – as evaluated by qualitative topology assessment.

A method to determine the relative sensor positions and orientations w.r.t. the linear motion system axis was presented. The method consists of a conical artefact, a surrogate setup and a computer algorithm that solves the inherent optimisation problem numerically. The obtained results can be used twofold: (i) to guide the physical sensor adjustment process and quantify the residual error due to misalignment or (ii) for registration of measurement points in a common coordinate system. The robustness of the method was demonstrated by simulations. Repeated experiments on the eight sensor CMS show good correspondence to simulation results. The influences originating from the artefact geometry on parameter estimation accuracy were also evaluated by simulations. Results indicate an optimal half aperture angle of approx. 70 deg and a low influence of the artefact positioning. Experimental results show a 5-times improvement for the steepest details on turbine blades by the presented method.

CHAPTER 3. PROTOTYPE COORDINATE MEASURING SYSTEM DESCRIPTION

Chapter 4

System characterisation

By use of the described hardware and software methods (chapter 3), different aspects of the CMS were characterised. All experiments were performed under shop floor conditions, as the intended use of the system is at the shop floor. The described experiments were executed at the forging plant of Pietro Rosa TBM s.r.l. [14], where the CMS was available in the framework of the Eurostars HOTGAUGE (E!6692) research project.

Dominant error sources were identified and quantified based on methods from the Guide to the expression of Uncertainty in Measurement (GUM) [136]. It shall be pointed out that it was not the aim to identify and quantify all possible input quantities nor to provide a sound uncertainty statement for a specific measurand on a specific workpiece. Procedures from the GUM were applied to quantify the most dominant influences on different system components.

Besides the characterisation of influences, additional tests of specific system characteristics were conducted: the effect of infrared radiation, originating from the workpiece at approx. 1000 °C, on the sensor was investigated; influence of the sampling density along the Z-axis – a parameter of the measurement strategy; and an analysis of effective resolution. Finally, with the discussed corrections applied, a bidirectional length test at elevated temperature is presented to demonstrate the achieved system performance.

4.1 Measurand definition

Since the CMS can be flexibly used for a variety of measurement tasks (e.g. [4, 10]), influences on single pointwise distance measurements between the sensor and workpiece

were analysed. Based on these results, influences on specific measurands can be obtained in a further step [42].

Note that there is no holistic mathematical model as prescribed by the GUM. Instead, distinct models for influences on specific components of the system were developed. This approach was chosen to assess effects on the different components of the system separately. The quantified influences are discussed and corrected, where necessary.

4.2 Identification of dominant error sources

During extensive discussions with experts in the context of the HOTGAUGE research project, several potentially relevant influence quantities were identified. Influences, classified as highly relevant, are underlined in figure 4.1, namely temperature, self-illumination, distribution of measurement points, and multisensor registration.

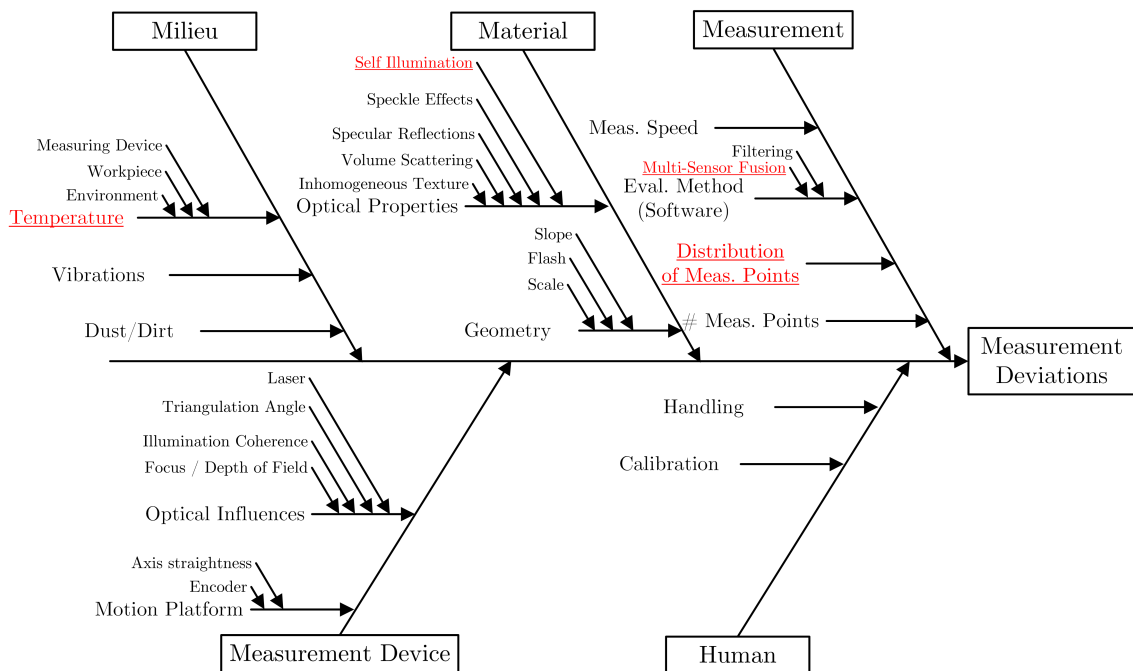


Figure 4.1: Ishikawa diagram of identified influence factors on the measurement result. Underlined factors are classified as highly relevant.

Clearly, other quantities influence the measurement results as well. However, recall that the aimed MPE of length measurement is 0.2 mm. Thus, effects in the order of 10^{-2} mm are considered as acceptable for the intended use of the system. By this consideration and

4.2. IDENTIFICATION OF DOMINANT ERROR SOURCES

available literature, some typical influences on optical triangulation measurement systems could be excluded in advance, as described in the following.

Schwenke et al. [54] and Chen et al. [137] state a relative resolution of 10^{-4} and an accuracy of 10^{-4} for light sectioning, respectively. For the CMS under consideration, with 800 mm diameter measurement area, this would result in maximally 80 μm . Vukasinovic et al. [138] studied the influence of surface topology on the accuracy of laser triangulation measurements. They report a maximal standard deviation of approx. 25 μm for distances between 70 mm to 130 mm and angles between surface and sensor of 0 deg to 75 deg. Unfortunately, only an analysis of variance (ANOVA) was reported, while lacking a reference quantity value and thus an uncertainty statement. Other authors [139, 140] report measurement uncertainties of 7 μm for diameters and 70 μm for cylindricity on a metallic cylinder with a custom 3D laser scanner (one laser for line generation and two cameras).

The surface dependence for laser triangulation sensors is often stressed in literature (e.g. [10, 54, 141]). At least partly diffuse reflectance of the surface is required, since light, reflected from the workpiece, must fall into the camera, independently of the surface orientation. Although, materials that reflect the majority of incident light by specular reflection show a higher influence of the topology to measurement uncertainty [141]. During experiments, the reflectance of gas turbine blades at elevated temperature was investigated and no notable specular reflections could be identified.

Speckle effects were also considered a priori. Such effects originate from coherent light in interaction with rough surfaces, i.e. peak to valley in the order of the laser wavelength or higher [86]. The coherent light, reflected on rough surfaces, causes self-interference, i.e. locally constructive or destructive interference, manifesting in intensity variations in the camera image. However, due to constant movement of the workpiece during the measurement process, it was assumed that the effect diminishes to a negligible level due to averaging of constructive and destructive interference during the camera exposure time. This assumption could be confirmed by qualitative assessment of the imaged laser line on multiple experiments.

Thus, a low influence of surface topology due to diffusely reflecting surfaces and averaging of destructive and constructive interference can be assumed. By above considerations, it was decided to concentrate on the identified influences, originating from the workpiece at elevated temperature and the use of multiple sensors.

All calculated numerical values shown in this chapter are rounded according to DIN 1333 [142]. However, for numerical calculations, the precision attained by the double-precision floating-point format [143] was exploited. The expectation of random variables, necessary

for calculation of sensitivity coefficients, is approximated by the sample mean throughout this chapter.

4.3 Multisensor data fusion

As discussed in section 3.2.3 and 3.2.4, the influence of sensor misalignment on measurement results strongly depends on workpiece geometry. Here, deviations originating from non-perfect sensor alignment and the residual error from non-perfect data registration are modelled for a typical turbine blade geometry.

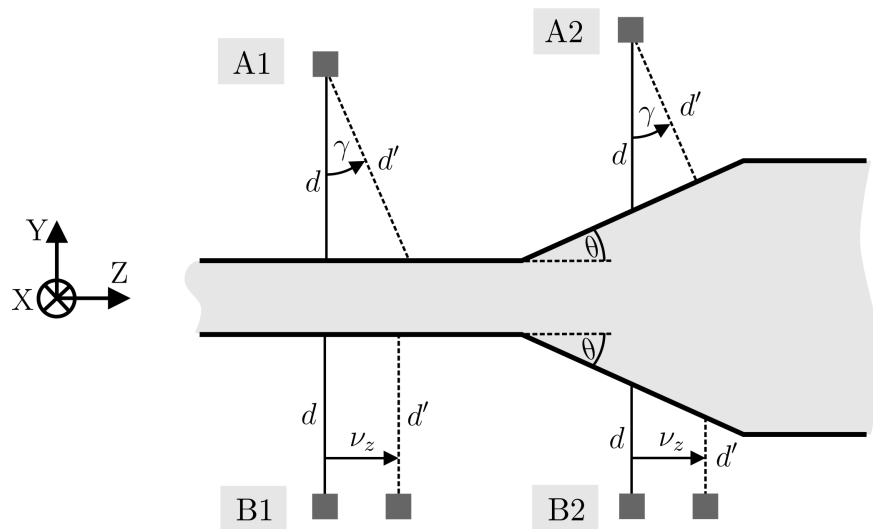


Figure 4.2: Different cases (A1, A2, B1, B2) of sensor misalignment, Top: angular misalignment γ around X-axis (A1 and A2). Bottom: shift ν_z along Z-axis (B1 and B2).

Different cases of misalignments are shown in figure 4.2. The effect on distance measurements is

$$\Delta d_{MultiSensor} = d' - d. \quad (4.1)$$

By geometrical considerations, explicit equations can be given as

$$\Delta d_{A1} = d (1/\cos \gamma - 1) \quad (4.2a)$$

$$\Delta d_{A2} = d (1/\cos \gamma - 1) - \operatorname{sgn}(\theta) \operatorname{sgn}(\gamma) \frac{d \sin (|\theta|) \tan (|\gamma|)}{\sin (90 - |\theta| - \operatorname{sgn}(\theta)|\gamma|)} \quad (4.2b)$$

$$\Delta d_{B1} = 0 \quad (4.2c)$$

$$\Delta d_{B2} = -\nu_z \tan \theta, \quad (4.2d)$$

where $\operatorname{sgn}()$ denotes the sign function. The dependence on the workpiece slope θ shows up in case A2 (equation 4.2b) and B2 (equation 4.2d). Clearly, A1 and B1 are special cases where $\theta = 0$. In case B1, no deviations are evident on the nominal geometry and such a misalignment is not necessarily identifiable from the measurement data (section 3.2.3). For the following analysis, angular and translational misalignment influence are merged into

$$\begin{aligned} \Delta d_{MultiSensor} &= d' - d = \Delta d_{A2} + \Delta d_{B2} \\ &= d (1/\cos \gamma - 1) - \operatorname{sgn}(\theta) \operatorname{sgn}(\gamma) \frac{d \sin (|\theta|) \tan (|\gamma|)}{\sin (90 - |\theta| - \operatorname{sgn}(\theta)|\gamma|)} - \nu_z \tan \theta. \end{aligned} \quad (4.3)$$

This influence is symmetric for possible combinations of θ and γ , i.e. the same value $\Delta d_{MultiSensor}$ results for $(\theta = x, \gamma = y, \nu_z = z)$ and $(\theta = -x, \gamma = -y, \nu_z = -z)$. This is also true for $(\theta = x, \gamma = -y, \nu_z = z)$ and $(\theta = -x, \gamma = y, \nu_z = z)$. Note that the worst case scenario requires $\operatorname{sgn}(\nu_z) = \operatorname{sgn}(\gamma) \neq \operatorname{sgn}(\theta)$, e.g. shift along the positive Z-axis, positive rotational deviation of the sensor but negative surface slope.

Values for γ and ν_z have been determined experimentally (section 3.2.4) and were verified by expert opinion from an experienced engineer of Zumbach AG [41]. Upper bound values were defined as $\gamma = \pm 0.15$ degree and $\nu_z = \pm 0.5$ mm. Due to lack of more information, a uniform distribution is assumed. By considering the symmetry of the influence, consideration of the *absolute* values was found to be sufficient for the aimed estimation of influences, i.e. $\gamma = U(0 \text{ deg}, 0.15 \text{ deg})$ and $\nu_z = U(0 \text{ mm}, 0.5 \text{ mm})$.

CHAPTER 4. SYSTEM CHARACTERISATION

Thus, standard uncertainties are

$$u(\gamma) = (0.075/\sqrt{3}) \text{ deg} \quad (4.4)$$

and

$$u(\nu_z) = (0.25/\sqrt{3}) \text{ mm}. \quad (4.5)$$

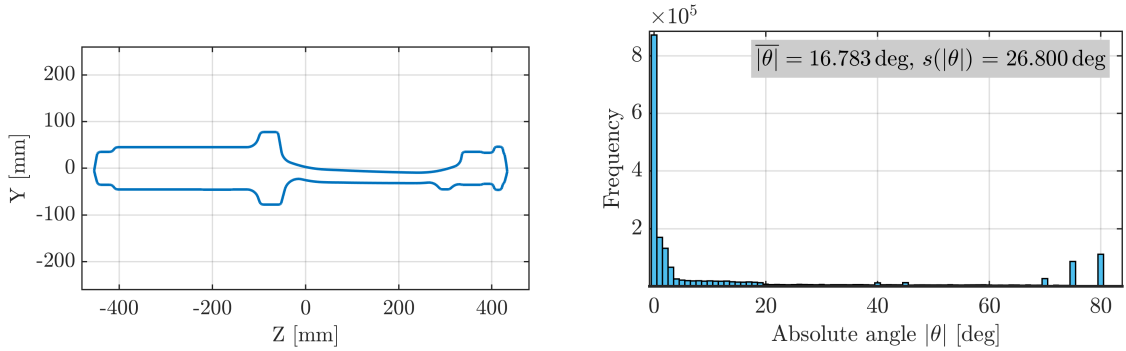


Figure 4.3: Left: section of a gas turbine blade in the YZ-plane. Right: histogram of absolute angle $|\theta|$, including sample mean and sample standard deviation.

The distribution of the angle θ is found by numerically evaluating derivatives of a section in the YZ-plane of a nominal gas turbine blade computer model (figure 4.3, left). For this evaluation, it is assumed that the workpiece is placed in the CMS, such that the Z-axis from design coordinate system and MCS correspond. Again due to symmetry, absolute values of the slope are considered (figure 4.3, right) and sample mean plus sample standard deviation are calculated, yielding $u(|\theta|) = s(|\theta|) = 27 \text{ deg}$ and an expected value of $E[|\theta|] = 16.8 \text{ deg}$. Note that the negative value $-E[|\theta|]$ is used to emulate the worst case, as described above. The corresponding sensitivity coefficients are found by partial derivation of equation 4.3 at the expected values as $c_\theta = -0.0132$, $c_\gamma = 2.1$ and $c_{\nu_z} = 0.30$. Thus, an expanded uncertainty for the uncorrected case can be given as

$$\begin{aligned} U(\Delta d_{MultiSensor}) &= k \sqrt{c_\gamma^2 u^2(\gamma) + c_{\nu_z}^2 u^2(\nu_z) + c_\theta^2 u^2(|\theta|)} \\ &\quad + \Delta d_{MultiSensor}(\gamma = 0.075 \text{ deg}, \nu_z = 0.25 \text{ mm}, \theta = -16.8 \text{ deg}) \quad (4.6) \\ &= 0.96 \text{ mm} \end{aligned}$$

for $k = 2$. This effect is clearly not negligible for the aimed use of the CMS. If the proposed multisensor registration method (section 3.2.4) is applied, the standard deviations of the absolute residuals of the method for γ (or equivalently β) and ν_z can be plugged into equation 4.6 as standard uncertainties, i.e. $u(\gamma_{Corrected}) = 0.007 \text{ deg}$ and $u(\nu_{z,Corrected}) = 0.018 \text{ mm}$.

Additionally, the term $\Delta d_{MultiSensor}(\dots)$ from equation 4.6 changes to $\Delta d_{MultiSensor}(\gamma = 0.00016 \text{ deg}, \nu_z = 0.024 \text{ mm}, \theta = -16.8 \text{ deg}) = 26.8 \mu\text{m}$. The former two parameters are obtained by $E[|N(0, u(\gamma_{Corrected})^2)|] = 0.00016 \text{ deg}$ and analogue for ν_z , where $N(\mu, \sigma^2)$ denotes the normal distribution with mean μ and variance σ^2 . Applying the procedure from above with these quantities leads to an expanded uncertainty of

$$U(\Delta d_{MultiSensor,Corrected}) = 0.113 \text{ mm} \quad (4.7)$$

for $k = 2$. The results demonstrate the effectiveness of the proposed registration method and its necessity for the intended use of the system.

4.4 Temperature

Temperature is one of the influence factors that attained major attention due to the expected high temperature gradient between a workpiece at elevated temperature and the CMS. Several analyses, regarding refractive index gradient, effects on sensor geometry, effects on the metrology frame geometry and the linear motion system were conducted. Additionally, the background noise on the camera image due to thermal radiation is evaluated.

To reach environmental conditions as close as possible to those active while measuring actual workpieces, a series of billets at elevated temperature with mass similar to typical turbine blades were individually loaded onto the CMS and moved back and forth as in normal operation for 5 hours. During this time, the average temperature of the billets was starting at approx. 850°C and decreasing to approx. 400°C before loading the next one. During this experiment, temperatures in and on the 2D scanner were measured by its internal thermocouple sensors (figure 4.4). The internal sensors are Pt100, class B sensors. Such sensors exhibit a MPE of $\pm(0.30 \text{ K} + 0.005|T(^{\circ}\text{C})|)$ [144, 145]. Based on the measured temperatures, the upper bound for expected temperature values for all sensors was set to 35°C . Thus, the MPE of the sensors is given by

$$MPE_{Pt100} = \pm(0.30 \text{ K} + 0.005|35^\circ\text{C}|) = \pm 0.475 \text{ K}. \quad (4.8)$$

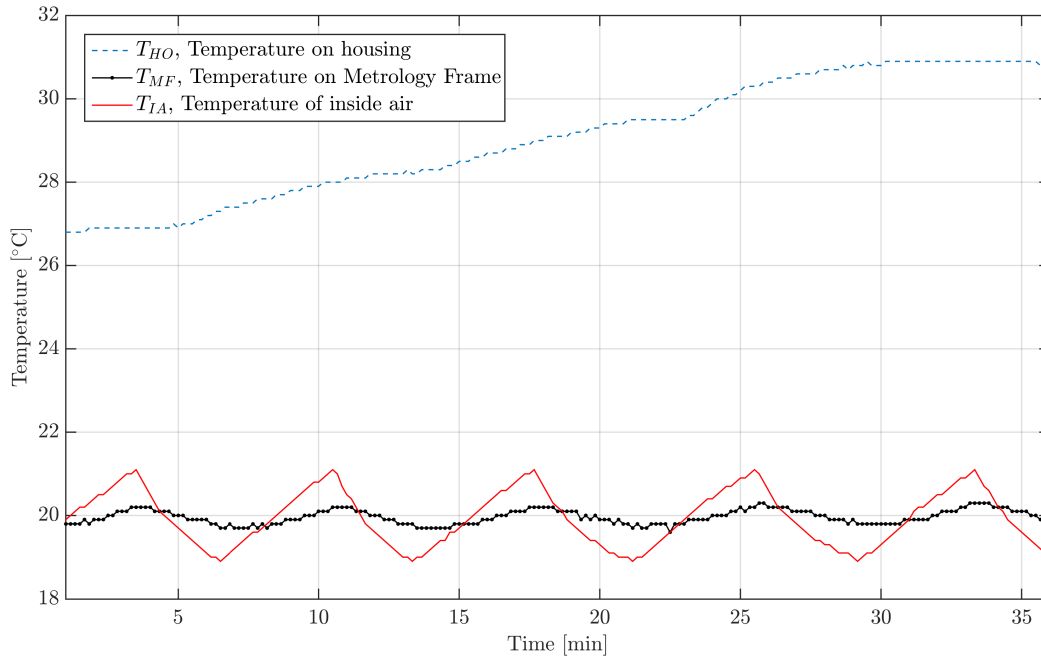


Figure 4.4: System temperatures as measured by internal thermocouple sensors during the first minutes of loading and measuring of workpieces at elevated temperature.

The sensor on the CMS housing shows a temperature gradient, eventually reaching a steady state after about 30 min. The inside air temperature T_{IA} is used for temperature control: if a value $\geq 21^\circ\text{C}$ is measured, the air chiller system is enabled and stays on until a value $\leq 19^\circ\text{C}$ is measured. Temperatures between 18.9°C and 21.1°C were measured though. It is evident by figure 4.4 that the temperature control by air cooling is sufficient to keep the system thermally stable. During all experiments with workpieces at elevated temperature, the auxiliary water cooling system was not required.

The temperature on the metrology frame, T_{MF} , follows the oscillation of the inside air temperature, T_{IA} , with a time lag of approx. 20 s (figure 4.4). The maximal deviation from 20°C of the metrology frame is $\pm 0.3\text{ K}$. In figure 4.5, histograms of the temperature on the metrology frame, T_{MF} , and inside air temperature, T_{IA} , are shown, generated from data of an approx. 2 hour long recording with 0.2 Hz framerate, resulting in 1426 measurement values per sensor. The histograms indicate the temperature distributions, which are approximated as uniform distributions for the following considerations.

Note that the state in which the CMS is calibrated (section 3.2.1) is not defined in terms of temperature. In the worst case, calibration is done at an extreme temperature, e.g. at an inside air temperature of $T_{IA,Cal} = 21.1^\circ\text{C}$ while measurements are conducted

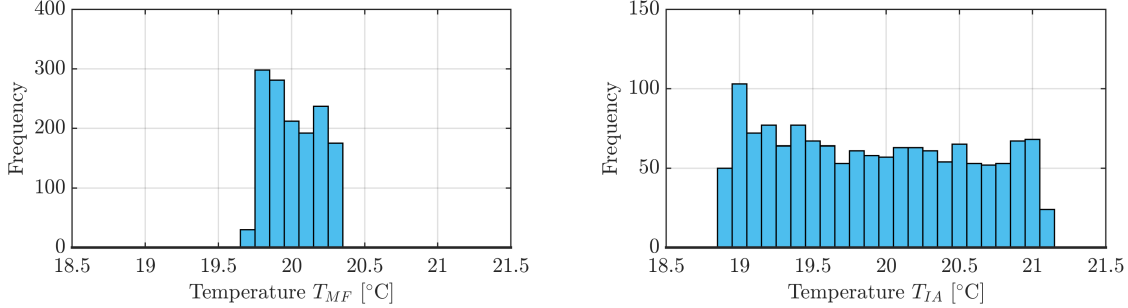


Figure 4.5: Left: histogram of metrology frame temperature measurements T_{MF} . Right: histogram of inside air measurements T_{IA} .

at $T_{IA} = 18.9^\circ\text{C}$. Thus, the maximal temperature deviation w.r.t. the calibrated state corresponds to two times the measured temperature range. This concept applies analogously for the MPE of the Pt100 sensors. By this consideration, define the standard uncertainty for operative and calibration state equal but separately as

$$u(T_{MF}) = u(T_{MF,Cal}) = \sqrt{\left(\frac{0.3^\circ\text{C}}{\sqrt{3}}\right)^2 + \left(\frac{0.475^\circ\text{C}}{\sqrt{3}}\right)^2} = 0.32 \text{ K} \quad (4.9)$$

and

$$u(T_{IA}) = u(T_{IA,Cal}) = \sqrt{\left(\frac{1.1^\circ\text{C}}{\sqrt{3}}\right)^2 + \left(\frac{0.475^\circ\text{C}}{\sqrt{3}}\right)^2} = 0.69 \text{ K}. \quad (4.10)$$

The expectation of the difference between the calibrated and the operative state, i.e. $E[T_{MF} - T_{MF,Cal}]$, is equal to zero. The value of this term is necessary for calculating sensitivity coefficients, which are possibly reduced to zero if the expected value is zero, and influences are eliminated. This was rated as too optimistic and the expected absolute difference, $E[|T_{MF} - T_{MF,Cal}|] = 0.37 \text{ K}$, was found to be more appropriate since the measurement system is typically calibrated at ambient temperature. The above results are utilised in the next sections to quantify error sources that are related to temperature influence.

4.4.1 Refractive index gradient

Due to temperature differences in the regions of sensors and workpiece, the refractive index n has a non-zero gradient along the path of the laser light. This influence on distance measurements was estimated by a hybrid approach of analytic modelling and numerical simulation, as discussed in the following.

CHAPTER 4. SYSTEM CHARACTERISATION

There exist multiple mathematical models to calculate an approximation of the refractive index of air, depending on temperature, relative humidity, pressure, CO₂ ratio and wavelength. The equation by Ciddor [146] and an updated version of Edlén's equation [147–149] are considered here, which are provided from the NIST engineering metrology toolbox [150].

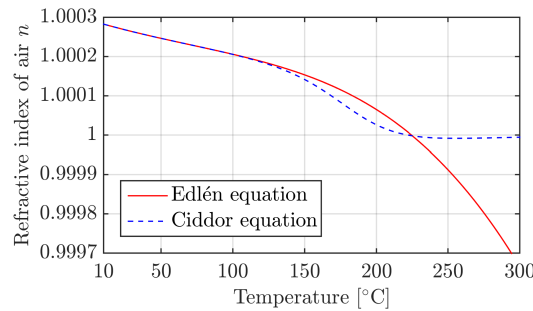


Figure 4.6: Temperature vs. refractive index for Ciddor and Edlén equations.

The temperature parameter for both models has an upper limit of 100 °C in the toolbox, as Ciddor suggested for his model [150]. By using a MATLAB implementation¹ without this restriction, but evaluating the same mathematical models, a strong divergence above 100 °C is evident (figure 4.6). Due to lack of an appropriate model, the air temperature, adjacent to the workpiece, is assumed to be between 20 °C and 100 °C. Formally,

$$T_{OA} = 60 \pm 40 \text{ } ^\circ\text{C}. \quad (4.11)$$

By the analogue argumentation as above, the standard uncertainties are defined as

$$u(T_{OA}) = u(T_{OA,Cal}) = \frac{40 \text{ K}}{\sqrt{3}} = 23 \text{ K}. \quad (4.12)$$

Differences of the refractive index between the two equations are of the order of magnitude of 10^{-9} for 20 °C and 10^{-6} for 100 °C. The equation by Ciddor is used in this work, since it should give better results under extreme conditions [150]. Moreover, the method is adopted as standard equation by the International Association of Geodesy (IAG). Pressure and CO₂ ratio parameters were set to $p = 101325 \text{ Pa}$ and $\text{CO}_2 = 450 \text{ } \mu\text{mol/mol}$, respectively. These are conventional values for standard atmospheric pressure and closed room CO₂ concentration [150].

¹<http://www.mathworks.com/matlabcentral/fileexchange/31240-air-refractive-index>, Author: John A. Smith, CIRES, University of Colorado at Boulder

A single limiting surface between volumes with different refractive indexes is assumed (figure 4.7), i.e. a refractive index transition at the 2D scanner housing only. This assumption does not hold in reality but is sufficient to estimate this effect, since it models a worst case scenario. Refraction is assumed to happen entirely at the limiting surface. That leads to higher deviations than a gradual refraction between 2D scanner housing and the workpiece (figure 4.7). Experiments by simple means demonstrated that the air nearby the 2D scanner housing is far below the assumed 100 °C, confirming a more gradual change of refractive index. Consequently, the real situation results in lower deviations, however due to the restricted assumption of 100 °C air temperature near to the workpiece, what is a potential underestimation, a worst case scenario is preferred.

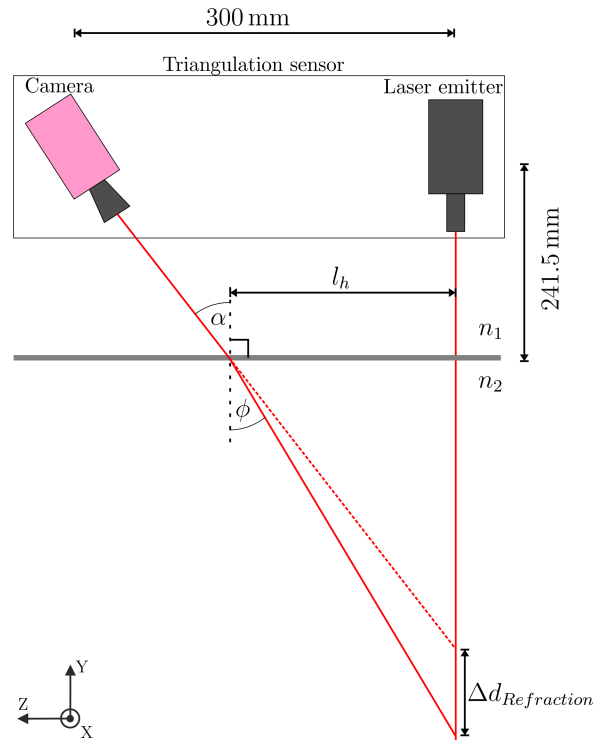


Figure 4.7: Sketch of the path difference $\Delta d_{Refraction}$ due to a change of the refractive index at the housing of the CMS (horizontal grey line). Inverse beam path, red line indicates the reflection observed by the camera including refraction. The red dashed line shows the reflection observed by the camera for the case $n_1 = n_2$.

By the model in figure 4.7 and some geometrical considerations, the difference of the vertical portion of the path in the n_2 volume can be described as

$$\Delta d_{Refraction} = \Delta l_v = l_h (\tan (90 \text{ deg} - \phi) - \tan (90 \text{ deg} - \alpha)), \quad (4.13)$$

CHAPTER 4. SYSTEM CHARACTERISATION

where ϕ denotes the angle after refraction (figure 4.7). Note that the vertical difference Δl_v is equivalent to the deviation of a single point distance measurement $\Delta d_{Refraction}$. The position of the limiting surface is determined by the systems nominal geometry, i.e. the nominal distance from the laser origin to the housing is 241.5 mm and as angle α between optical axis of camera and laser emitter, the nominal value of 30 deg is assumed. By some geometry, the horizontal portion of the path in the volume with refractive index n_2 can be found by

$$l_h = 300 \text{ mm} - \frac{241.5 \text{ mm}}{\tan(90 \text{ deg} - \alpha)}. \quad (4.14)$$

The angle after refraction, ϕ , is found by applying the law of refraction as

$$\phi = \arcsin\left(\frac{n_1}{n_2} \sin(\alpha)\right). \quad (4.15)$$

Further, the refractive indexes n_1 and n_2 are found by applying Ciddor's equation as described above. Exemplary results for the four installed laser wavelengths and different relative humidity are given in table 4.1. For the evaluated cases, results show that deviations are maximal for a relative humidity of 90% and a laser wavelength of $\lambda = 405 \text{ nm}$.

Table 4.1: Maximal deviations $\Delta d_{Refraction}$ for $T_{IA} = 20^\circ\text{C}$, $T_{OA} = 100^\circ\text{C}$, the four installed wavelengths and different relative humidity percentages (RH). The highest value is highlighted in bold font.

$\Delta d_{Refraction} [\mu\text{m}]$	RH = 30%	RH = 60%	RH = 90%
$\lambda = 405 \text{ nm}$	23.5	26.6	29.8
$\lambda = 450 \text{ nm}$	23.4	26.5	29.8
$\lambda = 640 \text{ nm}$	23.2	26.4	29.7
$\lambda = 670 \text{ nm}$	23.2	26.4	29.7

The combination of Ciddor's equation and the presented geometrical model is used to evaluate the sensitivity coefficients numerically. A relative humidity of 90% and a wavelength of 405 nm are utilised since those quantities indicate the highest deviations. Numerical partial derivation of equation 4.13 at 20°C and 60°C w.r.t. temperature yields $c_{T_{IA}} = 3.60 \cdot 10^{-4} \text{ mm/K}$ and $c_{T_{OA}} = 3.59 \cdot 10^{-4} \text{ mm/K}$. Note that the same sensitivity coefficient is utilised for the influence of temperature in calibrated and operational state, e.g. $T_{IA,Cal}$ and T_{IA} , since only their sign is different that vanishes by calculating the square.

The expanded uncertainty is thus evaluated as

$$\begin{aligned} U(\Delta d_{Refraction}) &= k \sqrt{c_{T_{IA}}^2 u^2(T_{IA}) + c_{T_{IA,Cal}}^2 u^2(T_{IA,Cal}) + c_{T_{OA}}^2 u^2(T_{OA}) + c_{T_{OA,Cal}}^2 u^2(T_{OA,Cal})} \\ &= 23 \mu\text{m} \end{aligned} \quad (4.16)$$

with $k = 2$. Naturally, the outside temperature is the dominant influence. By the inside temperature influence only, the expanded uncertainty is reduced to $0.7 \mu\text{m}$. For the intended use however, the entire influence is regarded as negligible. Due to the upper bound of 100°C for available models to evaluate the refractive index, this quantification is considered as a rough estimation.

4.4.2 Metrology frame expansion

Based on an earlier study [151] that includes a simulation of temperatures within the system, the metrology frame (section 3.1.1) expansion influence was estimated. Although the study suggests temperature deviations from 20°C by several degrees, aforementioned experiments demonstrate that the temperature of the metrology frame T_{MF} can be controlled by air cooling within a range of $\pm 0.4 \text{ K}$. With these experimentally determined values and the frame geometry and material, the influence on a single point distance measurement can be evaluated by

$$\Delta d_{FrameExpansion} = \alpha_{Al} L_0 (T_{MF} - T_{MF,Cal}) \quad (4.17)$$

and the expanded uncertainty is given by

$$U(\Delta d_{FrameExpansion}) = k \sqrt{c_{\alpha_{Al}}^2 u^2(\alpha_{Al}) + c_{T_{MF}}^2 u^2(T_{MF}) + c_{T_{MF,Cal}}^2 u^2(T_{MF,Cal})}. \quad (4.18)$$

Again, the same sensitivity coefficient is utilised for the influence of temperature in calibrated and operational state, justified by the same argument as in section 4.4.1. The Coefficient of Thermal Expansion (CTE) for aluminium is approximated by a value from literature [152] as $\alpha_{Al} = 24 \cdot 10^{-6} \text{ K}^{-1}$. For its uncertainty, following [153], 10% is assumed. The standard uncertainty of α_{Al} is thus given by $u(\alpha_{Al}) = 2.4 \cdot 10^{-6} \text{ K}^{-1} / \sqrt{3}$.

The sensitivity coefficients are found by derivation of equation 4.17 as

$$c_{\alpha_{Al}} = L_0(T_{MF} - T_{MF,Cal}) \quad (4.19)$$

and

$$c_{T_{MF}} = \alpha_{Al}L_0. \quad (4.20)$$

For the expectation of term $T_{MF} - T_{MF,Cal}$, the expected absolute value of 0.37 K is used, as argued in section 4.4. For the length L_0 , the largest nominal distance between a sensor and the mounting of the metrology frame of 850 mm is used (section 3.1.1), calculated by nominal geometry information. With those quantities, equation 4.18 evaluates to

$$U(\Delta d_{FrameExpansion}) = 18.7 \mu\text{m} \quad (4.21)$$

with $k = 2$. This result indicates that the metrology frame expansion has negligible influence for the intended use of the system.

4.4.3 Influence on sensors

To characterise the change of triangulation sensor geometry due to temperature variations, the work from Clarke et al. [154] is used as basis. The temperature on the metrology frame, T_{MF} is utilised as approximation of the temperature on the sensors cameras, since they are directly attached to the metrology frame.

Sensor expansion

Following [154], the thermal expansion of the photosensitive chip can be modelled as

$$\Delta p = \frac{L}{2}\alpha_{Si}(T_{MF} - T_{MF,Cal}) \quad (4.22)$$

where L is one side length of the chip, α_{Si} is the CTE of silicon (base material of the photosensitive chip) and Δp is the position deviation on the chip. The mounting of the chip is assumed to be at the centre position, as evident by the $L/2$ factor.

For distance measurement assessment, the vertical dimension of the chip has to be evaluated (section 3.2.2). That is $L = 5.5 \mu\text{m} \cdot 1088$, i.e. the vertical pixel pitch, $L_p = 5.5 \mu\text{m}$, times the number of pixels in vertical direction. Note that this evaluates the deviation at

the topmost and bottommost pixels of the sensor and can thus be regarded as a worst case scenario. The single point distance deviation is then obtained by

$$\Delta d_{SensorExpansion} = \frac{\Delta p}{L_p} L_{pp}. \quad (4.23)$$

The projected pixel size L_{pp} represents the height of a pixel, if transformed into the laser plane coordinate system. Its value is determined for the typical case as described later in section 4.6.3 as $L_{pp} = 0.64$ mm. The expanded uncertainty due to sensor expansion is modelled by

$$U(\Delta d_{SensorExpansion}) = k \sqrt{c_{\alpha_{Si}}^2 u^2(\alpha_{Si}) + c_{T_{MF}}^2 u^2(T_{MF}) + c_{T_{MF,Cal}}^2 u^2(T_{MF,Cal})} \quad (4.24)$$

with its sensitivity coefficients, determined by derivation of equation 4.22, being

$$c_{\alpha_{Si}} = \frac{L}{2} (T_{MF} - T_{MF,Cal}) \frac{L_{pp}}{L_p} \quad (4.25)$$

and

$$c_{T_{MF}} = \frac{L}{2} \alpha_{Si} \frac{L_{pp}}{L_p}. \quad (4.26)$$

Again, the expected absolute value of 0.37 K for $T_{MF} - T_{MF,Cal}$ as discussed in section 4.4 is used. The CTE of silicon was approximated by $\alpha_{Si} = 3 \cdot 10^{-6}$ K⁻¹ [152] with 10% uncertainty [153], i.e. a standard uncertainty of $u(\alpha_{Si}) = 0.1\alpha_{Si}/\sqrt{3}$. The expanded uncertainty is evaluated by equation 4.24 as

$$U(\Delta d_{SensorExpansion}) = 0.96 \mu\text{m} \quad (4.27)$$

with $k = 2$. This result shows that the sensor expansion can be neglected for the intended use of the CMS.

Sensor-lens distance expansion

Similar to the estimation of sensor expansion, the elongation between sensor and lens system is calculated as in [154] by

$$\Delta p = \frac{L}{2} \alpha_{Al} (T_{MF} - T_{MF,Cal}). \quad (4.28)$$

Note that this is equivalent to equation 4.22, up to the CTE. The factor $\frac{L}{2}$ shows up again due to the geometrical relationship between focal distance f ; maximal angle β between camera axis and incoming ray; and sensor size L , i.e. $\frac{L}{2} = f \tan(\beta)$ [154].

For the conversion to single point distance deviation, equation 4.23 is applied accordingly. The camera casing is made of aluminium, hence the CTE is [152] $\alpha_{Al} = 24 \cdot 10^{-6} \text{ K}^{-1}$ and $u(\alpha_{Al}) = 0.1\alpha_{Al}/\sqrt{3}$ [153].

The standard uncertainty is modelled analogue to equation 4.24 and the sensitivity coefficients are determined as in equation 4.25 and equation 4.26. This leads to

$$U(\Delta d_{SensorLensExpansion}) = 7.7 \mu\text{m} \quad (4.29)$$

with $k = 2$. This effect is also considered as negligible for the aimed application.

Baseline expansion

Besides sensor internal effects, also the distance between laser emitter and camera, i.e. the baseline, is subject to changes by temperature deviations. Following [154],

$$\Delta d_{BaselineExpansion} = \Delta L \tan(90 \text{ deg} - \alpha) = L_b \alpha_{Ss} (T_{MF} - T_{MF,Cal}) \tan(\alpha), \quad (4.30)$$

where L_b is the length of the baseline, α the angle between optical axis of camera and laser emitter and α_{Ss} the CTE of stainless steel. Nominal values of $L_b = 300 \text{ mm}$ and $\alpha = 30 \text{ deg}$ are used. For α_{Ss} an average value from literature, 10^{-6} K^{-1} [152], is used and again 10% uncertainty for that value is assumed [153]. The sensitivity coefficients are calculated as

$$c_{\alpha_{Ss}} = L_b (T_{MF} - T_{MF,Cal}) \tan(90 \text{ deg} - \alpha), \quad (4.31)$$

and

$$c_{T_{MF}} = L_b \alpha_{Ss} \tan(90 \text{ deg} - \alpha). \quad (4.32)$$

The standard uncertainty is evaluated analogue to equation 4.24 as

$$\begin{aligned} U(\Delta d_{BaselineExpansion}) &= k \sqrt{c_{\alpha_{Ss}}^2 u^2(\alpha_{Ss}) + c_{T_{MF}}^2 u^2(T_{MF}) + c_{T_{MF,Cal}}^2 u^2(T_{MF,Cal})} \\ &= 4.8 \mu\text{m} \end{aligned} \quad (4.33)$$

for $k = 2$. Thus, it can be concluded that the effect is negligible for the intended application.

4.5 Influence on the linear motion system

Temperature effects on the linear motion system (section 3.1.2), specifically on its magnetic scale, were experimentally estimated. Therefore, three commercial temperature loggers² were attached near the magnetic scale, as shown in figure 4.8, left.

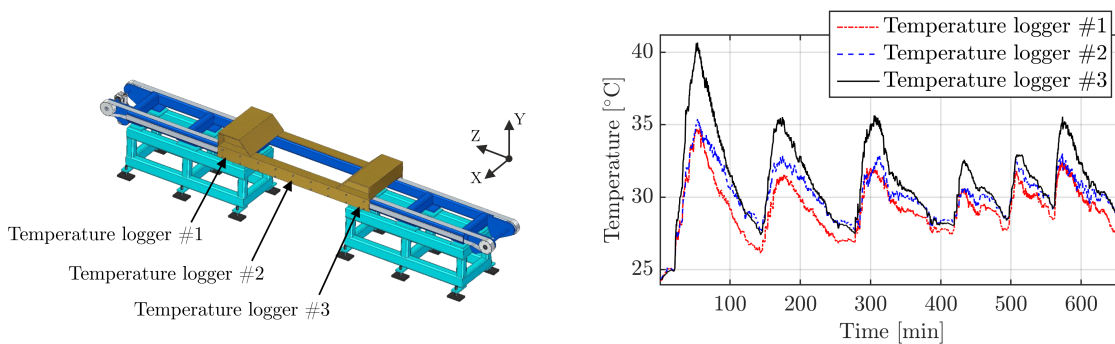


Figure 4.8: Left: temperature logger positions on the linear motion system. Right: temperature logger measurements during a several hour long measurement of workpieces at elevated temperature.

Then, a test was conducted, similar to the one described in section 4.4: a series of forged gas turbine blades at approx. 850°C were individually loaded onto the CMS and moved back and forth until they reached approx. 400°C . Turbine blades were measured continuously, as in normal operation, for over 10 hours with pauses between production batches. Figure 4.8, right shows the temperature readouts of the sensors during the testing. Temperature logger #3 shows the highest magnitude due to its location on the side where workpieces are loaded. The low frequency temperature oscillation emerges from pauses between batches.

The temperature values obtained by the installed temperature loggers make up only three sampling positions along the 860 mm measurement range of the linear motion system. To estimate the complete elongation, linear interpolation and integration is conducted. For each triple of temperature values at time t , intermediate temperature values are obtained by linear interpolation between sampling positions (figure 4.9). The measurement range elongation e_t at time t is then found by integration.

²MicroLite II external NTC temperature USB data logger, LITE5032P-EXT

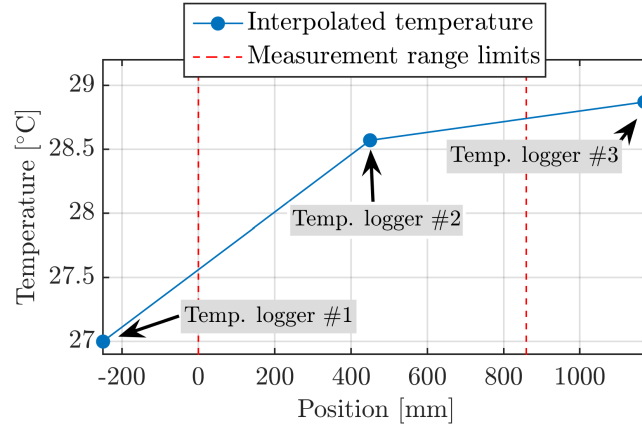


Figure 4.9: Temperature values at minute 650, linearly approximated between sensor positions, measurement range limits shown by vertical solid lines.

Based on the considerations in section 4.3, the deviation on distance measurements depends on the local surface slope by

$$\Delta d_{LinearMotion} = e \tan \theta. \quad (4.34)$$

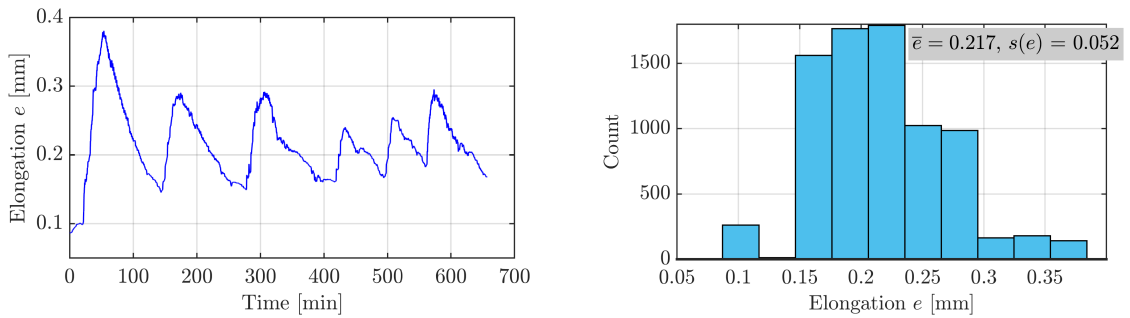


Figure 4.10: Left: time vs. elongation of the measurement range. Right: histogram of elongations with sample mean and sample standard deviation.

Plotting the measurement range expansion e_t for all t during the experiment yields figure 4.10, left. These results, together with equation 4.34 indicate that the elongation on the magnetic scale has an influence in the range of mm and is therefore significant.

The effect is considered as a systematic error and it was decided, that the temperature loggers remain installed on the linear motion system to compensate for this effect during measurements. The residual error after correction and the influence, if no correction is applied, are now quantified.

4.5. INFLUENCE ON THE LINEAR MOTION SYSTEM

The MPE of the temperature loggers is $MPE_{TempLogger} = \pm 0.30^\circ\text{C}$ in the range of -50°C to 150°C , as specified by the manufacturer. The approximate deviation between systematic measurement error and measurement bias [2], originating from temperature logger deviation, is found by applying the above method using an indication of 20.3°C ($= 20^\circ\text{C} + MPE_{TempLogger}$) for all loggers. This results in an observed elongation increase of $6.0\ \mu\text{m}$.

To test for the effect of non-linear temperature behaviour between logger positions, a simple numerical experiment was conducted by the author: considering figure 4.9, assume a discrepancy of 1°C between the linear interpolation and the actual temperature at position $100\ \text{mm}$, i.e. the centre between the first and second temperature logger positions. Including this value in the interpolation leads to an increase of elongation of $6.2\ \mu\text{m}$. The quantity of 1°C is estimated as a worst case by observation of the temperature gradient between temperature loggers, where a maximal deviation along the complete measurement range of approx. 2°C is evident.

Both influences, the error originating from temperature loggers and from finite sampling along the measurement range, are considered independent and their variations are estimated by uniform distributions. The approximate deviation between systematic measurement error and measurement bias can then be quantified as

$$u(e) = \sqrt{\left(\frac{6.0\ \mu\text{m}}{\sqrt{3}}\right)^2 + \left(\frac{6.2\ \mu\text{m}}{\sqrt{3}}\right)^2} = 5.0\ \mu\text{m}. \quad (4.35)$$

Considering equation 4.34, the standard uncertainty is modelled as

$$U(\Delta d_{LinearMotion}) = k \sqrt{c_\theta^2 u^2(\theta) + c_e^2 u^2(e)} + \Delta d_{LinearMotion} (e = E[e], \theta = E[|\theta|]). \quad (4.36)$$

with $c_\theta = e \sec^2(\theta)$ and $c_e = \tan(\theta)$. As expected absolute value of θ , the same value as in section 4.3 is used, $E[|\theta|] = 16.8\ \text{deg}$. For the expected value of e , due to lack of more information, an assumption of $E[e] = 1\ \mu\text{m}$ was made. Straightforward application of statistics would result in $E[e] = 0\ \mu\text{m}$ due to symmetry, what was rated as not realistic. With the declared quantities, the expanded uncertainty is

$$U(\Delta d_{LinearMotion}) = 59\ \mu\text{m} \quad (4.37)$$

with $k = 2$. Repeating the above considerations without correction, values of $E[e] = 220 \mu\text{m}$ and $u(e) = s(e) = 52 \mu\text{m}$ are to be used (figure 4.10, right). Thus

$$u(e) = \sqrt{\left(\frac{6.0 \mu\text{m}}{\sqrt{3}}\right)^2 + \left(\frac{6.2 \mu\text{m}}{\sqrt{3}}\right)^2 + (52 \mu\text{m})^2} = 52 \mu\text{m} \quad (4.38)$$

and

$$U(\Delta d_{LinearMotion}) = 12.7 \text{ mm} \quad (4.39)$$

using $k = 2$. These results demonstrate the effect of temperature influence compensation on the magnetic scale and the need for correction.

4.6 Noise and sampling analyses

In this section, additional effects on specific parts of the system are evaluated and discussed: noise on the camera chip, originating from emanating infrared radiation of the workpiece at elevated temperature; the effect of measurement frequency and linear motion system velocity, since they are part of the measurement strategy and can be adjusted by metrologists; and the effective resolution of a single sensor, using an experimental approach for quantification.

4.6.1 Noise evaluation for workpieces at elevated temperature

In this section, the pixel noise on the camera chip is evaluated to answer if infrared radiation from a workpiece at elevated temperature manifests as noise in the camera image. Note that each sensor is equipped with an appropriate optical bandpass filter with mean wavelength corresponding to the respective laser wavelength and Full Width at Half Maximum (FWHM) of approx. 20 nm. By Wien's displacement law, the wavelength of the maximal radiated energy of a black body can be found as

$$\lambda_{max} = \frac{b}{T} \quad (4.40)$$

where $b = 2.897772 \cdot 10^{-3} \text{ m K}$ is Wien's displacement constant and T the temperature in Kelvin. Assuming a black body and setting $T = (272.15 + 1000) \text{ K}$, i.e. 1000°C , yields a maximal emitted wavelength of $\lambda_{max} = 2.3 \mu\text{m}$ of the workpiece, which is in the near-infrared domain. Two of the sensors operate in the high-wavelength region of the visible

4.6. NOISE AND SAMPLING ANALYSES

spectrum (640 nm and 670 nm) and thermal radiation was suspected to be visible on the camera chip. To validate this hypothesis, the author conducted a noise analysis on image data from both, workpieces at ambient and elevated temperature.

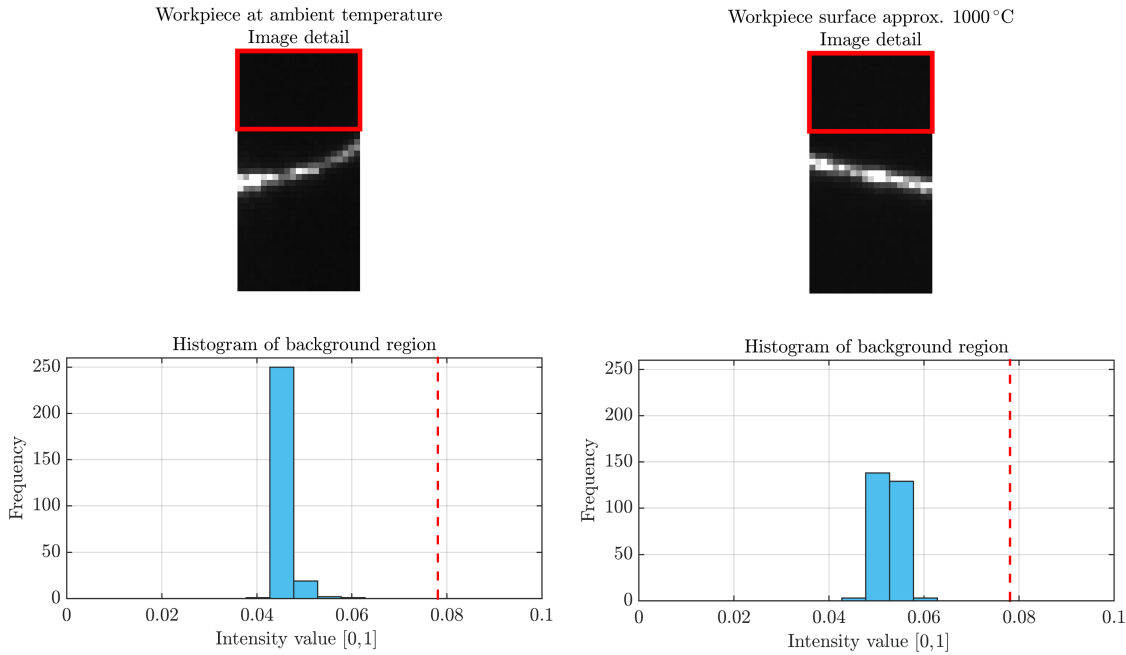


Figure 4.11: Top: image detail of a workpiece at ambient temperature (left) and with surface temperature of approx. 1000 °C (right). Both images are from the sensor with its optical bandpass centred at 670 nm and 20 nm FWHM. The red frame indicates the evaluated background region. Bottom: histograms of the indicated regions of the respective workpiece.

Images from the sensor with the longest wavelength of 670 nm were examined due to its vicinity to the infrared spectrum. The intensity values of pixels, which represent a surface region where no laser light is reflected, are therefore analysed (framed region in figure 4.11, top). These intensities are increased by infrared radiation and/or ambient lighting. For noise analysis on workpieces at elevated temperature, it was ensured that the evaluated image region exhibits thermal radiation, i.e. that a surface region of approx. 1000 °C is imaged. Plotting histograms of the regions indicates their intensity distribution (figure 4.11, bottom).

The camera's internal line extraction algorithm (section 3.2.2) has a tuneable intensity threshold. Only pixels above the threshold are considered in the line extraction procedure. This threshold was set during all experiments to the byte value of 20, or, if scaled to the interval [0,1], to 0.078. In the histograms in figure 4.11, this threshold is depicted as vertical dashed line. Clearly, all intensity values in the evaluated regions fall below the threshold and

are therefore omitted. It can be concluded that neither infrared radiation, for the elevated temperature case, nor ambient lighting influence the measurement.

Note that the optical bandpass filters damp the laser light that is located at the filter's mean wavelength, in this case by approx. 10% as specified by the manufacturer. However, by appropriate exposure time settings, such damping is avoided. The above experiment was conducted with productive exposure time settings, i.e. approx. 10% higher than without a bandpass, thus also amplifying intensities of the background region. Still, the experiment demonstrated that, despite this increase, the measurement is not influenced by infrared radiation nor by ambient lighting.

4.6.2 Measurement time vs. sampling density

By adjusting the velocity of the linear motion system, a metrologist can balance between measurement time and density along the Z-axis, i.e. the density of contours. In this section, deviations on a single point distance measurement, originating from this finite uniform sampling, are modelled.

Since the workpiece surface is linearly approximated during the surface reconstruction step (section 3.2.3 and section 3.2.4), deviations due to the sampling strategy are caused by non-linear surface geometry between sampled positions. For the considered one-dimensional case, such a surface can be described with a constant, non-zero curvature c as $y''(z) = c$ and the surface positions are found by integrating two times as

$$y(z) = c \frac{z^2}{2} + C_2. \quad (4.41)$$

For simplicity, the sampling positions with a sampling distance of d_z are defined at $-d_z/2$ and $d_z/2$ (figure 4.12). Further, no deviation at the sampling positions is assumed, i.e. $y(\pm d_z/2) = 0$. This assumption is made because only the effect of sampling is to be quantified. Consequently, the constant of integration is

$$C_2 = -\frac{(d_z/2)^2}{2}c. \quad (4.42)$$

Plugging this result into equation 4.41 yields the maximal deviation at $z = 0$, that is

$$\Delta d_{\text{Sampling}} = \frac{d_z^2}{8}c. \quad (4.43)$$

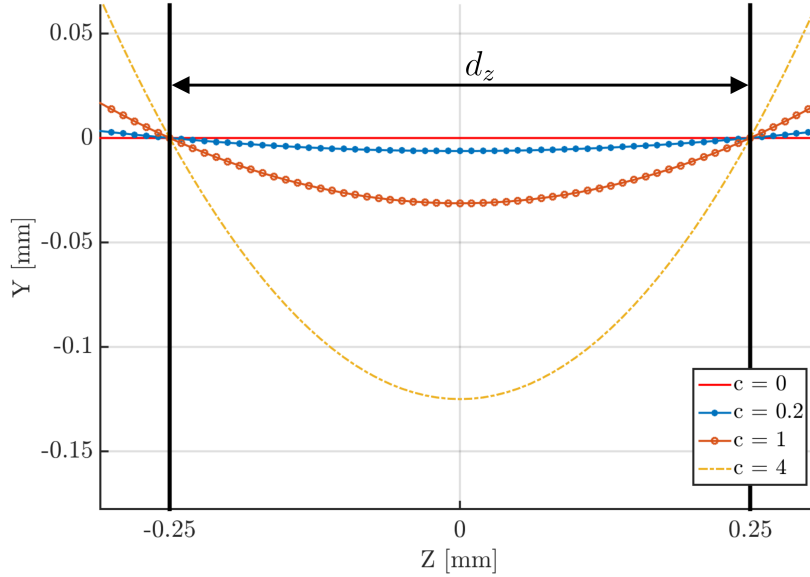


Figure 4.12: Plot of surfaces with different curvature. The y-value at $z = 0$ represents the maximal deviation due to finite sampling.

By this simple relation, the sampling distance d_z , i.e. the moving velocity v and measurement frequency f , can be tuned appropriately based on prior information about the expected curvature c of the workpiece. Since $d_z = v/f$,

$$\Delta d_{\text{Sampling}} = \frac{v^2}{8f^2}c. \quad (4.44)$$

The absolute surface curvature along the Z-axis was estimated analogously as discussed in section 4.3 (figure 4.13), resulting in $u(|c|) = s(|c|) = 1.19 \text{ mm}^{-1}$ and $E[|c|] = 0.59 \text{ mm}^{-1}$. The expanded uncertainty is given by

$$U(\Delta d_{\text{Sampling}}) = k\sqrt{c_c^2 u(|c|)^2} + \Delta d_{\text{Sampling}}(c = E[|c|]) \quad (4.45)$$

with sensitivity coefficient

$$c_c = \frac{v^2}{8f^2}. \quad (4.46)$$

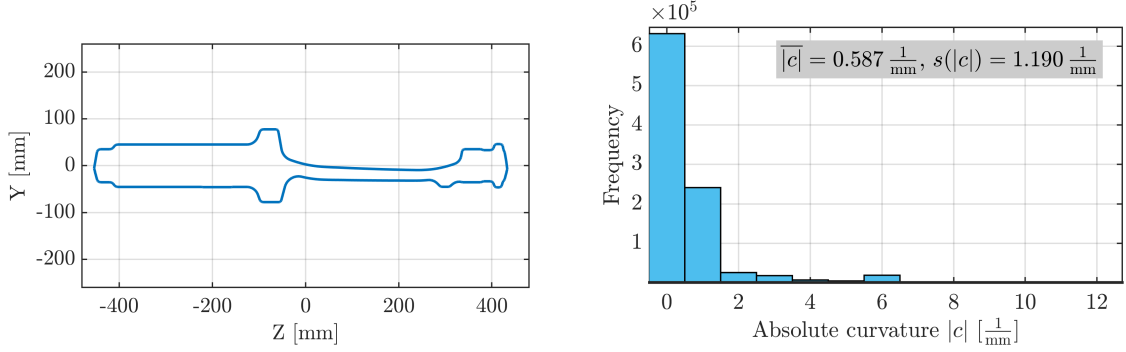


Figure 4.13: Left: section of a gas turbine blade in the YZ-plane, where curvatures along Z-axis were extracted. Right: histogram of absolute curvature $|c|$, including sample mean and sample standard deviation.

Further, set typical values for frequency and velocity, $f = 320$ Hz, $v = 160$ mm/s, respectively. That corresponds to a sampling distance of 0.5 mm and yields

$$U(\Delta d_{\text{Sampling}}) = 93 \mu\text{m}. \quad (4.47)$$

Obviously, this procedure is not specific to any axis. It was applied along the Z-axis because of its typically large sampling distance of 0.5 mm. Moreover, the maximal curvature of gas turbine blades in conducted experiments clearly dominates along this axis over the maximal curvature along other axes. The described model could be extended to the three-dimensional case by considering sampling positions in 3D space and a 2D surface.

4.6.3 Sensor resolution analysis

Since there is no analysis of light sectioning sensor resolution available in literature, to the best of the author's knowledge, the effective resolution of such sensors is analysed in this section. Firstly, note that sensor resolution is subject of this evaluation, not to be confused with the optical resolution of the lens system. Since, in the CMS under consideration, the resolution of the photosensitive chip is the limiting factor and not its optical resolution, the following considerations concentrate on sensor resolution.

To understand depth (along the vertical chip axis) and lateral (along the horizontal chip axis) sensor resolution (section 3.2.2), assume that a flat workpiece is imaged by the sensor. Further, assume a workpiece orientation, such that a horizontal line in the camera image results. The vertical position of the line in the image indicates the distance from the sensor, i.e. the *depth resolution w.r.t the surface* is related to the vertical pixel resolution of the sensor only. On the other hand, the lateral sensor resolution, in this case, defines the

4.6. NOISE AND SAMPLING ANALYSES

sampling density along the workpiece. Consequently, to assess depth resolution w.r.t the surface, only the vertical sensor resolution is of importance – in this specific case. If the workpiece is rotated and results in an arbitrary line on the chip, this simple separation is no longer valid. In the following, the depth resolution w.r.t. the surface and sampling density are to be evaluated in dependence of surface orientation.

For estimation of these quantities, an empirical method is proposed. Briefly, (i) generation of a synthetic image with all pixels active, (ii) transformation of pixel coordinates into the laser coordinate system (section 3.2.2), (iii) evaluation of local pixel distances in depth and lateral direction, (iiii) optional simplification and evaluation of the depth resolution and sampling density w.r.t. the surface. The first two steps are respectively trivial or already discussed; the latter two are described in the following.

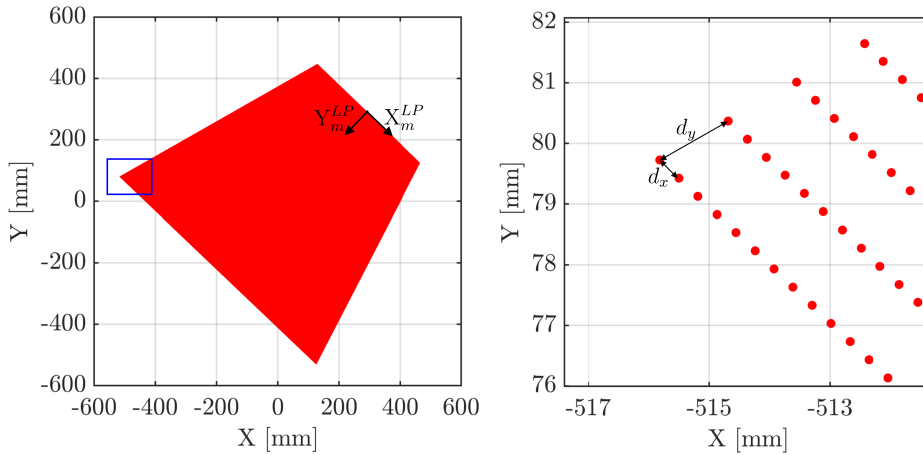


Figure 4.14: Left: all image pixels from sensor 1, transformed into the laser coordinate system, P^1 , together with the transformed image sensor coordinate axes X_m^{LP} and Y_m^{LP} . The rectangle indicates a detail. Right: detail from left with distances d_x in lateral and d_y in depth direction.

All image coordinates, transformed into the laser plane coordinate system are shown in figure 4.14. The magnified detail (figure 4.14, right) depicts how the sensor depth resolution d_y and lateral resolution d_x are evaluated. It can be seen that the depth direction, i.e. the transformed vertical sensor coordinate axis Y_m^{LP} , is position dependent. The projected axis in figure 4.14 is only valid for the horizontal centre of the chip.

Note that the sensor depth resolution is not determined by the pixel distance in the laser plane coordinate system exclusively, but influenced by the line extraction algorithm subpixeling capability, i.e. with the utilised algorithm (section 3.2.2), reduced by factor 16. Thus, the effective sensors depth resolution is $d_y/16$.

CHAPTER 4. SYSTEM CHARACTERISATION

Sensor resolution	Min [μm]	Max [μm]	Typical [μm]
Lateral (d_x)	226	434	310
Depth ($d_y/16$)	21	81	40

Table 4.2: Minimal, maximal and typical values for lateral and depth sensor resolution.

Since projective transformations, i.e. transformation into the laser plane coordinate system (section 3.2.1), do not preserve distances, the sensor resolution is position dependent. Values for minimal, maximal and typical, i.e. in the centre of the measurement area, sensor resolutions are given in table 4.2.

For simplification of the following description, the projected pixel area is assumed rectangular. Thus, Y_m^{LP} becomes constant and the evaluation is position independent – up to the rectangle dimensions. Due to the subpixeling capability of the algorithm, pixel areas are subdivided along Y_m^{LP} into 16 areas. Specifically, this "subpixel area" with typical dimensions from table 4.2 ($d_x = 0.31$ mm, $d_y/16 = 0.04$ mm) is discussed here.

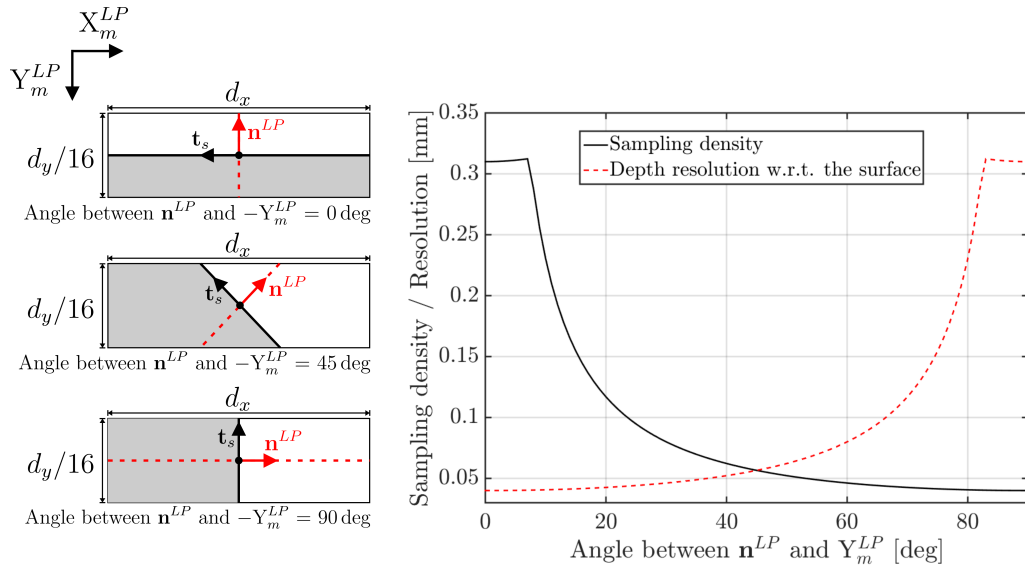


Figure 4.15: Trade-off between depth resolution w.r.t. the surface and sampling density for the typical sensor resolution. Left, top: \mathbf{n}^{LP} is parallel to Y_m^{LP} , resulting in low depth resolution w.r.t. the surface and high sampling density. Left, middle: \mathbf{n}^{LP} is 45 deg rotated to Y_m^{LP} , resulting in equal depth resolution w.r.t. the surface and sampling density. Left, bottom: \mathbf{n}^{LP} is orthogonal to Y_m^{LP} , resulting in high depth resolution w.r.t the surface and low sampling density.

The depth resolution w.r.t. the workpieces surface is identical to the sensors depth resolution if and only if $\mathbf{n}^{LP} \cdot (-Y_m^{LP}) = 1$, where \cdot denotes the dot product, \mathbf{n}^{LP} is the

4.6. NOISE AND SAMPLING ANALYSES

surface normal, projected into the laser plane coordinate system and Y_m^{LP} is the vertical sensor coordinate axis, transformed from image coordinates into the laser plane coordinate system (section 3.2.2). A non-zero angle between projected surface normal and transformed negative sensor axis leads to a trade-off between sampling density and depth resolution w.r.t. the surface (figure 4.15). Descriptively, the length of the surface normal inside the subpixel area represents the depth resolution w.r.t. the surface and the length of the surface tangent inside the subpixel area represents the sampling density (figure 4.15, left).

More formally, pixel limits can be described by lines represented as $([p_x, p_y]^\top, [v_x, v_y]^\top)$, where $[p_x, p_y]^\top$ is a point on the line and $[v_x, v_y]^\top$ is the line direction vector. For the projected pixel dimensions $(d_x, d_y/16)$, this yields for left, right, bottom and top limits

$$l_l = \left(\begin{bmatrix} -d_x/2 \\ 0 \end{bmatrix}, \begin{bmatrix} 0 \\ 1 \end{bmatrix} \right), \quad (4.48a)$$

$$l_r = \left(\begin{bmatrix} d_x/2 \\ 0 \end{bmatrix}, \begin{bmatrix} 0 \\ 1 \end{bmatrix} \right), \quad (4.48b)$$

$$l_b = \left(\begin{bmatrix} 0 \\ d_y/16/2 \end{bmatrix}, \begin{bmatrix} 1 \\ 0 \end{bmatrix} \right), \quad (4.48c)$$

$$l_t = \left(\begin{bmatrix} 0 \\ -d_y/16/2 \end{bmatrix}, \begin{bmatrix} 1 \\ 0 \end{bmatrix} \right), \quad (4.48d)$$

respectively. If the projected surface normal \mathbf{n}^{LP} is also treated as a line $([0, 0]^\top, (\mathbf{n}^{LP})^\top)$, the depth resolution w.r.t. the surface can be obtained by

$$r_d(\mathbf{n}^{LP}) = \min (\|l_r \cap \mathbf{n}^{LP} - l_l \cap \mathbf{n}^{LP}\|, \|l_t \cap \mathbf{n}^{LP} - l_b \cap \mathbf{n}^{LP}\|), \quad (4.49)$$

where $\|\mathbf{x}\|$ denotes the Euclidean norm of vector \mathbf{x} and \cap denotes line-line intersection. The procedure can be applied analogously for evaluation of the sampling density, i.e. by replacing \mathbf{n}^{LP} with the surface tangent vector. Results for different surface orientations are shown in figure 4.15, right.

The standard uncertainty of resolution w.r.t. the surface, for 0 deg between $-Y_m^{LP}$ and \mathbf{n}^{LP} , originating from typical sensor depth resolution is given by

$$u(\Delta d_{Resolution}) = \frac{r_d([0, 1]^\top)}{\sqrt{12}} = \frac{40 \mu\text{m}}{\sqrt{12}} = 11.5 \mu\text{m}. \quad (4.50)$$

This result changes, e.g. for the 45 deg case, to

$$u(\Delta d_{Resolution}) = \frac{r_d([1/\sqrt{2}, 1/\sqrt{2}]^T)}{\sqrt{12}} = \frac{56 \mu\text{m}}{\sqrt{12}} = 16.1 \mu\text{m}. \quad (4.51)$$

Since no a priori information about the projected surface normal is available, equal probability for all normal vector orientations is assumed, i.e. $U(0 \text{ deg}, 90 \text{ deg})$, the uncertainty is approximated by the averaged depth resolution w.r.t. the surface, using a discrete uniform distribution $U\{0 \text{ deg}, 90 \text{ deg}\}$, sampled at each degree. Consequently, the expanded uncertainty is given by

$$U(\Delta d_{Resolution}) = k \frac{\overline{\{r_d([\cos(u), \sin(u)]^T) \forall u \in [0 \text{ deg}, 90 \text{ deg}]\}}}{\sqrt{12}} \text{ mm} = 56 \mu\text{m} \quad (4.52)$$

with $k = 2$. This analysis shows (i) resolution of light sectioning sensors is position dependent, (ii) sensor depth resolution may differ from the depth resolution w.r.t. a surface and (iii) depth resolution w.r.t. a surface depends on the angle between projected surface normal and the projected vertical image axis of the sensor. With these results at hand, a method can be thought of that assigns measurement points a quality quantity, e.g. the inverse depth resolution w.r.t. the surface, to support the data fusion process (section 3.2.3 and 3.2.4). Unfortunately, such a method could not be implemented in the context of the HOTGAUGE research project, although the author believes that it has the potential to improve the systems performance in terms of accuracy.

The proposed procedure is also applicable to the real projected pixel geometry, i.e. a trapezoid. However, the projected sensor axis Y_m^{LP} would become position dependent and the model more complex. The method is also adaptable for the 3D case, however, since the linear motion system speed is adjustable, resolution along the Z-axis is variable (section 3.1.2). Therefore, the third axis was excluded from this analysis. Moreover, the sampling influence along the movement axis was addressed in section 4.6.2.

4.7 Testing at elevated temperature

In order to test the improved metrological performance of the CMS by the proposed methods, bidirectional length measurements were performed on a series of calibrated parts at the forging plant of Pietro Rosa TBM s.r.l. [14].

4.7. TESTING AT ELEVATED TEMPERATURE

At the same time, for acceptable testing costs and testing uncertainty, the calibrated parts should not be too expensive, with curved and optically cooperative surfaces, easy to calibrate with appropriate uncertainty and having small CTE. Experiments were performed using commercially available 130 mm × 70 mm × 4 mm. glass-ceramic plates (Schott Nextrema® [155]) with rounded surfaces in the smallest dimension, having a CTE of $(0.63 \pm 0.2) \cdot 10^{-6} \text{K}^{-1}$ in the range of 20 °C to 300 °C, as stated by the manufacturer. Calibration of the two main dimensions was performed using a scanning tactile CMS (MPE of length measurement = $2,7 + L(\text{mm})/300 \mu\text{m}$) with measurand definition, measuring strategy, i.e. area of interest and point density, and data processing similar to those active while measuring on the optical CMS, obtaining a calibration uncertainty lower than 5 μm.

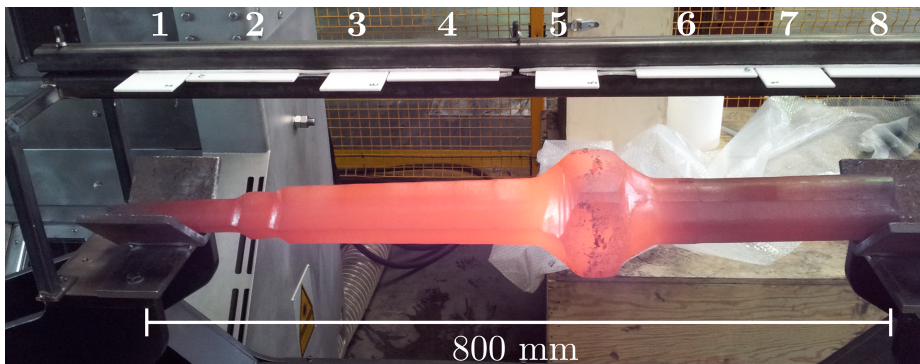


Figure 4.16: Calibrated glass-ceramic plates with low CTE and alternating orientation on a dedicated frame (top) and billet at elevated temperature (bottom) during testing. Glass-ceramic plate numbering as overlay.

To reach environmental conditions as close as possible to those active while measuring actual workpieces, a series of billets at elevated temperature with mass similar to a typical turbine blade were individually loaded onto the CMS and moved back and forth as in normal operation for one hour. During this time, the average temperature of the billet was starting at approx. 850 °C and decreasing to approx. 400 °C before loading the next one. Then, eight calibrated glass-ceramic plates were loaded on a dedicated frame positioned above a billet at about 850 °C (figure 4.16). The plates were fixed in two different orientations, in order to measure the two distinct calibrated lengths of 70 mm and 130 mm. Individual part alignment was on purpose slightly different, resulting in an angle of few degrees between moving direction and corresponding workpiece axis. The glass-ceramic plates and the billet at elevated temperature were measured continuously for 40 minutes, moving backwards and forwards, resulting in 50 measurements with billet temperature decreasing from approx. 800 °C to 300 °C.

CHAPTER 4. SYSTEM CHARACTERISATION

Testing results of length measurements at elevated temperature are given in figure 4.17, showing deviations from the reference values well within the target MPE of the prototype CMS (0.2 mm). Results are corrected for thermal expansion of the plates, using individual average temperature data for each plate. Dimensional stability of the plates was investigated after testing in hot conditions, obtaining deviations within the calibration uncertainty.

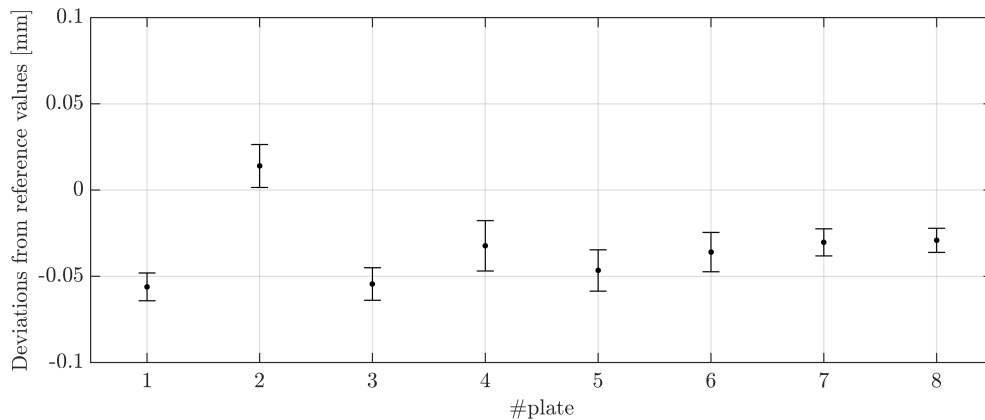


Figure 4.17: Results of testing in hot conditions. Even and odd plate numbers refer to glass-ceramic plates oriented to measure the 70 mm length and the 130 mm length, respectively. Error bars represent the standard deviation of 50 repetitions.

Temperature of the glass-ceramic plates was not measurable by the available pyrometers, due to their partial transparency in the infrared spectrum; therefore, to estimate their temperature, a thermal simulation using ANSYS v.15 [156] was conducted. Radiation effects were simulated using the Gauss-Seidel radiosity solver method, assuming constant emissivity for the billet and the plates. Maximum estimated temperatures of plates are reported in table 4.3, with room temperature of 30 °C. For practical reasons, a single correction value for thermal expansion was computed for each plate, using its average simulated temperature. CMS test uncertainty [157, 158] was determined by information on plates calibration, CTE and temperature values as well as their uncertainty. Test uncertainty resulted to be 9 μm , well adequate for testing the MPE of the CMS.

Table 4.3: Highest temperatures of glass-ceramic plates during testing, as computed using FEM simulation.

#plate	1	2	3	4	5	6	7	8
Maximum plate temperature [°C]	106	126	131	143	152	150	136	106

4.8 Conclusion

In this chapter, evaluation of the identified major error sources was presented. Note that for the designated aim of the CMS (MPE of length measurement = 0.2 mm), influences causing deviations on single measurement point in the 10^{-5} m range are regarded as negligible. It can be seen in table 4.4 that thermal effects on the linear motion system and multisensor registration are the main error sources. Both were corrected by online measurement of the temperature on the linear motion system (section 4.5) and by improved data registration (section 3.2.4), respectively. The influence of the refractive index gradient is rated as a rough estimate due to the limited capability of available models for calculation of the refractive index. The effect of infrared radiation, originating from the workpiece at elevated temperature was also investigated. It was found that the utilised optical bandpass filters are sufficient to exclude influence from infrared radiation and ambient lighting. Additionally, the effective depth resolution, which depends on the surface normal, was analysed for typical workpieces.

Variable	Description	Value [μm]
$U(\Delta d_{MultiSensor})$	Multisensor registration	960 (corrected: 113)
$U(\Delta d_{Refraction})$	Temp. - Refractive index gradient	(rough estimate) 23
$U(\Delta d_{FrameExpansion})$	Temp. - Metrology frame expansion	18.7
$U(\Delta d_{SensorExpansion})$	Temp. - Sensor expansion	0.96
$U(\Delta d_{SensorLensExpansion})$	Temp. - Sensor-lens distance	7.7
$U(\Delta d_{BaselineExpansion})$	Temp. - Baseline expansion	4.8
$U(\Delta d_{LinearMotion})$	Temp. - Linear motion system	12700 (corrected: 59)
$U(\Delta d_{Sampling})$	Sampling (Z-axis)	93
$U(\Delta d_{Resolution})$	Sensor resolution	56

Table 4.4: Expanded uncertainties ($k = 2$) for single point distance measurements Δd for the evaluated influences.

Moreover, a procedure for testing the prototype CMS in hot conditions was shown. The procedure uses glass–ceramic plates, featuring low CTE and two calibrated lengths, mounted on a frame above a billet at elevated temperature. Test results show that the prototype CMS, after more than 1 h of operation in hot conditions, is measuring with bidirectional length measurement errors in the order of 0.05 mm. Test uncertainty was determined using calibration data, CTE and temperature information, resulting to be less than $9 \mu\text{m}$.

CHAPTER 4. SYSTEM CHARACTERISATION

Chapter 5

Production process optimisation

Geometrical deviations due to inappropriate setting of process parameters are one of the main causes for variability in manufacturing of hot forged parts [18]. The described CMS (chapter 3) allows for process-intermittent measurements and enables a closed-loop control of the forging process. The forging step, that is, a complex process with multiple known and unknown process parameters is thus subject to optimisation, though the feedback into the process is non-trivial and is developed in this chapter.

It shall be stressed that measurement results at elevated temperature do not reflect the quality characteristic value after the cooling step. Thus, the cooling process must be taken into account. The cooling has significant impact on the geometry, specifically on the thin aerofoil region of turbine blades [15–17]. However, the final part dimensions do not depend on the cooling process only but also on the forging process parameters as demonstrated for hot forging of an axisymmetric metal wheel [59].

By a measurement system capable of measurement at elevated and ambient temperatures, as the discussed CMS, the effect of the cooling can be characterised by measurements at elevated temperature and after cooling; followed by an appropriate comparison.

In this chapter, firstly, the aims of optimisation are discussed and quality characteristics of turbine blades at elevated temperature are reviewed. In that context, the advantage of asymmetric off-target cost functions for the use in forging is emphasised. The forging and cooling steps are discussed and a characterisation of the forging step by calibrated simulations is presented. Moreover, a computationally cheap approach to predict quality characteristic evolution during cooling is presented.

Next, for the aimed process optimisation, the Setup Adjustment (SA) problem is introduced and discussed in the context of forging. In that framework, a generalised representation of expected off-target cost is presented. The proposal is validated by applying it to

the problem of finding the optimal process setpoint. Based on the proposed representation, an available stopping criterion for process adjustment is generalised, obtaining two distinct criteria for specific application cases. The criteria are then compared to the existing solution and a deadband model. Eventually, a coupled adjustment framework that incorporates the discussed methods is proposed.

5.1 Optimisation aims

Besides the subdivision between offline and online approaches in chapter 2, the aims of efficient forging or forging optimisation found in literature can be partitioned into: optimisation of material properties [58, 159] and optimisation of geometry [15, 59, 60, 160].

In this work, the focus is on online optimisation of geometrical quality characteristics by process adjustment during ramp-up. The objective is minimisation of material loss [23], or in other words, production of near net-shape (final shape) forgings [15, 22]. However, sufficient material must be retained to eventually produce a conforming product. Being able to produce workpieces that are near to the final geometry reduces time exposure for post-forging steps, i.e. reduced cost for machining.

However, since adjustments to the process are not considered free, their number shall be limited. Determination of the optimal number of adjustments, in order to minimise the combined cost of material loss and adjustments, is discussed in-depth in this chapter.

5.2 Quality characteristics for process optimisation

To assess quality on the aerofoil region of a turbine blade (chapter 1) in terms of process optimisation, typically, angular displacement of cross-sections (twist), positional displacement of cross-sections (bow) [15, 23, 61] and an indication of the aerofoil thickness (e.g. mean thickness [23] or maximum thickness [16]) are considered (figure 5.1). These quality characteristics can be evaluated based on so-called *key points* at multiple cross-sections [22, 61] (figure 5.2).

5.2. QUALITY CHARACTERISTICS FOR PROCESS OPTIMISATION

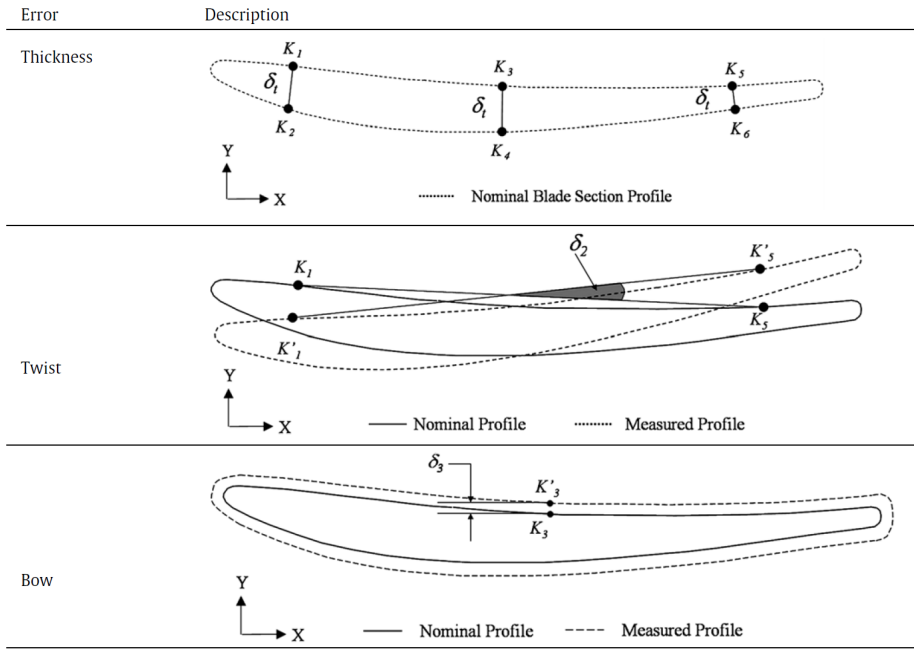


Figure 5.1: Graphical illustration of thickness, twist and bow. Image by Makem et al. [61]

Based on these quantities, Lu et al. [22] propose two aerofoil tolerance measures for the optimisation of forging dies as

$$\delta^{TK}(x_i, z_i) = 1/2 ([g^{TD}(x_i, z_i) - g^{BD}(x_i, z_i)] - [g_0^{TD}(x_i, z_i) - g_0^{BD}(x_i, z_i)]) \quad (5.1)$$

and

$$\delta^{DV}(x_i, z_i) = 1/2 ([g^{TD}(x_i, z_i) + g^{BD}(x_i, z_i)] - [g_0^{TD}(x_i, z_i) + g_0^{BD}(x_i, z_i)]) \quad (5.2)$$

where $g^{TD}(x_i, z_i)$ and $g^{BD}(x_i, z_i)$ are the measured profiles at the top and bottom aerofoil surfaces and $g_0^{TD}(x_i, z_i)$ and $g_0^{BD}(x_i, z_i)$ the nominal profiles at the top and bottom. Thus, $\delta^{TK}(x_i, z_i)$ and $\delta^{DV}(x_i, z_i)$ are respectively the thickness and position deviations along the Y-Axis, at position (x_i, z_i) . By a densely sampled surface representation, as provided by the presented CMS, thickness and position of the aerofoil can be evaluated on more positions than nine key points (figure 5.3).

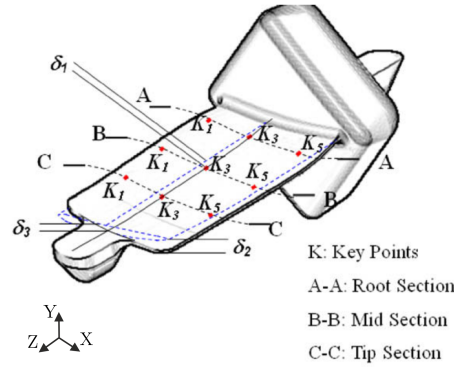


Figure 5.2: Illustration of nine key points on the aerofoil surface, Image by Lu et al. [22], coordinate system adapted.

From the functional point of view, one can argue that the final geometry of a part must at least "fit completely into the forging geometry" to make further processing feasible. By this, it is meant that there exists a rigid 3D transformation, such that the final geometry is completely encased in the forging geometry. If this requirement is not met, the forging is locally lacking material and the desired final shape cannot be achieved without "adding material", regardless of the post-forging step capabilities. This can be formalised as

$$d(u, v) = f(u, v) - n(u, v), \quad (5.3)$$

$$\delta_{OM} = \int_{\{d \in D \mid d > 0\}} d \, dD, \quad (5.4)$$

$$\delta_{UM} = \int_{\{d \in D \mid d < 0\}} d \, dD, \quad (5.5)$$

where $d(u, v)$ is a distance between forging geometry $f(u, v)$ and net-shape geometry $n(u, v)$ at (u, v) on the respective surfaces. Then, two volumes are specified, i.e. "over-metal" δ_{OM} which is additional volume of the forging and "under-metal" δ_{UM} which is the additional volume of the net-shape geometry. To reach net-shape geometry, the aim can be defined as: minimise "over-metal" while avoiding any "under-metal". The above integrals are to be discretised for the use with finite measurement data. This approach requires (i) a procedure that yields a rigid transformation of the net-shape geometry such that it is completely enclosed in the forging geometry and signals if this is feasible or not; and (ii) that post-forging steps are capable of appropriate material removal to extract the *transformed*

5.2. QUALITY CHARACTERISTICS FOR PROCESS OPTIMISATION

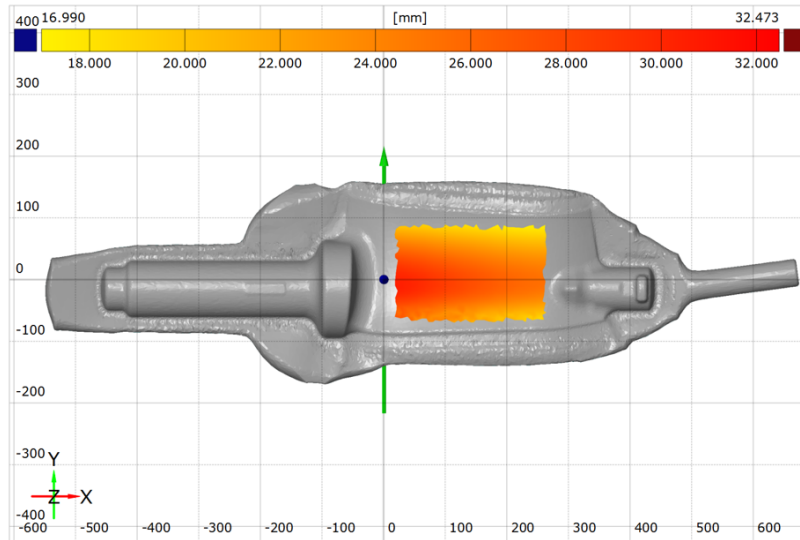


Figure 5.3: Screenshot of GOM Inspect V8 [135]. Evaluation of aerofoil thickness, colour coded.

net-shape geometry from the forging. Former can be achieved by available software registration methods with appropriate tolerancing parameters (e.g. by GOM Inspect V8 [135]). The latter is defined by the available machining equipment.

The purpose of forging tolerances is to have more material than the net-shape geometry. This allows for deviations while still being able to produce a conforming product by removing the additional material through machining processes. The asymmetry of having additional material is reflected e.g. in aerofoil thickness, where falling below the nominal value implicates that the workpiece must be scrapped, while a positive deviation requires additional time for machining. The concept applies similarly for the idea of encasing the final geometry in the forging.

For the following, the maximal thickness of the aerofoil, evaluated by several hundred pointwise measurements, is chosen as quality characteristic of interest. A single quality characteristic was selected to demonstrate the adjustment approach concisely for the univariate case, i.e. for one parameter and one quality characteristic. More sophisticated quality characteristic combinations can be thought of, e.g. minimal and maximal thickness (or "overmetal" and "undermetal") in a bivariate model or even an 18-dimensional model for thickness and positional deviations at the nine key points.

5.3 Process steps

In this section, forging and cooling process steps are discussed. In particular, parameters for forging which are applicable for online adjustment are identified and a characterisation of the forging step, based on calibrated FEM simulations, is presented. To predict the evolution of quality characteristics during cooling, a neural network based approach is discussed.

5.3.1 Forging

For the considered example of closed die forging of X20Cr13 turbine blades, a 400 kJ double-effect counter hammer press was utilised [16, 17]. After approx. 20 blows, the process is stopped and the forgings are placed in calm air for cooling. Process parameters, suitable for online adjustment and a characterisation of their influence are discussed in the following.

Forging parameters

In literature, the shape of dies is often considered as a parameter [22, 24, 61], but also the influence of lubrication and initial billet temperature were examined [59, 160], although not for freeform workpieces. Latter reports state that billet temperature and lubrication have significant influence on the resulting geometry. In addition, the stroke length, i.e. the final opening between the dies, was identified as an important parameter, specifically for the workpiece thickness [59]. By literature research and extensive discussion with experts from metrology, hot forming and FEM simulation, most critical parameters were identified as:

- Die shape
- Die temperature
- Initial billet temperature
- Lubrication
- #Blows / Final die opening

From this list, only the latter two are well adequate for online adjustment. Die shape and temperature are obviously not controllable during production. The initial billet temperature is, however, adjustable during production. Although, a change would require to adjust

parameters for the heating. Such changes need several minutes to take effect and are thus excluded from further analysis.

Forging characterisation

Based on a calibrated forging simulation [16, 17] (Transvalor Forge 2011 [161]), enabled by measurements with the presented CMS, the influence of the selected parameters was quantified. The process response, e.g. the maximal thickness on the aerofoil region, is characterised by a Design Of Experiments (DOE) approach, and subsequent Response Surface Methodology (RSM). A full factorial computer experiment was conducted with the input factors "Final die opening" and "Lubrication", resulting in a linearly interpolated response surface depicted in figure 5.4.

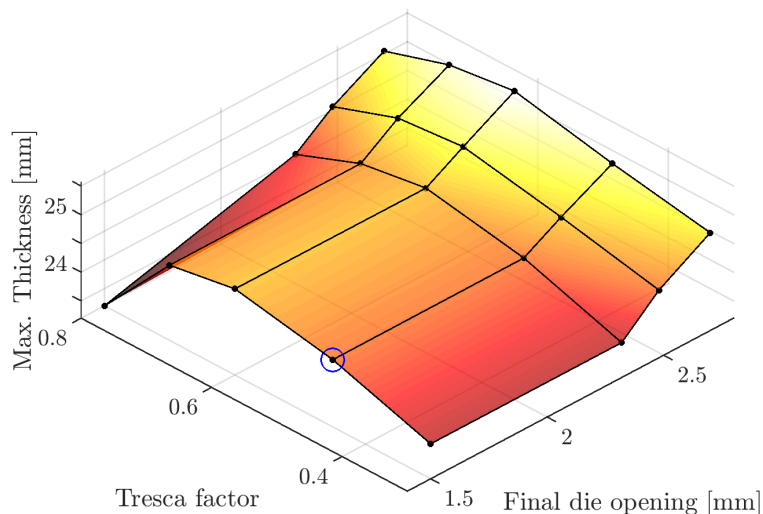


Figure 5.4: Design of experiments for input parameters "Final die opening" and "Tresca factor". The circled point indicates the parameter set of the calibrated simulation.

The points in figure 5.4 represent the computer experiments and the response surface is linearly approximated between them. The circled point indicates the parameter set of the calibrated simulation.

The final die opening was chosen instead of number of blows because the number of blows is an intermediate quantity and does not directly determine the forgings geometry. Note that the energy per blow can vary, so that one blow may change the die opening differently. However, experiments were conducted by varying the number of blows, i.e. the points in figure 5.4 along the "Final die opening"-axis represent different number of

blows (20, 19, 18 and 17). The Tresca factor models the lubrication between workpiece and forging dies in the utilised FEM software. Values of 0.3, 0.45, 0.6, 0.7 and 0.8 were used.

From this result, it can be seen that the last blow (i.e. final die opening of approx. 1.5 mm) has little influence on the maximal thickness on the aerofoil whereas higher openings exhibit an approximately linear relationship. In contrast, the Tresca factor influence shows a non-linear relationship. The information gained by this characterisation is utilised in section 5.4.5 for a coupled process adjustment approach.

5.3.2 Cooling

The cooling process does not only change the volume of the workpiece [59] but introduces geometric distortions on the thin aerofoil region, which must be accounted for [15]. An appropriate design of the cooling process can help to approach near-net-shape geometry for turbine blades [162, 163]. Since measurements are conducted at elevated temperature and quality characteristics shall be verified at 20 °C, the influence of the cooling process must be known sufficiently or be reduced to an acceptable level. To attain this requirement, several approaches can be thought of, e.g.:

- Modelling geometrical distortions during cooling, e.g. by FEM simulation [16, 17].
- Modelling correlations between quality characteristics at elevated temperature and 20 °C (discussed in the next section).
- Minimisation of the cooling process influence down to an acceptable level.

Regardless of the approach used, the measurement uncertainty increases. In this context, establishing the relation between quantities at elevated temperature and 20 °C is regarded as part of the measurement process because the quality characteristics are to be verified at 20 °C [25]. Typically, models do not represent the reality, but are a somewhat simplified abstraction of it. Thus, modelling the cooling or modelling specific quality characteristic evolution will increase a quantities uncertainty due to imperfections in the model. Similarly, a minimisation of the cooling process influence, while not eliminating it, leads to an increased uncertainty.

In the next section, an approach to correlate quality characteristics at elevated temperature and after cooling at 20 °C is discussed. However, for later sections, the method for cooling influence characterisation or minimisation is left unspecified. The proposed methodology is applicable, independent of the procedure for cooling influence quantification.

A neural network approach to quantify the evolution of quality characteristics during cooling

An approach to estimate the evolution of quality characteristics was made, in order to predict the cooling influence in a computationally cheap way. In contrast, a FEM simulation, e.g. by Transvalor Forge 2011 [161], takes several hours, what is not feasible if results shall be used to adjust the forging process during production.

By continuous measurements during cooling and correlation analysis (figure 5.5), quality characteristics most systematically influenced by temperature decrease were identified as twist and bow. Note that such quantities are already utilised to characterise the cooling influence [15] (section 5.2). Additionally, the length of the workpiece shows a systematic correlation unlike the maximal thickness, which displays a less systematic correlation.

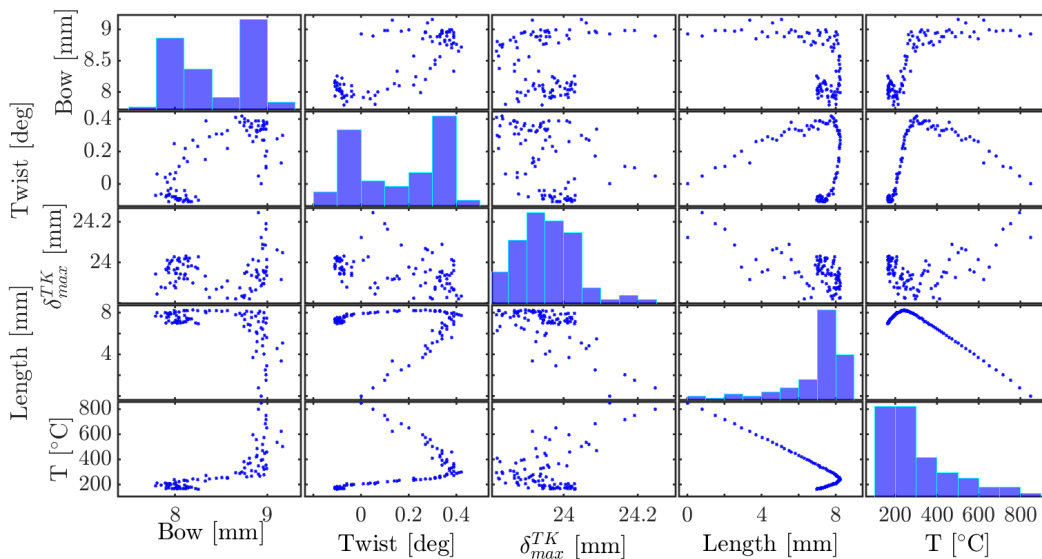


Figure 5.5: Correlation plot of variable pairs between aerofoil temperature T , bow, twist, maximal thickness δ_{max}^{TK} and turbine blade length. Data was obtained by continuous measurement of one turbine blade during cooling. On the diagonal, histograms of the variables are given.

For software implementation of a feed-forward neural network, the MATLAB Neural Network Toolbox 8.3 [132] with the `fitnet` function is used. Input data was extracted from measurements of 17 workpieces, all cooled in calm air. The cooling process is necessarily assumed equivalent for all workpieces.

As input data, the mentioned quality characteristics, together with the sampled mean surface temperature of the aerofoil region and the sampled mean surface temperature of

the turbine blade foot are used. Temperature was measured by two pyrometers in the system (section 3.1). Note that also intermediate measurements, during the cooling, were used as input, obviously with lower temperatures down to approx. 700 °C at the foot of turbine blades. This was done to generate more than the initial 17 datasets, thereby obtaining 169 datasets what allows for more adequate training. The output of the network are the quality characteristic quantities at 20 °C. Their values were measured several hours after the forging process as reference to train the network.

The optimal number of hidden nodes in the network was determined by brute force, i.e. train 1000 networks, keep the best network created, increase the number of nodes by one and repeat. By comparison of the best networks created, the optimal number of nodes between 1 and 10 was found to be 8. The data are subdivided into 70% training, 15% testing and 15% validation. For training, backpropagation of error in conjunction with the Levenberg-Marquardt optimisation algorithm are used. As transfer function, the default hyperbolic tangent sigmoid function `tansig` is employed.

Predictions of the best network for the bow, length and maximal thickness have a standard deviation of approx. 0.2 mm. Those for twist exhibit approx. 0.07 deg standard deviation. Additionally, networks that predict only a single quality characteristic instead of multiple were tested and results were found to have similar standard deviations. The time for prediction is below one second. However, since the MPE for length measurements is 0.2 mm, the results are considered not adequate for the aimed application.

One suspected reason for these relatively large variations is the cooling in calm air being not actively controlled. Variations, induced by the cooling process itself, cannot be accounted for by the discussed approach. Consequently, an increased reproducibility of the cooling process could improve the precision of the predictions. Alternatively, environmental influence quantities, e.g. temperature of the calm air during cooling, could be monitored and included as model input.

5.4 Forging process adjustment

In this section, online optimisation with special focus on process adjustment of the forging process is discussed. Note that, whenever feasible, no units are stated. The discussed methods are applicable regardless of the actual quantity magnitude. Off-target cost functions, i.e. models for cost that are caused by deviations from a nominal value, are denoted by the term *cost function* for the sake of readability.

The general concept of process control is shown in figure 5.6. In the previous sections, controllable inputs and appropriate quality characteristics for the turbine blade example were identified and selected. Clearly, uncontrollable inputs, e.g. raw material properties or environmental effects, also influence the process. Offline optimisation methods, e.g. the above presented DOE approach, lack to include variation of such influences. By online optimisation approaches, such variations can be accounted for.

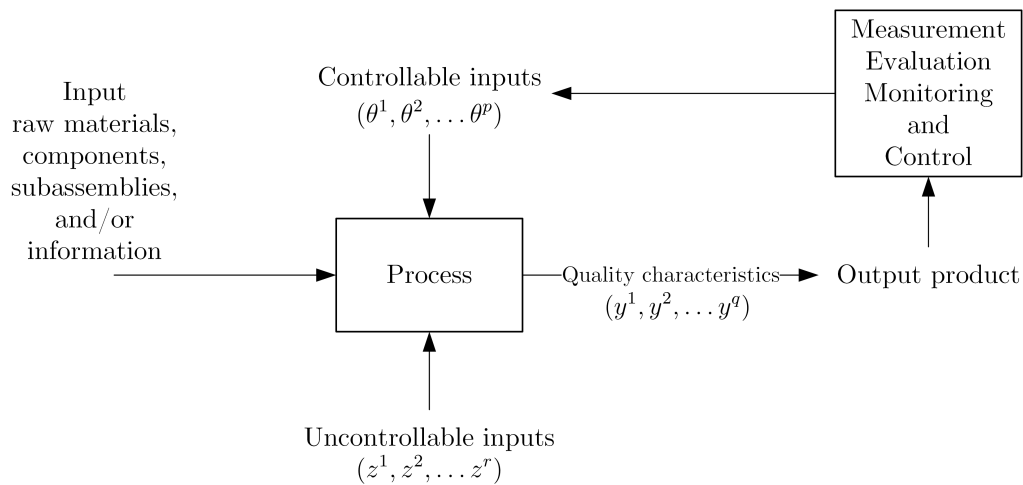


Figure 5.6: Production process inputs and outputs. Adapted from Montgomery [1].

5.4.1 Assumptions and model selection

The production of turbine blades is assumed to have no dead time, i.e. a change in the process parameter values has an immediate effect on the quality characteristic quantity. In the domain of discrete part manufacturing, this means that the next to be produced workpiece is affected.

Due to typically small batch production (50 to 100 parts) in the considered application, the ramp-up of the process is crucial and, due to custom parts, optimal production parameters may differ from batch to batch. Thus, the focus is on parameter adjustment during the ramp-up phase. The forging process is assumed as a *setup dominant* process [64], i.e. quality characteristics of interest have a constant mean, or, the process is stationary. Note that centring of the process is the objective and its variance is assumed to remain constant.

In literature, two classes of this problem can be found (chapter 2). In this work, the focus is on the SA problem class, which assumes as specific process model but allows parameter values to be specified as unknown or only partly known. Alternative methods make use of

historic data, which are typically not available for the case of customer specific products. Additionally, process parameters are treated as observations, i.e. they are considered as known [66]. This is not appropriate for the final opening of the dies nor for the lubrication, which are both not easily quantifiable during production.

5.4.2 Process capability

Process capability and the various Process Capability Indexes (PCI), e.g. C_p , C_{pk} , are not explicitly discussed in this chapter. To assess the short time process capability, already an appropriate adjustment of the process is presumed [10], what is the main objective of the methodology presented.

However, it shall be noted that for assessment of process capability (short, medium or long-term), the uncertainty arising from the measurement system must be considered to obtain an unbiased result. Approaches to exclude the influence of the measurement system on PCIs are given by Weckenmann and Rinnagl [164] and Villeta [165, 166].

5.4.3 A numerical approach to the setup adjustment problem

The SA problem was initially proposed by Grubbs in 1954 [68]. He considered an improper machine setup in discrete metal part manufacturing, resulting in a systematic error in the quality characteristic of interest. The problem is to adjust the setup dominant production process appropriately. Grubbs proposes two rules, the "harmonic rule" and the "extended rule" as they were termed later by Trietsch [26]. Both rules assume a quadratic cost function, i.e. $c(y) = y^2$, where y is, without loss of generality, the deviation of the quality characteristic quantity from its nominal value. He models process and measurement variations as normally distributed. If no information about the initial process setpoint are available, he showed that the optimal adjustment is $U_i = \frac{y_i}{i}$ where U_i is the parameter adjustment quantity at part i , i.e. the value by which the parameter is to be adjusted.

If there is information on the initial process setpoint, e.g. the setpoint can be modelled as normal distribution with variance τ^2 , he shows that the optimal adjustment is $U_i = \frac{y_i}{i + \sigma_v^2/\tau^2}$ where σ_v^2 is the variance due to process variation and measurement deviations.

Grubbs' solutions were studied and extended by several authors [9, 26, 65, 70, 72, 73, 83, 167–169]. For the univariate case, the production process is typically modelled as [26, 65, 68, 72, 73]

$$Y_i = \theta_i + \nu_i, \quad (5.6)$$

where Y_i is, without loss of generality, the deviation of a quality characteristic quantity from its nominal value of the i th part. θ_i is the (unknown or partly known) *process setpoint* and $\nu \stackrel{iid}{\sim} N(0, \sigma_\nu^2)$ models process variation and measurement deviations. The latter is termed *process variation* in the following.

Updating the process setpoint is modelled as

$$\theta_i = \theta_{i-1} + U_{i-1}, \quad (5.7)$$

where U_{i-1} is the parameter adjustment quantity at part $i - 1$. Clearly, equation 5.7 is a significant simplification of many production processes, i.e. the parameter adjustment is correlated by multiplicative identity to the process setpoint.

Equations 5.6 and 5.7 make up a state-space representation of the process, the former is the measurement equation and the latter the state transition equation. The objective is to find the optimal adjustment U_{i-1}^* at every state $i - 1$, i.e. part $i - 1$, which is [72, 73]

$$U_{i-1}^* = \mu_i^* - \mu_{i-1}. \quad (5.8)$$

Here, μ_i^* is the optimal process setpoint for the next step i and μ_{i-1} is an estimate of the current process setpoint. An available method to determine the current process setpoint μ_{i-1} and a novel approach to evaluate the optimal process setpoint μ_i^* are described in the next sections.

Approximation of the current process setpoint

To outline the approach for parameter estimation, the work of Colosimo et al. [65] and Lian & Castillo [72] is followed and their Bayesian inference approach for the univariate case with a priori known σ_ν^2 is shortly reviewed.

Let $i - 1$ be the part just produced, the following procedure is applied before producing part i . The initial process setpoint, i.e. the prior, is modelled as $\theta_0 \sim N(\mu_0, \tau_0^2)$ and $Y_1|\theta_0 \sim N(\theta_0 + U_0, \sigma_\nu^2)$ with μ_0 and τ_0^2 assumed to be known.

At part $i - 1$, a quality characteristic value y_{i-1} is obtained. A posterior distribution of the process setpoint can then be given as $\theta_{i-1}|Y^{(i-1)}, U^{(i-1)} \sim N(\mu_{i-1}, \tau_{i-1}^2)$, where $Y^{(i-1)}$

represents the set of all y 's up to and including y_{i-1} and analogously for adjustments $U^{(i-1)}$. By their model, the posterior predictive density is

$$Y_i | Y^{(i-1)}, U^{(i-1)} \sim N(\mu_{i-1} + U_{i-1}, \sigma_\nu^2 + \tau_{i-1}^2). \quad (5.9)$$

The model is applied iteratively as new parts are measured. It can be shown that for a non-informative prior $\mu_0 \rightarrow 0$ and $\tau_0^2 \rightarrow \infty$, i.e. having no information about the initial process setpoint, this model simplifies to the sample mean and sample variance [170]. Alternatively, more sophisticated models exist, which consider the parameter of the process variation σ_ν^2 as only partly known [72, 73]. Its distribution is estimated during application of the model. However, for concise presentation, sufficient information about process and measurement variance is assumed.

In the presented approach, conjugate distributions [170] were used. This allows for closed-form update rules for the process setpoint distribution parameters as

$$\mu_{i-1} = \frac{\frac{\mu_{i-2} + U_{i-2}}{\tau_{i-2}^2} + \frac{y_{i-1}}{\sigma_\nu^2}}{\frac{1}{\tau_{i-2}^2} + \frac{1}{\sigma_\nu^2}} \quad (5.10)$$

and

$$\frac{1}{\tau_{i-1}^2} = \frac{1}{\tau_{i-2}^2} + \frac{1}{\sigma_\nu^2}. \quad (5.11)$$

Descriptively, the estimation of the process setpoint is iteratively improved while new parts are manufactured and measured, starting with a prior belief of the process setpoint.

Note that other distributions are feasible, and are evaluated analogue as the above example if they make up a conjugate pair. If not, the posterior can be evaluated numerically, e.g. by Markov Chain Monte Carlo (MCMC) or Sequential Monte Carlo (SMC) methods [9].

Non-identity parameter relation For many applications, as turbine blade forging, the relation between parameter and quality characteristic is more complex than in the above SA model (section 5.3.1). A few authors introduce a linear, non-identity relationship [70, 74], however, not for a Bayesian formulation. Lian et al. [73] propose as outlook of their work the state transition equation

$$\theta_i = \theta_{i-1} + aU_{i-1}. \quad (5.12)$$

Consequently, U_{i-2} is to be replaced in the update rule (equation 5.10) by aU_{i-2} and the optimal adjustment U_{i-1}^* would be found by $U_{i-1}^* = \frac{\mu_i^* - \mu_{i-1}}{a}$. These relations are used in section 5.4.5 to incorporate information from offline process characterisation (section 5.3.1).

Approximation of the optimal process setpoint

In the last section, a state-of-the-art procedure to estimate the current process setpoint was discussed. In this section, a method to estimate the optimal process setpoint, μ_i^* , at any part i during production is proposed. With those two quantities at hand, equation 5.8 can be solved and optimal adjustments can be obtained.

Deviations of a quality characteristic from its nominal value, y , are compared not only against tolerance limits but can also be penalised by a cost function (e.g. [65, 73]) (also loss model, e.g. [26, 77]). Taguchi's famous quadratic cost function $c(y) = c^q y^2$ [171] (figure 5.7, left), to estimate the loss to society, is often used, also because of its mathematical tractability [73]. The tolerance limits in this chapter are, if not stated differently, $LSL = -1$ and $USL = 1$, without loss of generality.

With the quadratic cost model, small deviations from the nominal value cause cost, even if the characteristic is still inside tolerances. This philosophy is motivated by considering customer dissatisfaction through reduced quality [77, 171].

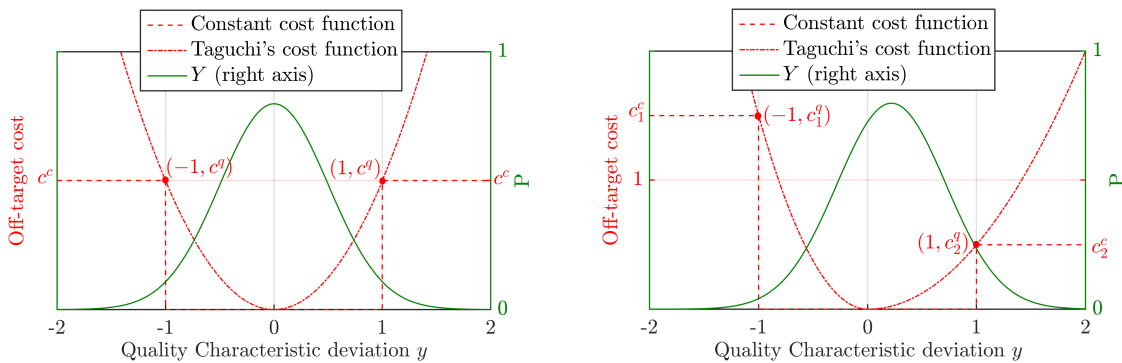


Figure 5.7: Taguchi's quadratic cost function (dash-dotted red line) and constant cost function (dashed red line) together with a standard normal quality characteristic distribution (solid green line). Left: symmetric case. Right: asymmetric case, the optimal process setpoint deviates from zero, e.g. for quadratic cost.

However, cost functions can be more complex in order to reflect real cost incurred by deviations from the nominal value. Asymmetric cost functions are considered if deviations to one side cause more cost than on the other (figure 5.7, right) [43, 65, 73, 77]. The

thickness of a turbine blade aerofoil is such an example: the cost of a negative thickness deviation will be much higher than a positive deviation, since negative deviations cannot be recovered by post-forging processes and the part has to be classified as defective.

For symmetric distributions of a quality characteristic and symmetric cost functions, the optimal process setpoint is equal to the nominal value, independent of the parametrisation of both (figure 5.7, left). However, for asymmetric quality characteristic distributions, e.g. due to an asymmetric process variation distribution or asymmetric cost functions, the optimal process setpoint deviates from the nominal value. In the asymmetric case, it depends on the parametrisation of process variation and cost function (figure 5.7, right and figure 5.8). Therefore, the optimal process setpoint must be determined.

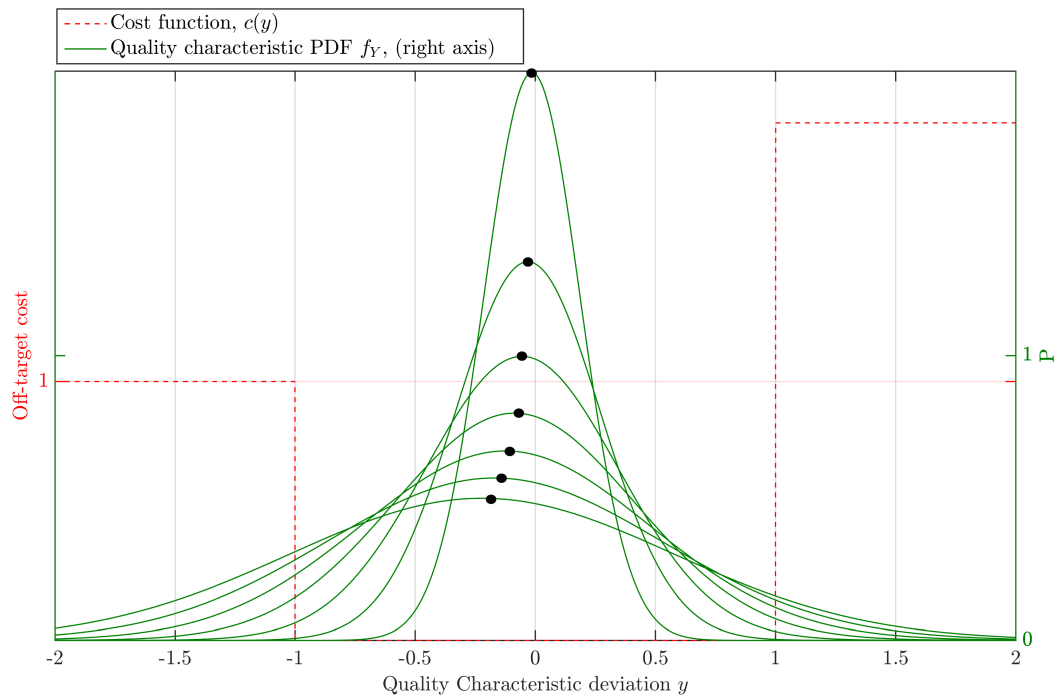


Figure 5.8: Dependence of the optimal process setpoint on the quality characteristic variation $\sigma_v^2 + \tau_i^2$ for an asymmetric constant cost function and normally distributed process variation, depicted for values $(\sigma_v^2 + \tau_i^2) = (0.2, 0.3, 0.4, 0.5, 0.6, 0.7, 0.8)$. Optimal setpoints are indicated by black dots at the maximum of the quality characteristic distribution.

Several closed-form solutions for different combinations of cost function and quality characteristic variation can be found in the literature [43, 65, 73, 76–78].

The solution for the optimal process setpoint for a quality characteristic y is found by minimising the *expected cost* $E[c]$ (e.g. [65, 73], also termed average quality loss [78] [76]). Note that the expected cost represent only cost from being off-target.

For a constant asymmetric cost function and a normally distributed process variation, the expected cost is found by [65]

$$E[c^c(i)] = c_1^c \int_{-\infty}^{LSL} f_N(y_i; \mu_i, \sigma_i^2) dy_i + c_2^c \int_{USL}^{\infty} f_N(y_i; \mu_i, \sigma_i^2) dy_i, \quad (5.13)$$

where c_1^c and c_2^c are the constant cost (figure 5.7, right) on the negative and positive side, respectively. $f_N(y; \mu, \sigma^2)$ is the probability density function of $N(\mu, \sigma^2)$, evaluated at y with μ and σ^2 as process setpoint and the variance of the process variation, respectively. Colosimo et al. [65] find the minimal expected cost by partial derivation. Their notation was slightly adapted for better clarity.

However, for some combinations, no closed form solution for the optimal process setpoint exists and numerical computation is required [43, 65, 73]. This applies for e.g. a quadratic asymmetric cost function (figure 5.7, right) and normal quality characteristic variation as

$$E[c^q(i)] = c_1^q \int_{-\infty}^0 y_i^2 f_N(y_i; \mu_i, \sigma_i^2) dy_i + c_2^q \int_0^{\infty} y_i^2 f_N(y_i; \mu_i, \sigma_i^2) dy_i, \quad (5.14)$$

where c_1^q and c_2^q are the distinct quadratic cost coefficients (figure 5.7, right), i.e.

$$c(y) = \begin{cases} c_1^q y^2 & \text{if } y < 0 \\ 0 & \text{if } y = 0 \\ c_2^q y^2 & \text{if } y > 0. \end{cases} \quad (5.15)$$

Note that determining the optimal process setpoint is closely related to the problem of finding the optimum steady state setpoint of a process, i.e. the optimal process setpoint as $i \rightarrow \infty$ [65, 75, 78]. Although, for asymmetric cost functions, due to increasingly precise estimation of the process setpoint, the optimal setpoint during adjustment does not coincide with the steady state setpoint (figure 5.8).

In the following, a numerical approach is proposed. It approximates the optimal current and steady state process setpoint for arbitrary cost functions and quality characteristic variations. Moreover, it is applicable for the multivariate case.

Method description Rearranging equation 5.14 yields

$$E[c_i^q] = \int_{-\infty}^{LSL} c_1^q y_i^2 \cdot f_N(y_i; \mu_i, \sigma_i^2) dy_i + \int_{USL}^{\infty} c_2^q y_i^2 \cdot f_N(y_i; \mu_i, \sigma_i^2) dy_i. \quad (5.16)$$

From that, it can be observed that the two involved integrals are in fact the cross-correlation of cost function, e.g. $c_1^q y_i^2$, and the quality characteristic's probability density function with variance of process variation σ_i^2 and process setpoint μ_i .

Consequently, given a process variation ν , a distribution for the process setpoint estimate θ and a cost function $c(y)$, the author proposes the following generalised definition for the expected cost

$$E[c(\nu, \theta)] = \int_{-\infty}^{\infty} c(t) f_{\nu+\theta}(t) dt, \quad (5.17)$$

where $f_{\nu+\theta}(t)$ is the probability density function of $\nu + \theta$, evaluated at t . Considering the measurement equation (equation 5.6), this can be written as

$$E[c(Y)] = \int_{-\infty}^{\infty} c(t) f_Y(t) dt. \quad (5.18)$$

The process setpoint μ , that generates the minimum expected cost, is the optimal process setpoint, found by

$$\mu^* = \arg \min_{\mu} E[c(Y)]. \quad (5.19)$$

The asymmetric case from figure 5.7, right, with its discrete cross-correlation and its minimum is shown in figure 5.9.

The approach is adaptable for the higher dimensional case with multiple quality characteristics $\mathbf{y} = (y^1, y^2, \dots, y^q)$ having a joint probability density $f_{(Y^1, Y^2, \dots, Y^q)}$. Cost functions $c_k(y^k)$ can be considered e.g. as additive [70], $c(y^1, y^2, \dots, y^q) = \sum_{k=1}^{k=q} c_k(y^k)$.

Thus, the expected cost are given by

$$E[c(Y^1, Y^2, \dots, Y^q)] = \int_{\mathbb{R}^q} c(\mathbf{t}) f(\mathbf{t}) dt. \quad (5.20)$$

5.4. FORGING PROCESS ADJUSTMENT

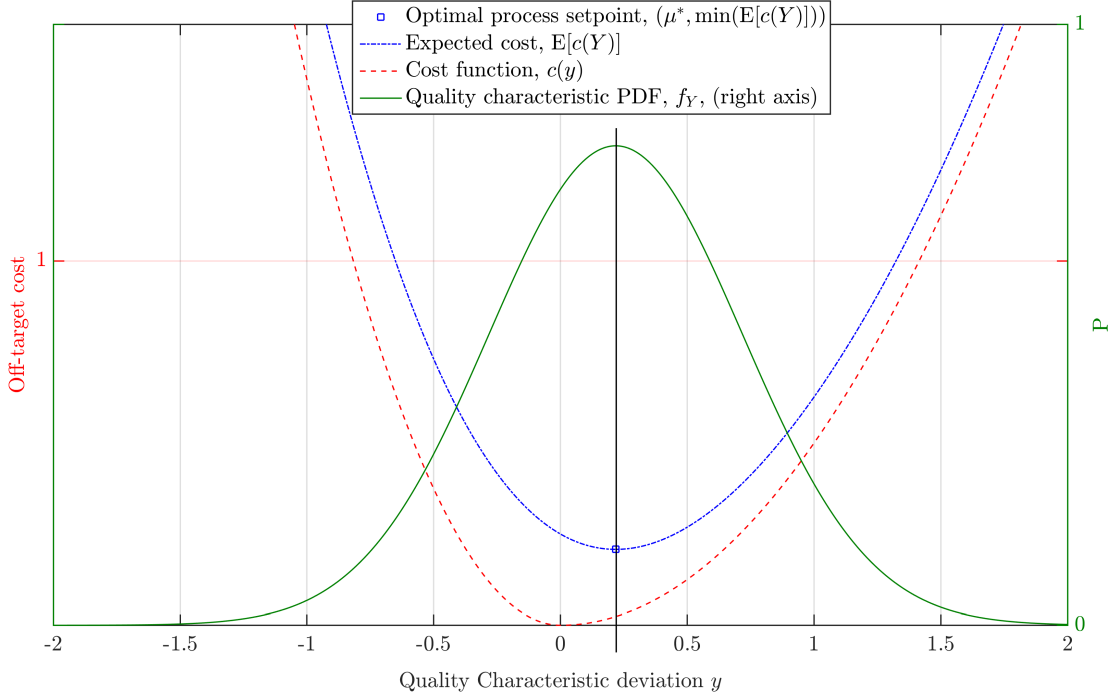


Figure 5.9: Expected cost and optimal process setpoint for an asymmetric quadratic cost function. The optimal process setpoint is determined by the proposed method.

Note that finding the optimal process adjustment U_{i-1}^* is independent of the method to estimate the current process setpoint [168]. Consequently, the above procedure is applicable for other process adjustment methods that utilise the optimal process setpoint, e.g. [65, 70, 72, 73, 167].

Computer implementation and validation Discrete variants of equation 5.18 and equation 5.19, with discrete variants of cost function and process variation are used for computer implementation. Bounds of integration of equation 5.18 were set to appropriate values, in order to cover the entire region of the potential optimal process setpoint.

To find the minimal expected cost efficiently, assumptions about the involved distribution and cost model are made: if the process variation satisfies (i) positivity (all values are positive), (ii) unimodality (A sequence is unimodal if it is first ascending (descending) and then descending (ascending)) and (iii) is integrable ($\sum_{y=-\infty}^{y=\infty} f[y]$ is finite), then it can be considered as a discrete scale-space kernel [172].

In the considered application, (i) and (iii) hold; (ii) is not necessarily true but typical since, due to many (independent) influences, the process variation is often approximately

normally distributed. If all assumptions hold, it was shown that convoluting with the cost function does not create new local extrema [172]. Convolution by $f(-y)$ is equivalent to cross-correlation with $f(y)$. By negating the parameter y , the above assumptions still hold and consequently no new local extrema are created by cross-correlation with a scale-space kernel.

If it is further required that the cost function $c[y]$ is also unimodal and has exactly one minimum, then $E[c[Y]]$ has one or zero minima. This implies that there is one optimal μ ; or if there is no minimum in $E[c[Y]]$, cost do not depend on the process setpoint what would dispense the need for process adjustment.

For a computer implementation of the proposed method, MATLAB 2015a [132] was used. The minimiser $\hat{\mu}^*$ is found through numerical optimisation by use of the `fminbnd` function, which applies a combination of golden section search and parabolic interpolation; both methods find extrema in unimodal functions. If the involved cost function and process variation distribution do not meet the discussed restrictions, more sophisticated optimisation methods are to be used.

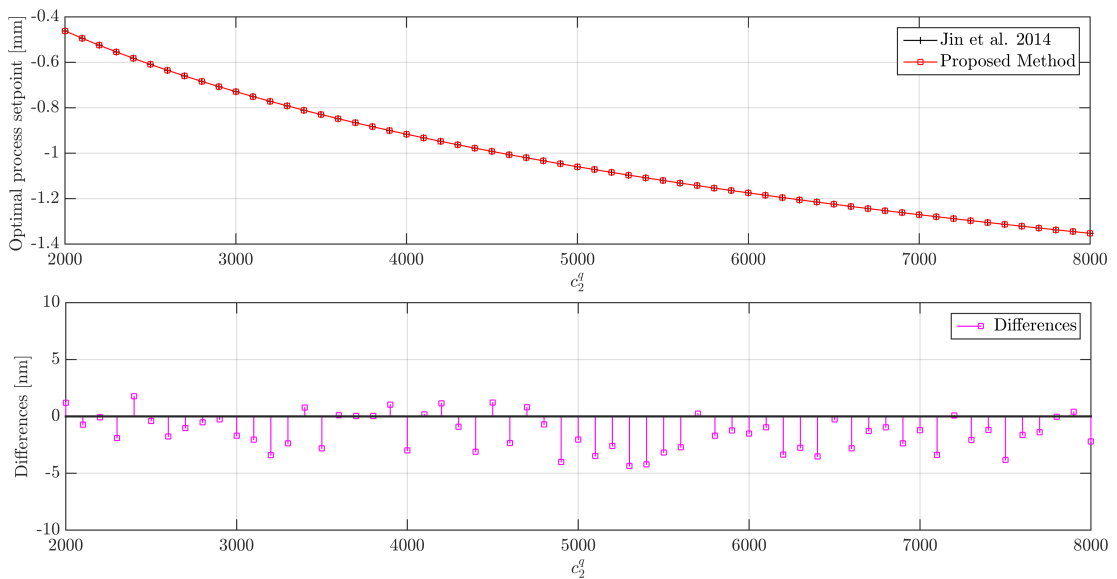


Figure 5.10: Comparison of the proposed method for $c_1^q = 1000$ and varying c_2^q with Jin et al. 2014

To validate the method, comparisons with two studies from literature were made. Recently, Jin et al. [77] stressed the importance of non-normal process variation. Exemplary, the case of a triangular process variation, combined with an asymmetric quadratic cost function was evaluated. Cost at the lower tolerance limit were fixed to $c_1^q = 1000$ units and cost

5.4. FORGING PROCESS ADJUSTMENT

at the upper tolerance limit c_2^q were adjusted between 2000 and 8000 units in steps of 100 units. Results and differences between the methods are given in figure 5.10.

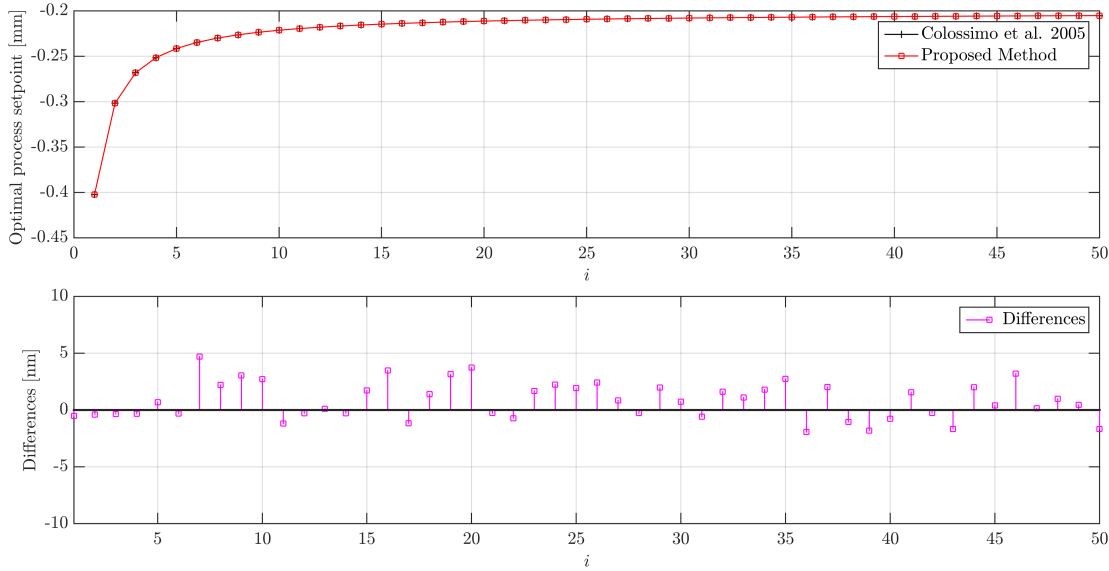


Figure 5.11: Comparison of the proposed method for $c_1^c = 1000$, $c_2^c = 5000$ with Colossimo et al. 2005 [65]

The second comparison was done with Colosimo et al. [65]. During the SA process discussed therein, the estimated variation of the quality characteristic changes due to additional information about the current process setpoint (section 5.4.3). The experiment was conducted for a constant asymmetric cost function ($c_1^c = 1000$, $c_2^c = 5000$) for the first 50 steps of process adjustment. In figure 5.11, the optimal process setpoint and differences between the closed form solution and the proposed method are shown.

Results show that the proposed approach can approximate closed form solutions with an accuracy in the order of 10^{-5} mm (figure 5.10 and figure 5.11, bottom) for a possible range for the optimal process setpoint of 5.96 mm what corresponds to approx. 0.00017% deviation to the closed form solution for the former case. Similar deviations are evident for the latter case, with a possible range for the optimal process setpoint of 14 mm, what corresponds to approx. 0.000071% deviation. The computation time for \hat{y}^* by the proposed method on a state-of-the-art commercial laptop¹ is in both examples below 0.2 seconds. If arbitrary cost functions and process variation distributions are to be used, more sophisticated optimisers become necessary.

¹Intel Core i7-4700MQ @2.4 GHz, 8 GB RAM, Windows 7

The above experiments were repeated with particle swarm optimisation using an initial population of 100 samples from a uniform distribution covering the search space. Equivalent results were observed and computation time increased to approx. 2.5 seconds for both cases. However, this computation can be done offline, i.e. before the production process starts, when no strict timing constraints must be met.

Since the author could not find multivariate examples for optimal process setpoint determination in the literature, no comparison is made for the multivariate case. However, for demonstration, an example for the bivariate case, i.e. $q = 2$, is shown in figure 5.12. An asymmetric constant cost function and an asymmetric quadratic cost function for the respective quality characteristics were used, together with a bivariate normal distribution for process variation. To approximate the minimiser of $E[c(Y^1, Y^2)]$, the MATLAB [132] function `fminsearch` is utilised which uses the variant of the simplex search method [173]. The computation time is in the order of 1 second. Due to naive implementation, the resolution was limited to $5 \mu\text{m}$ for a tolerance range of 2 mm in both dimensions, i.e. 2.5%, due to limited RAM.

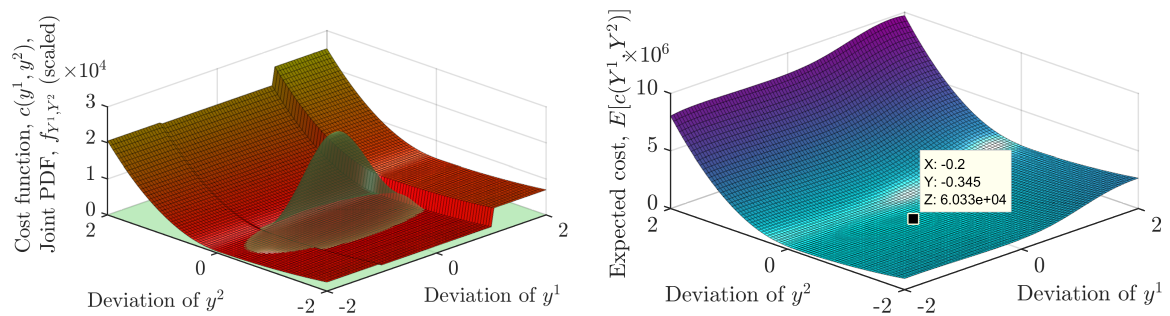


Figure 5.12: Bivariate case with quality characteristics y^1 and y^2 . Top: cost function $c(y^1, y^2)$ and joint probability distribution f_{Y^1, Y^2} . Bottom: expected cost $E[c(Y^1, Y^2)]$ and its found minimiser.

It shall be pointed out that solving the discrete variant of equation 5.20 for large q is numerically not straightforward. More sophisticated, possibly approximative, integration methods, e.g. (Quasi-)Monte Carlo integration [174], are necessary to keep the computation time feasibly low. In addition, non-creation of new extrema for $q > 1$ is not guaranteed by the discussed requirements [172] and sophisticated search procedures may be necessary.

Incorporating measurement uncertainty Following ISO 14253-1 [175], an uncertainty range around the specification limits exists, defined by the expanded measurement uncertainty U of the measuring system (figure 5.13). In those regions, no conformity/non-conformity statement about a quality characteristic can be made. Depending on the strategy for results that fall in that range, the cost function is to be adapted. If quality characteristics in that range simply cause classification as defective, cost in regions B (figure 5.13) rise to the respective constant cost on the negative and positive side.

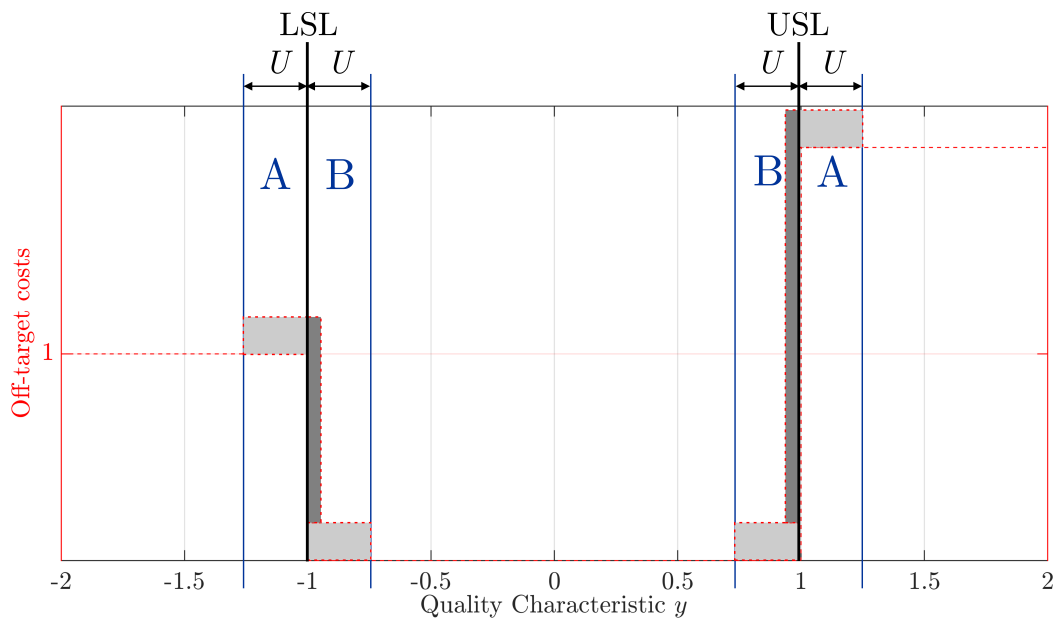


Figure 5.13: Asymmetric constant cost function (red, dashed) with uncertainty range of the measuring system (solid, blue). Light grey rectangles indicate additional cost for re-measuring with a more accurate system. Dark grey rectangles indicate the additional cost if re-measuring yields a result in the uncertainty range of the more accurate measuring system.

Alternatively, if a more accurate measurement system is to be used for results in the uncertainty range, the cost for such measurement is to be added in region A and B, as shown by light grey rectangles in figure 5.13. Clearly, also a more accurate system may yield results in its, relatively to the initially used system, smaller, uncertainty range. Assuming that parts with measurement results in this range are classified as defective, additional cost arise, as depicted by the dark rectangles in figure 5.13.

With the possibility of arbitrary cost functions, considering the measurement uncertainty is simplified, i.e. no specific evaluation models are necessary for different strategies.

5.4.4 A generalised stopping criterion for setup adjustment

If the cost to adjust a process are non-zero, continuous adjustment of a process may not yield the most economical solution. Thus, a rule when to adjust is necessary.

To minimise off-target cost for short production runs (i.e. small batch sizes), the use of deadband models was proposed [9, 72, 80, 81, 167]. The idea is to adjust a process only if the process setpoint is substantially off target [80]. To quantify "substantially off target", adjustment limits are calculated. If the current estimate of the process setpoint is outside the limits, the process is to be adjusted. The resulting adjustment limits are time varying and have a characteristic shape for short production runs. Those limits are discussed in more detail in section 5.4.4.

Besides reports about the use of deadband models in SA, Trietsch proposed a stopping criterion for normally distributed process variation and quadratic cost function, based on Grubbs' harmonic rule as [26]

$$n_f = \frac{\sqrt{\left(\frac{C_{ma}}{c^q \sigma_v^2} - 1\right)^2 + \frac{4NC_{ma}}{C^q \sigma_v^2} + \frac{C_{ma}}{c^q \sigma_v^2} - 1}}{\frac{2C_{ma}}{c^q \sigma_v^2}}. \quad (5.21)$$

Where N is the number of parts in the batch, the constant cost to measure a part and adjust the process are denoted by C_{ma} . The resulting n_f is the maximal number of produced parts after which the process adjustment is to be stopped. Since equation 5.21 yields a non-integer value and the production is discrete, truncate as $n = \lfloor n_f \rfloor$ to find the number of parts to produce before stopping the adjustment.

The derivation of equation 5.21 is motivated by the following idea: adjust the process until an adjustment reduces the Expected Quadratic Loss (EQL, Trietsch used a quadratic cost model) for the rest of the production by less than the cost to adjust the process. Alternatively, expressed vice versa: stop if an adjustment is more costly than leaving the process unchanged. This can be formalised as: measure and adjust as long as [26]

$$C_{ma} < c^q \sigma_v^2 \frac{N-i}{i-1} - c^q \sigma_v^2 \frac{N-i}{i}. \quad (5.22)$$

The largest i that satisfies this inequality equals to n of the truncated result of equation 5.21 [26]. It can be seen, that the cost for being off-target at part $i-1$ and part i is modelled by $\frac{c^q \sigma_v^2}{i-1}$ and $\frac{c^q \sigma_v^2}{i}$, respectively.

Using expected cost instead of expected quadratic loss, a more general formulation is proposed by the author: measure and adjust as long as

$$C_{ma} < \mathbb{E}[c(Y_{i-1}|U_{i-2} = U_{i-2}^*)](N - i) - \mathbb{E}[c(Y_i|U_{i-1} = U_{i-1}^*)](N - i) \quad (5.23)$$

holds, where $\mathbb{E}[c(Y_i|U_{i-1} = U_{i-1}^*)]$ is the expected cost at the i th part with performed optimal adjustment after part $i - 1$.

Since $U_{i-1} = U_{i-1}^*$, the predictive quality characteristic density (equation 5.9) at $i - 1$ is $Y_i|U_{i-1} = U_{i-1}^* \sim N(\mu_i^*, \sigma_\nu^2 + \tau_{i-1}^2)$. Note that all involved quantities are computable offline, i.e. before the production process starts. Thus, the above criterion is termed Static Stopping Criterion (SSC). A variant that takes the current estimate of the process setpoint into account is discussed in the next sections.

Computer implementation and validation

Inequality 5.23 was implemented in a computer program that finds the minimal i that satisfies the inequality, i.e. n . Note that the expected cost in equation 5.23 are computed numerically as discussed in section 5.4.3.

The resulting n from the implementation was compared to the closed form solution (equation 5.21), inevitably with a symmetric quadratic cost function ($c_1^q = c_2^q = 5000$) and a normally distributed process variation. Results given in figure 5.14 show the number of adjustments n for different batch sizes N and three different values of σ_ν , evaluated by both methods. Clearly, the results are identical. In almost all performed experiments, numerical inaccuracies are removed by the truncation operation. However, differences of ± 1 may occur if the result before truncation is near an integer due to different numerical operations involved.

By the use of the proposed method to calculate expected cost, this approach is applicable for other cost functions and process variation models, as it will be demonstrated in section 5.4.5.

Deadband adjustment models and a dynamic stopping criterion

As briefly discussed in chapter 2, deadband models [72, 79–81] provide a temporally varying deadband. If the current estimate of the process setpoint, μ_i , is outside this band, the process is to be adjusted. If it is inside the band, an adjustment is not feasible since cost for adjustment are higher than the cost due to the non-optimal process setpoint. Although

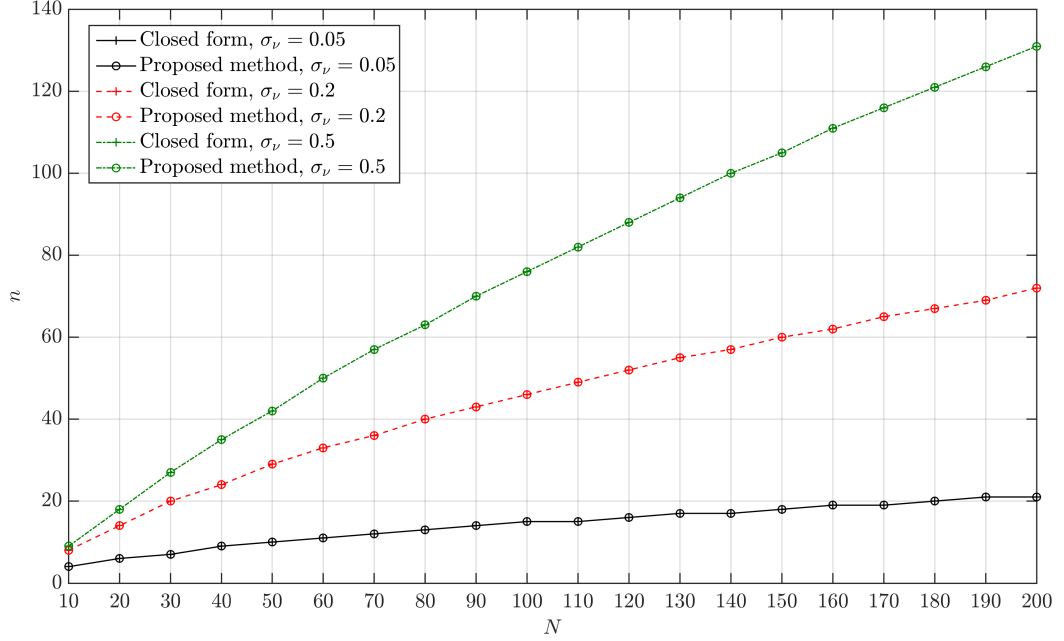


Figure 5.14: Number of adjustments to be made n vs. batch size N for three different σ_ν , evaluated by equation 5.21 and equation 5.23.

such models optimise cost by leaving out adjustments, they do not limit the number of adjustments and hence do not provide a stopping criterion.

Consider the optimal adjustment rule for a deadband model, e.g. from Lian & Castillo [72]. The model requires a symmetric quadratic cost function ($\mu_i^* = 0$) and normally distributed process variation. The adjustment rule for a known process variation σ_ν is given as [72]

$$U_{i-1}^* = \begin{cases} -\mu_{i-1} & \text{if } \mu_{i-1}^2 + \mathbf{E}[R_i(\mu_i)|U_{i-1} = 0] > C_a + \mathbf{E}[R_i(\mu_i)|U_{i-1} = -\mu_{i-1}] \\ 0 & \text{otherwise.} \end{cases} \quad (5.24)$$

$R_i(\mu_i)$ denotes the minimum cost due to being off-target *for all* parts ($i+1$) to N and C_a represents the cost to adjust the process. Note that, due to symmetry of the process variation and cost function, the optimal process mean is $\mu_i^* = 0 \forall i \in [1, N]$ and does not show up in the rule. Cost for measurement do not show up in this model because measurements are always necessary to check for violation of the limits, regardless of the adjustments to be made. Based on this rule, deadband limits are calculated, i.e. the limit is at the value of the

current process setpoint estimate μ_i for which both sides are equal. The notation from Lian & Castillo [72] was slightly adapted for better clarity.

Retaining the above representation, it can be seen that an adjustment is made if: the quadratic cost, μ_{i-1}^2 , at $i - 1$ due to non-adjustment plus expected minimum cost *without* adjustment at $i - 1$ for the remainder of the batch is larger than the cost for adjustment C_a plus expected minimum cost *with* adjustment at $i - 1$ for the remainder of the batch.

The expected minimum cost for the rest of the batch, given U_{i-1} , are [72]

$$\mathbb{E}[R_i(\mu_i) | U_{i-1}] = \int R_i(\mu_i) f_N(y_i; \mu_{i-1} + U_{i-1}, \sigma_\nu^2 + \tau_{i-1}^2) dy_{i+1} \quad (5.25)$$

and the minimum cost for the rest of the batch, $R_i(\mu_i)$, is defined as [72]

$$R_{i-1}(\mu_{i-1}) = \min_{U_{i-1}} \{ \sigma_\nu^2 + \tau_{i-1}^2 + (\mu_{i-1} + U_{i-1})^2 + c\delta(U_{i-1}) + \mathbb{E}[R_i(u_i) | U_{i-1}] \}, \quad (5.26)$$

where $\delta(x) = 1$ if $x \neq 0$ and $\delta(x) = 0$ otherwise. It can be seen that all possible future adjustments U and process variation variances τ^2 are taken into account. In their implementation, optimal U_i 's are found by backwards induction [72].

Note that deadband models allow to leave out adjustments, i.e. $U_{i-1} = 0$ to leave out an adjustment, to minimise cost whereas a stopping criterion shall evaluate when to stop adjustments, i.e. $U_{i-1} = 0 \forall (i - 1) > n$. By these considerations, a stopping criterion that takes the current process setpoint into account is proposed by the author: measure and adjust as long as

$$\mathbb{E}[c(Y_{i-1} | U_{i-1} = 0)](N - i) > C_a + \mathbb{E}[c(Y_{i-1} | U_{i-1} = U_{i-1}^*)](N - i) \quad (5.27)$$

holds. Similarly to above, the largest i that satisfies equation 5.27, equals to the number of parts to produce before adjustment is to be stopped, i.e. n . This dynamic variant of the stopping criterion is termed Dynamic Stopping Criterion (*DSC*).

Note that inequality 5.24 and inequality 5.27 are not equivalent. The deadband model requires measurements during the entire process, allowing to consider more precise process setpoint estimations and future adjustments. In contrast, with the proposed model, only the current estimates are used and measurements may stop at after n produced parts.

Performance comparison to a deadband adjustment model

For comparing the performance among models, the Integrated Real Cost (IRC)

$$IRC = \sum_{i=1}^N \left(E[c(Y_i|\theta_i^R)] + C_a \delta(U_i) \right) + mC_m \tag{5.28}$$

is proposed. The real process setpoint θ_i^R , which is a scalar value and not a random variable, is available in simulation. Clearly, this value is in practice unknown but serves well for model comparison purposes. Thus, the expected cost can be given with the real process setpoint known, i.e. $E[c(Y_i|\theta_i^R)]$. Cost for adjustment C_a are added if an adjustment U_i was made, $\delta(x) = 1$ if $x \neq 0$ and $\delta(x) = 0$ otherwise. The number of measurements m times the cost for measurement C_m is included explicitly.

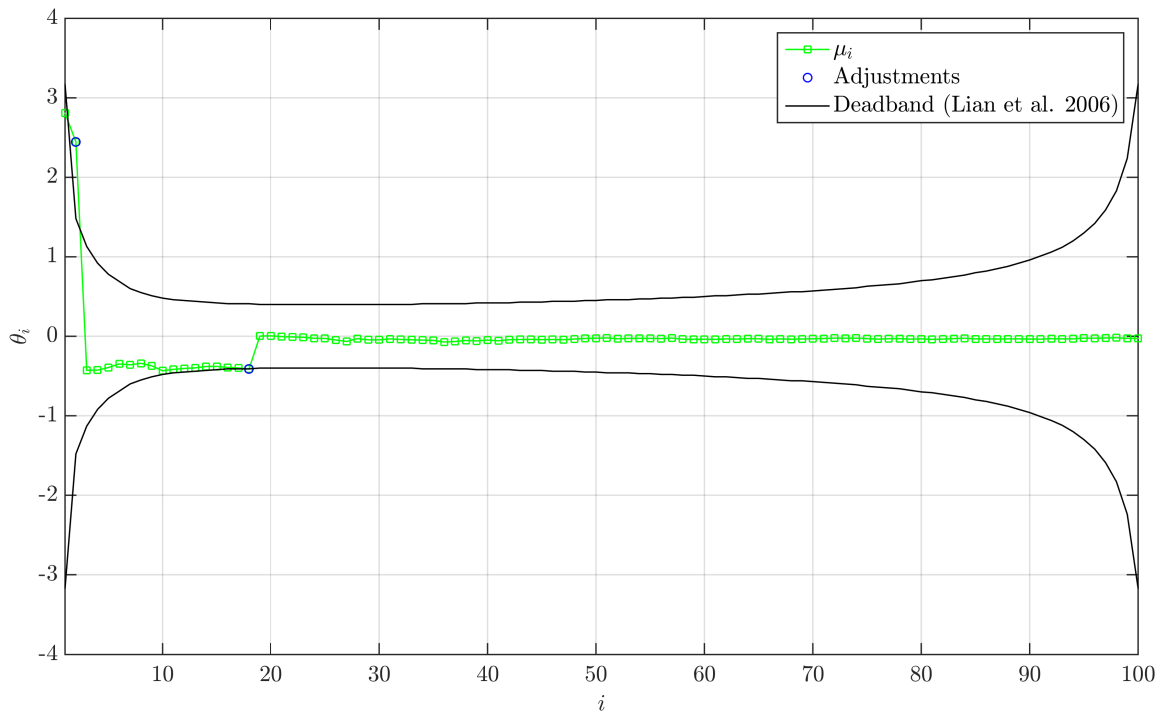


Figure 5.15: One production realisation with symmetric quadratic cost function ($c_1^q = c_2^q = 1000$) and normally distributed process variation ($\sigma_\nu = 0.4$ mm), adjusted by the above presented model from Lian & Castillo [72]. In addition, the deadband (black solid lines), calculated as in [72], and adjustments (blue circles) are shown.

Since deadband models allow to leave out adjustments, and not only to stop adjustments from a certain instant on, they obtain lower cost than a stopping criterion by design – if

measurement costs are excluded. Both approaches minimise off-target cost during the adjustment process, however deadband models exhibit more degrees of freedom to do so. On the other hand, it is not necessary to continue measurements after the n th part with a stopping criterion, whereas if a deadband model is employed, measurements must be performed during the complete batch, in order to test for violation of the deadband limits.

With deadband models, wider band limits in the beginning arise from limited knowledge of the process setpoint θ_i at the start of the process (figure 5.15). As a result, adjustments based on a highly uncertain θ_i must have a larger impact to be profitable. Later in the process, where the knowledge of the process setpoint is more precise, limits narrow. At the end of the process, limits funnel out again due to limited benefit by an adjustment, i.e. it affects only the few parts left to be produced. Note that a reduction of adjustment cost C_a narrows the deadband, i.e. cheaper adjustments justify more adjustments to be made.

If the assumption of a setup dominant process holds, i.e. constant mean of the quality characteristic during one batch, only changed by adjustments, the funnelling out of deadband models is in theory redundant. The increasingly precise estimated process setpoint θ_i shifts only if process adjustments $U_i \neq 0$ are made. However, due to process variation, the estimation of the process setpoint fluctuates. With this in mind, a comparison between the two approaches was conducted by the author.

Therefore, simulations with $N = 50$ and a real initial process setpoint (in practice unknown or only partly known) of $\theta_0^R = 2$ and a non-informative prior were performed. A normal process variation with different values for σ_v and different ratios of adjustment cost and quadratic cost coefficient C_a/c^q were used. Unfortunately, there exists no deadband model that allows for asymmetric cost functions [73], which is why a symmetric quadratic cost function was utilised with $c^q = 1$. The deadband limits were computed by a software implementation from the author, based on the R implementation from Lian et al. [73]. The ported software was verified by comparison of resulting deadband limits for the shown parameter sets.

To evaluate the relation between models, the ratio of the expected IRC is used, i.e.

$$\frac{E[IRC_{SSC}]}{E[IRC_{DB}]}, \quad (5.29)$$

where IRC_{SSC} and IRC_{DB} are the IRC obtained by the proposed static stopping criterion and the deadband model, respectively. The relation between the dynamic stopping criterion DSC and the deadband model is made analogously.

This ratio is approximated by the jackknife estimator. 99.7% confidence intervals, i.e. bootstrap-t jackknife intervals, were computed by the bootstrap-t algorithm[176], using the variant for independent simulations for IRC_{SSC} and IRC_{DB} . A data based method to compute confidence intervals was chosen since the sampled distribution of the ratio differed between the evaluated cases. Moreover, it accounts for asymmetric distributions of the ratio, which were observed in some cases.

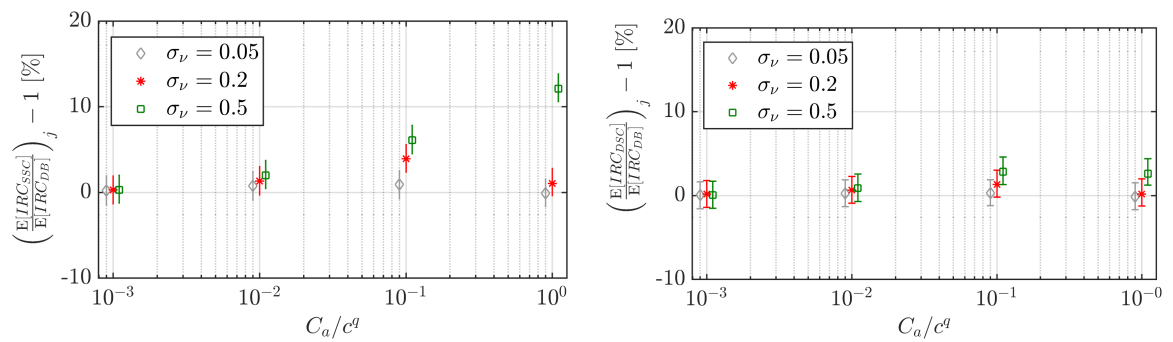


Figure 5.16: Increase of IRC , due to the use a stopping criterion instead of the deadband model, in percent. Measurement costs are not included. Evaluated by 1000 simulation repetitions. Vertical bars represent the 99.7% confidence bounds. A horizontal displacement between datasets was introduced at the 10^x marks for better clarity. Left: ratio for the static stopping criterion, SSC . Right: ratio for the dynamic stopping criterion DSC .

The increase in IRC in percent, with measurement costs excluded, i.e. $C_m = 0$, is given in figure 5.16. Results for the SSC vs. the deadband model span from approx. -1.5% to 14% increased IRC if the SSC is used. It is evident that smaller ratios C_a/c^q lead to lower discrepancies between the two approaches. Especially for high process variation, the effect is evident. For the DSC , the resulting increase in IRC is between approx. -1.7% and 4.5% .

The proposed stopping criteria yield, by design, higher cost than the deadband model compared with, if measurement costs are excluded. However, the stopping criteria are simpler for practical use since only one single transition between "do adjust" and "do not adjust" is made, whereas with deadband models, operators have to monitor the production process from beginning to the end for potential need to adjust. The example indicates that, if measurements are done regardless of the adjustment process, the proposed criteria, especially the DSC , could replace a deadband model. Application of the DSC increases the IRC by less than 5% in the demonstrated cases, what can be acceptable in favour of a simpler rule.

5.4. FORGING PROCESS ADJUSTMENT

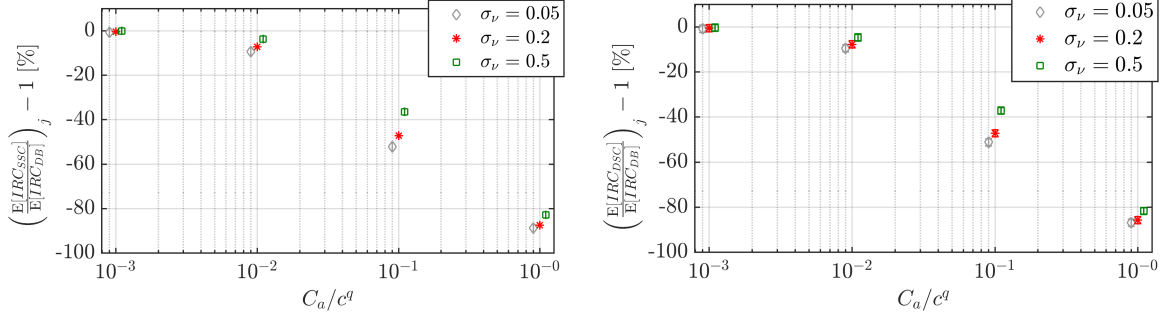


Figure 5.17: Increase of IRC , due to the use a stopping criterion instead of the deadband model, in percent. Measurement costs equal to the cost for adjustment. Evaluated by 1000 simulation repetitions. Vertical bars represent the 99.7% confidence bounds. A horizontal displacement between datasets was introduced at the 10^x marks for better clarity. Left: ratio for the static stopping criterion, SSC . Right: ratio for the dynamic stopping criterion DSC .

If measurement costs are included, however, and measurements are performed only for the adjustment procedure, the number of necessary measurements in the deadband model still equals the batch size, i.e. $m = N$ in equation 5.28. In contrast, for the stopping criterion, it equals to the last adjustment to be made, i.e. $m = n$. In figure 5.17, results with $C_m = C_a$ are presented. Here, results range from approx. 2% down to -86% for the SSC and from approx. 1.5% down to -90% for the DSC . Thus, both criteria approximately equal or outrun the deadband model, depending mainly on the ratio C_a/c^q .

5.4.5 Coupled process adjustment

In this section, previously discusses methods are joined into a holistic framework for process adjustment. The flowchart of the proposed framework is shown in figure 5.18.

Before the production process starts (figure 5.18, top), the optimal process setpoints during adjustment $\{\hat{\mu}_i^*\}$ are estimated as described in section 5.4.3, given an appropriate cost function $c(y)$ and process variation ν . Note that, depending on the actual quality characteristic estimation model, a priori knowledge of the process variation may not be necessary [72, 73].

The gain a is to be approximated, e.g. by the discussed DOE approach (section 5.3.1). The prior distribution, $\theta_0 \sim N(\mu_0, \tau_0^2)$ is also to be found by the created response surface, i.e. μ_0 is the best a priori known process setpoint. For τ_0^2 , an appropriate uncertainty value, chosen on basis of simulation accuracy and the ability to set the process setpoint to a specific value is to be used.

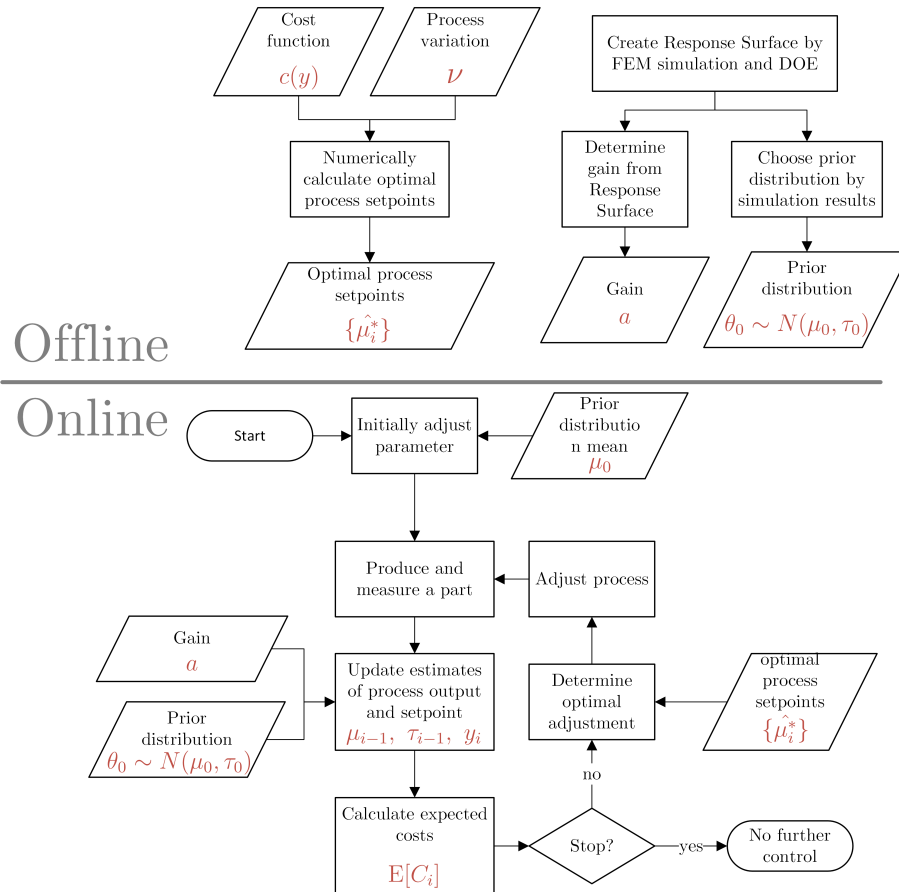


Figure 5.18: Flowchart of the coupled approach. Top: offline process steps. Bottom: online adjustment procedure.

The sequence for adjustment (figure 5.18, bottom) starts with initial (approximate) process setpoint setting followed by producing the first part and quantifying quality characteristics of interest through measurements. By incorporating the gain factor a in an appropriate estimation model, e.g. the model by Lian & Castillo [72] (section 5.4.3), an estimation of the quality characteristic can be made. Based on this estimation and the cost function, the expected cost are numerically calculated as described in section 5.4.3. With the expected cost available, the decision about continuing adjustments is made by the *SSC* or *DSC*, as proposed in section 5.4.4. If adjustments shall be continued, the optimal adjustment U_i^* is determined, the process is adjusted by that value and the sequence repeats.

In the following, the effect on this framework due to deviations of a , are analysed by computer simulations. Moreover, process adjustment for turbine blade forging is simulated with regard to the performance of different adjustment rules.

Influence of the process gain

As mentioned in section 5.4.3, the SA model assumes a multiplicative identity relation between process setpoint and adjustment, or in a slightly extended case, a linear relation. It was shown by calibrated FEM computer experiments (section 5.3.1) that the correlation is non-identity. In fact, for the Tresca factor, it is not even a linear relation. Note, however, that an initial process setpoint θ_0 , in the vicinity of the optimum, can be obtained by offline optimisation and the effective region of the response surface, where process adjustment "takes place", is small compared to the region of the shown response surface (figure 5.4). Thus, at small scale, a linear relationship is assumed.

To assess the effects of violating this assumption, simulations have been conducted by the author. To exclude the influence of the number of adjustments made to the process, it was always adjusted. Further, the real process setpoint θ_i^R is considered, instead of off-target cost, to exclude the dependence on a cost function. Therefore, define the Integrated Absolute Setpoint Deviation (*IASD*) as

$$IASD = \frac{1}{N} \sum_{i=1}^{i=N} |\theta_i^R|. \quad (5.30)$$

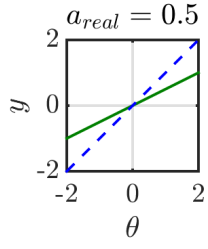
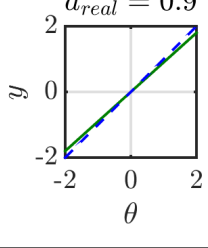
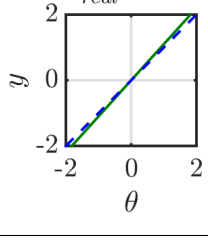
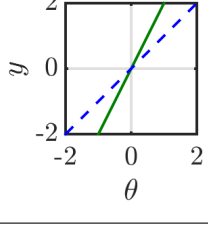
For simulation, two potentially different gain values were used. One for the simulated production process, a_{real} , and one for the adjustment model, a_{model} . The gain for the adjustment model was set to $a_{model} = 1$ for all simulations. The real gain of the process a_{real} was set to 0.5 and 2 to simulate severe deviations and to 0.9 and 1.1 to assess minor deviations.

For a relative comparison, the ratio $\frac{E[IASD|a_{real}]}{E[IASD|a_{real}=1]}$ is used. As in section 5.4.4, this ratio is approximated by the jackknife estimator and 99.7% confidence intervals are bootstrap-t jackknife intervals, calculated for independent simulations [176].

Table 5.1 shows this ratio for adjustments by the discussed model from Lian & Castillo [72], symmetric cost function, i.e. $\mu_i^* = 0 \quad \forall i \in [1, N]$, a non-informative prior, and normally distributed process variation, obtained by 1000 simulation repetitions. For θ_0^R , the values 2 and 10 were used to simulate a more or less severe initial process setpoint deviation. With the specification limits of -1 and 1 in mind, standard deviations of 0.05, 0.2 and 0.5 were selected for the process variation.

CHAPTER 5. PRODUCTION PROCESS OPTIMISATION

Table 5.1: Influence of gain factor a_{real} (solid line) with utilised gain factor $a_{model} = 1$ (dashed line), 99.7 % confidence intervals included. Results for $N = 50$, obtained by 1000 simulation repetitions.

a_{real}	θ_0^R	σ_ν	$\left(\frac{E[IASD a_{real}]}{E[IASD a_{real}=1]} \right)_j - 1 [\%]$
	2	0.05	217.2 ^{+1.9} _{-1.4} %
		0.2	98.4 ^{+2.0} _{-1.2} %
		0.5	24.1 ^{+2.2} _{-1.2} %
	10	0.05	278.9 ^{+1.6} _{-1.5} %
		0.2	231.2 ^{+1.8} _{-1.4} %
		0.5	164.4 ^{+2.0} _{-1.2} %
	2	0.05	13.9 ^{+1.8} _{-1.5} %
		0.2	-1.9 ^{+2.2} _{-1.2} %
		0.5	-1.0 ^{+2.5} _{-1.1} %
	10	0.05	32.9 ^{+1.7} _{-1.6} %
		0.2	18.5 ^{+1.7} _{-1.4} %
		0.5	4.2 ^{+2.0} _{-1.3} %
	2	0.05	26.2 ^{+1.8} _{-1.4} %
		0.2	9.4 ^{+2.2} _{-1.2} %
		0.5	6.7 ^{+2.7} _{-1.0} %
	10	0.05	43.3 ^{+1.6} _{-1.6} %
		0.2	28.3 ^{+1.7} _{-1.4} %
		0.5	16.5 ^{+2.0} _{-1.3} %
	2	0.05	241.2 ^{+1.9} _{-1.3} %
		0.2	154.5 ^{+2.5} _{-1.1} %
		0.5	96.1 ^{+3.2} _{-0.9} %
	10	0.05	286.1 ^{+1.6} _{-1.5} %
		0.2	251.2 ^{+1.9} _{-1.4} %
		0.5	201.1 ^{+2.2} _{-1.2} %

From these results it can be concluded that over- and underestimations of a by 10% results in increases the $IASD$ between approx. -5% and 45% . A severely wrong estimation

of a by factor 2 increases the $IASD$ up to approx. 288%. It is interesting to note that for the specific parameters, $a_{real} = 0.9$, $\theta_0 = 2$ and $\sigma_\nu = 0.5$, a lower $IASD$ than in the ideal case is observed. In the evaluated cases, overestimation of a causes less increase in the $IASD$ than underestimating a . This can be explained by the respective process behaviour.

In figure 5.19, it can be observed that underestimation leads to slow convergence whereas overestimation causes an overshooting in the beginning but converges faster to the optimal process setpoint. This indicates that, for an uncertain gain, a slight overestimation can be advantageous. However, this depends on the utilised cost function.

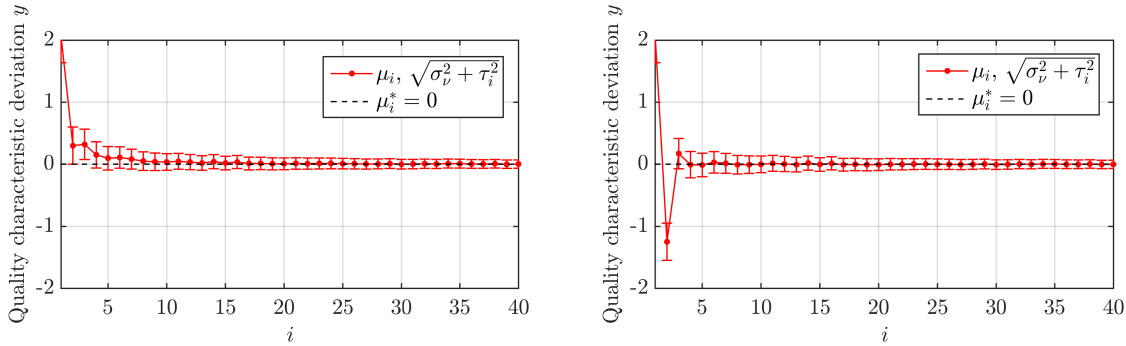


Figure 5.19: One realisation for $a_{model} = 1$, $\theta_0^R = 2$ and $N = 20$, always adjusted. Error bars represent the standard deviation of Y_i . Left: $a_{real} = 2$, underestimation. Right: $a_{real} = 0.5$, overestimation.

Adjustment comparison

To emulate the adjustment for turbine blade forging, a model of constant and quadratic off-target cost is proposed (figure 5.20).

As discussed above, the maximal thickness quality characteristic, as well as other considered quality characteristics, exhibits strong asymmetry in terms of cost, i.e. negative thickness deviations cause higher cost than positive deviations. By this model, any negative deviation is penalised by the constant cost spent to scrap the workpiece. Positive deviations are modelled by a quadratic cost function that reach the same cost if they are two units off.

Note that the measurement uncertainty is not explicitly considered in this cost model because no secondary measuring system would be available if results fall in the uncertainty range. The chosen tolerance is exemplary and does not reflect a specific real case. Thus, accounting for measurement uncertainty would shift the lower limit and thereby merely change the tolerance limits. Also note that such an uncertainty range exists only at the lower specification limit, whereas for positive deviations, no decision has to be taken but machining costs will increase (chapter 1).

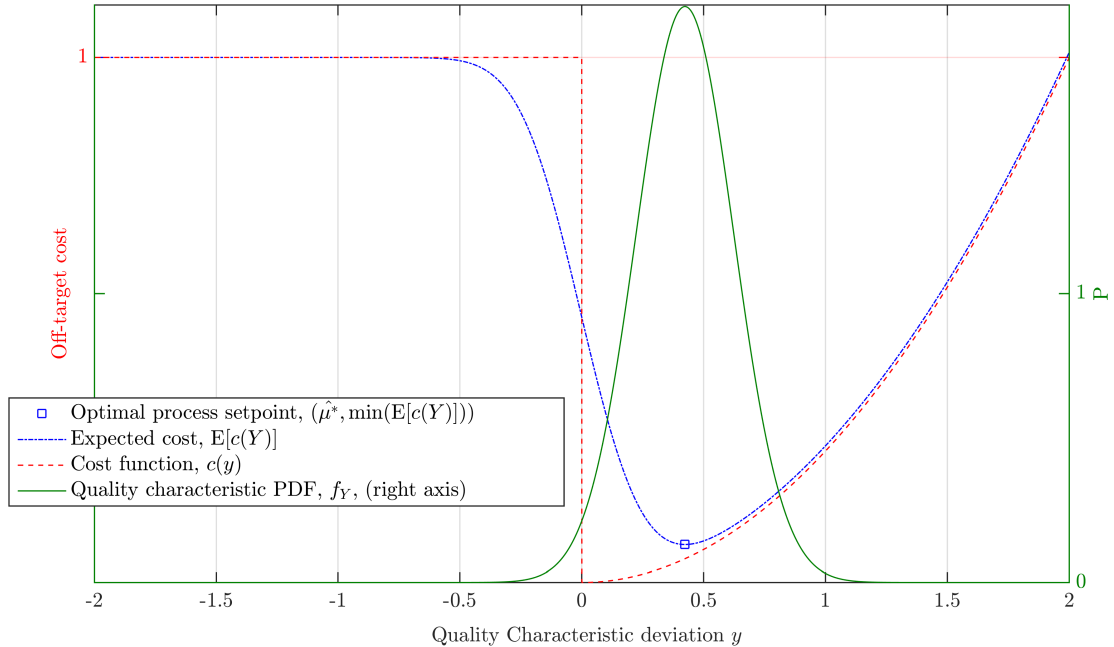


Figure 5.20: Normally distributed process variation (green solid line) and expected cost $E[y]$ (blue dash-dotted line) and the proposed cost function (red dashed line).

Further parameters are $N = 50$ and $C_a = 0.01$. N was chosen to reflect typical batch sizes and C_a was assumed such that an adjustment is 100 times cheaper than scrapping a workpiece. The same cost are again used for measurement, i.e. $C_m = C_a$. A normal process variation with standard deviation σ_v equal to 0.05, 0.2 and 0.5 was used. The tolerance range spans from 0 to +2 and for the initial process setpoint θ_0^R , positive values 1 and 4, i.e. on the "safe side" of the cost function, are used. Note that these parameters are chosen to demonstrate the adjustment process exemplary; application specific cost and quality distributions are required for a real implementation. Also note that the deadband model ([72], section 5.4.3) is designed for symmetric quadratic off-target cost. Due to lack of a deadband model that allows for asymmetric cost functions [73], no such model is included in the comparison.

An "One adjustment" rule was included that performs one optimal adjustment after the first workpiece is produced and measured. Thereby, it emulates an "educated manual adjustment" by an operator. This first and only adjustment is made on basis of the deadband model rule. This is feasible, since the real initial process setpoint is in the quadratic region of the cost function. In addition, a naive rule, i.e. "Always adjust", is included. For both

rules, the adjustment magnitude is found by considering the current process mean, as with the *DSC*.

Table 5.2 shows the sampled mean *IRC* (equation 5.28) including 99.7 % bootstrap confidence intervals, obtained by 1000 simulation runs. A data based method to compute confidence intervals was chosen since the sampled distribution of the *IRC* differed between the displayed adjustment rules. Additionally, the sampled mean of the number of adjustments $\#adj$ is shown. Two cases are given, for an informative ($\theta_0 \sim N(1, 0.5)$) and non-informative prior ($\theta_0 \sim N(0, \infty)$). The variance of the non-informative prior was approximated by the value 10 000 for numerical simulation. Note that $\theta_0^R = 1$ represents the case where the initial process setpoint corresponds to the informative prior mean and $\theta_0^R = 4$ constitutes an erroneous informative prior. The latter is indicated by red font in table 5.2.

It can be observed that the *DSC* achieves the lowest *IRC* in all cases with a correct informative prior or non-informative prior, followed by the *SSC*. The latter shows the best results if a precise but wrong prior is used. Note that the *SSC* does not take the current process setpoint into account and is therefore not influenced by the prior, in contrast to the *DSC*.

If the process variation increases, the "Always adjust" rule and the stopping criteria yield more similar results, e.g. for $\sigma_\nu = 0.5$, because both stopping criteria perform an increased number of adjustments for high process variation. Moreover, it can be seen that the "One adjustment" rule yields the widest confidence intervals. Thus, it can be concluded that an adequate stopping criterion is more favourable than simple adjustment rules for the selected parameters, with the highest profit for low process variation.

It shall be emphasised that the *SSC* is computable offline, i.e. before the production process starts, and simply yields the number of adjustments for given parameters what makes it a very practical tool. On the other hand, the *DSC* yields slightly lower cost while requiring to take the decision, after which part to stop, during the production process.

CHAPTER 5. PRODUCTION PROCESS OPTIMISATION

Table 5.2: Mean IRC and mean number of adjustments, calculated by 1000 simulation repetitions using $N = 50$ and $C_a = C_m = 0.01$. 99.7% confidence intervals included. Results for the erroneously informative prior are highlighted in red font, lowest values are highlighted in bold font.

θ_0^R	σ_ν	Adj. rule	$\overline{IRC} (\overline{\#adj})$ $\theta_0 \sim N(1, 0.5)$		$\overline{IRC} (\overline{\#adj})$ $\theta_0 \sim N(0, 10\,000)$	
1	0.05	<i>SSC</i>	0.792 ^{+0.008} _{-0.010}	(5.0)	0.792 ^{+0.010} _{-0.010}	(5.0)
		<i>DSC</i>	0.765 ^{+0.005} _{-0.005}	(5.3)	0.764 ^{+0.005} _{-0.005}	(5.4)
		One adj.	1.038 ^{+0.090} _{-0.121}	(1.0)	1.013 ^{+0.089} _{-0.093}	(1.0)
		Always adj.	1.652 ^{+0.003} _{-0.004}	(50.0)	1.652 ^{+0.003} _{-0.003}	(50.0)
	0.2	<i>SSC</i>	4.365 ^{+0.027} _{-0.031}	(14.0)	4.365 ^{+0.028} _{-0.036}	(14.0)
		<i>DSC</i>	4.239 ^{+0.019} _{-0.016}	(12.2)	4.270 ^{+0.020} _{-0.028}	(12.4)
		One adj.	5.775 ^{+0.233} _{-0.298}	(1.0)	6.234 ^{+0.351} _{-0.454}	(1.0)
		Always adj.	5.001 ^{+0.017} _{-0.018}	(50.0)	5.016 ^{+0.017} _{-0.020}	(50.0)
	0.5	<i>SSC</i>	14.387 ^{+0.068} _{-0.060}	(21.0)	14.387 ^{+0.053} _{-0.054}	(21.0)
		<i>DSC</i>	14.029 ^{+0.035} _{-0.041}	(17.2)	14.260 ^{+0.058} _{-0.048}	(18.1)
		One adj.	15.104 ^{+0.232} _{-0.217}	(1.0)	19.973 ^{+0.749} _{-0.722}	(1.0)
		Always adj.	14.694 ^{+0.042} _{-0.044}	(50.0)	14.882 ^{+0.041} _{-0.049}	(50.0)
4	0.05	<i>SSC</i>	4.544 ^{+0.010} _{-0.011}	(5.0)	4.544 ^{+0.010} _{-0.012}	(5.0)
		<i>DSC</i>	4.518 ^{+0.004} _{-0.004}	(5.6)	4.518 ^{+0.005} _{-0.005}	(5.5)
		One adj.	4.700 ^{+0.040} _{-0.059}	(1.0)	4.767 ^{+0.095} _{-0.106}	(1.0)
		Always adj.	5.402 ^{+0.002} _{-0.002}	(50.0)	5.404 ^{+0.004} _{-0.004}	(50.0)
	0.2	<i>SSC</i>	8.128 ^{+0.025} _{-0.029}	(14.0)	8.128 ^{+0.029} _{-0.033}	(14.0)
		<i>DSC</i>	8.242 ^{+0.026} _{-0.028}	(12.7)	8.035 ^{+0.021} _{-0.023}	(12.4)
		One adj.	14.450 ^{+0.354} _{-0.383}	(1.0)	9.955 ^{+0.348} _{-0.355}	(1.0)
		Always adj.	8.969 ^{+0.024} _{-0.026}	(50.0)	8.770 ^{+0.016} _{-0.018}	(50.0)
	0.5	<i>SSC</i>	18.133 ^{+0.050} _{-0.073}	(21.0)	18.133 ^{+0.065} _{-0.065}	(21.0)
		<i>DSC</i>	20.564 ^{+0.112} _{-0.136}	(18.6)	18.002 ^{+0.046} _{-0.055}	(18.0)
		One adj.	65.371 ^{+1.195} _{-1.168}	(1.0)	23.375 ^{+0.662} _{-0.804}	(1.0)
		Always adj.	21.140 ^{+0.122} _{-0.128}	(50.0)	18.603 ^{+0.048} _{-0.059}	(50.0)

5.5 Conclusion

In this chapter, quality characteristics of turbine blades were discussed and the need for asymmetric cost functions in forging was emphasised. Parameters for online optimisation were identified and the forging process was characterised by calibrated FEM simulations and DOE methodology. The cooling process was modelled by an artificial neural network to predict evolution of quality characteristics during cooling. The resulting variability in the predictions was not appropriate for the considered application. Although, the author suspects that a more stable, e.g. actively controlled, cooling process can lead to more precise predictions.

In the context of process adjustment, a novel formulation to approximate the optimal process setpoint was proposed. The novel formulation allows for arbitrary off-target cost functions and process variation models. It was verified by comparison to state-of-the-art methods with resulting deviations in the order of 10^{-4} %. Based on this result, an available stopping criterion was generalised for arbitrary cost functions and arbitrary process variation models. The discussed criterion determines the optimal number of adjustments before the process starts, what makes it an easy to use tool. Feasibility was verified by comparison with the specific case, showing equivalent results up to numerical inaccuracies. Moreover, a stopping criterion based on a deadband model formulation was proposed. This dynamic criterion evaluates the optimal number of adjustments during production. However, it accounts for a prior belief of the process setpoint. Both criteria were compared to a state-of-the-art deadband model. If measurement costs are equal to adjustment costs and measurements are stopped after adjustment, the performance of both proposed criteria approximately equals or outruns the deadband model performance, yielding down to 90% lower cost in the simulated cases. The proposed criteria are not restricted to forging but are applicable to any setup dominant production processes.

Eventually, a holistic framework for process adjustment, based on the previously discussed methods was proposed. The necessity of a gain factor for the forging process was discussed and deviations of this factor were investigated. It was found that a slight overestimation of the gain factor could be preferable if it is uncertain, depending on the cost function. By simulation of the adjustment process for turbine blades, the proposed stopping criteria were compared to simpler adjustment rules, i.e. one educated adjustment and always adjusting. Unfortunately, no deadband model that allows for asymmetric cost functions is available to compare with. The dynamic stopping criterion resulted in the lowest cost in all simulated cases with a correct informative prior or non-informative prior, followed by the static stopping criterion.

CHAPTER 5. PRODUCTION PROCESS OPTIMISATION

Chapter 6

Conclusions

In this thesis, the quality control for forged freeform workpieces was discussed. The focus was on process-intermittent dimensional measurements at elevated temperature, e.g. on gas turbine blades, and forging process adjustment during the ramp-up of production batches. The following paragraphs summarise the main conclusions of this work and review the contributions of the author.

At the former, a fast heuristic surface reconstruction method to approximate the workpiece surface was presented. Its low asymptotic time complexity allows for realtime visualisation of the workpiece with sufficient framerate during the measurement process. Thus, it allows operators to monitor and qualitatively verify measurement results quickly. The approach is based on a heuristic state-of-the-art method and incorporates a fundamental idea for surface reconstruction. Improvement to the state-of-the-art method was demonstrated by example on a typical gas turbine blade geometry.

A 2D data fusion method was presented, based on the envelope method, which yields better results than simple averaging of data points in terms of shape preservation and averaging capabilities as shown by the example of a profile geometry. The method exhibits the same asymptotic time complexity as pointwise averaging and as a side product, it allows for detection of high measurement point dispersion and can thus support system diagnostics.

A 3D data registration method for multiple light sectioning sensors in combination with a linear motion system was proposed. The method quantifies the misalignment between sensors and an additional linear moving system by use of a surrogate setup, a conical artefact and a computer algorithm. The method was validated by simulations and real experiments that show a 5-times reduction of deviations between measurements of sensors with respect to an already optimised adjustment by manual methods.

CHAPTER 6. CONCLUSIONS

Influences on the coordinate measuring system were identified and quantified, mainly considering thermal effects and multisensor issues. It was found that thermal effects on the linear motion system and sensor misalignment are the two most dominant error sources. For both, adequate correction methods were proposed. For the former, online temperature measurement by three sensors and appropriate interpolation was proposed and for the latter, the discussed 3D data registration method is recommended.

By the availability of a coordinate measuring system that enables quantification of quality characteristics at elevated temperature, investigations on online control of the forging process became feasible. The focus was on process adjustment during ramp-up of small batch production on the example of turbine blade forging.

Firstly, quality characteristics of turbine blades were discussed and the need for asymmetric cost models in forging was emphasised. Then, parameters, adequate for online optimisation, were identified and the forging process was characterised by calibrated FEM simulations and DOE methodology.

Since the cooling process has significant impact on the geometry of the thin aerofoil region of turbine blades, its influence must be considered and was modelled by an artificial neural network to predict evolution of quality characteristics while cooling. Unfortunately, the resulting variability in the predictions was not appropriate for the considered application. However, the author suspects that a stabilised, e.g. actively controlled, cooling process can lead to predictions that are more precise.

For the aimed process adjustment, a novel formulation of expected off-target cost was proposed. The formulation enables approximation of the optimal process setpoint, during production and in steady state, for arbitrary off-target cost models and process variation models. It was verified by comparison to state-of-the-art closed-form methods with resulting deviations in the order of 10^{-4} %. However, numerical optimisation is necessary, which is feasible for the univariate case. The method is also applicable for the multivariate case, as demonstrated on a bivariate example, but more sophisticated numerical methodology becomes necessary.

The question, when to stop adjusting a production process during ramp-up could be answered from literature research, restricted to a specific combination of process variation and off-target cost model, though. By use of the proposed formulation of expected off-target cost, the available stopping criterion was generalised for arbitrary off-target cost functions and quality characteristic distributions. The discussed criterion determines the optimal number of adjustments before the process starts, what makes it an easy to use tool. Feasibility of the proposal was verified by comparison with the established specific case, showing equivalent results up to numerical inaccuracies.

Moreover, a stopping criterion based on a deadband model formulation was proposed. This dynamic criterion evaluates the optimal number of adjustments during production. However, it accounts for a prior belief of the process setpoint and yielded slightly better results in most simulations. Both criteria were compared to a more complex state-of-the-art deadband model for process adjustment. For the dynamic criterion, it was found that the average cost increase by less than 5% for the evaluated typical cases. This can be acceptable in the favour of a simpler adjustment rule.

However, with the proposed stopping criteria, it is not necessary to measure during the entire production process, but only up to the moment when no more adjustments are necessary. Deadband models in contrast, require measurements during the entire process. By incorporating cost for measurements, equal to the cost for adjustment, it was demonstrated that the performance of both stopping criteria approximately equals or outruns the deadband model performance, yielding down to 90% lower cost in the simulated cases for small batch production. It shall be emphasised that the proposed criteria are not restricted to forging or hot working but are applicable to any setup dominant production processes.

Eventually, a holistic framework for process adjustment, based on previously discussed offline and online methodologies. In this context, the necessity of a gain factor in the process model was discussed. The necessity of a gain factor for the forging process was discussed and deviations of this factor were investigated. It was found that a slight over-estimation of the gain factor could be preferable if it is uncertain, depending on the cost function.

Using the introduced framework, the adjustment process for turbine blades was emulated. In this context, the proposed stopping criteria were compared to simpler adjustment rules. Unfortunately, no state-of-the-art deadband model exists that allows for asymmetric off-target cost functions, which is why it was excluded from the comparison. It was shown that the dynamic stopping criterion yields the lowest average cost for all simulated instances, followed by the static stopping criterion. Thus, it can be stated that an adequate stopping criterion is more favourable than simple adjustment rules for the selected parameters, with the highest profit for low process variation.

CHAPTER 6. CONCLUSIONS

References

- [1] Douglas C. Montgomery. *Introduction to statistical quality control*. 7th ed. Hoboken, NJ: Wiley, 2013. ISBN: 978-1118146811.
- [2] JCGM 200:2012. *International Vocabulary of Metrology (VIM) – Basic and General Concepts and Associated Terms, 3rd edition: Basic and general concepts and associated terms*. Bureau international des poids et mesures, Sèvres, 2012.
- [3] Albert Weckenmann. *Koordinatenmesstechnik: Flexible Strategien für funktions- und fertigungsgerechtes Prüfen. 2., vollständig überarb. Aufl.* München: Hanser, 2012. ISBN: 978-3-446-40739-8.
- [4] Enrico Savio, Leonardo De Chiffre, and Robert Schmitt. “Metrology of freeform shaped parts”. In: *CIRP Annals - Manufacturing Technology* 56 (2) (2007), pp. 810–835.
- [5] ISO 17450-1:2011. *Geometrical product specifications (GPS) - General concepts - Part 1: Model for geometrical specification and verification*. International Organization for Standardization, Geneva, 2011.
- [6] DIN 58174. *Optics and photonics - Specification of freeform surfaces*. German Institute for Standardization, Berlin, 2011.
- [7] X. Jiang, P. J. Scott, and David J. Whitehouse. “Freeform Surface Characterisation - A Fresh Strategy”. In: *CIRP Annals - Manufacturing Technology* 56 (1) (2007), pp. 553–556.
- [8] Vijay Kumar Butte and L. C. Tang. “Engineering Process Control: A Review”. In: *Handbook of Performability Engineering*. Ed. by Krishna B. Misra. Springer London, 2008, pp. 203–223. ISBN: 978-1-84800-130-5.
- [9] Enrique Del Castillo. “Statistical process adjustment: a brief retrospective, current status, and some opportunities for further work”. In: *Statistica Neerlandica* 60 (3) (2006), pp. 309–326.

CHAPTER 6. REFERENCES

- [10] Claus P. Keferstein. *Fertigungsmesstechnik: praxisorientierte Grundlagen, moderne Messverfahren*. 8. Auflage. Wiesbaden: Vieweg + Teubner, 2015. ISBN: 978-3-8348-2582-7.
- [11] Enrico Savio. “A methodology for the quantification of value-adding by manufacturing metrology”. In: *CIRP Annals - Manufacturing Technology* 61 (1) (2012), pp. 503–506.
- [12] H. Kunzmann et al. “Productive Metrology - Adding Value to Manufacture”. In: *CIRP Annals - Manufacturing Technology* 54 (2) (2005), pp. 155–168.
- [13] Robert J. Hocken and Paulo H. Pereira. *Coordinate measuring machines and systems*. 2nd ed. Vol. 76. Manufacturing engineering and materials processing. Boca Raton, Fla.: CRC Press, 2012. ISBN: 978-1574446524.
- [14] PIETRO ROSA TBM srl. *Pietro Rosa TBM srl*. 2014. URL: <http://www.pietrorosatbm.it/> (visited on 01/26/2014).
- [15] Stefania Bruschi and Andrea Ghiotti. “Distortions induced in turbine blades by hot forging and cooling”. In: *International Journal of Machine Tools and Manufacture* 48 (7-8) (2008), pp. 761–767.
- [16] Enrico Simonetto et al. “Analysis of X20Cr13 turbine blades distortions at elevated temperatures”. In: *AITeM*. 2015.
- [17] Enrico Simonetto et al. “Prediction of Distortions in Hot Forged Martensitic Stainless Steel Turbine Blades by Numerical Simulation”. In: *Procedia Manufacturing* 1 (2015), pp. 804–813.
- [18] Andrea Ghiotti et al. “Enhancing the accuracy of high-speed laser triangulation measurement of freeform parts at elevated temperature”. In: *CIRP Annals - Manufacturing Technology* 64 (1) (2015), pp. 499–502.
- [19] Zhisong Tian et al. “Dimension measurement of hot large forgings with a novel time-of-flight system”. In: *The International Journal of Advanced Manufacturing Technology* 44 (1-2) (2009), pp. 125–132.
- [20] Xian Lu and Raj Balendra. “Temperature-related errors on aerofoil section of turbine blade”. In: *Journal of Materials Processing Technology* 115 (2) (2001), pp. 240–244.
- [21] Hengan Ou and C.G. Armstrong. “Evaluating the effect of press and die elasticity in forging of aerofoil sections using finite element simulation”. In: *Finite Elements in Analysis and Design* 42 (10) (2006), pp. 856–867.

-
- [22] Bin Lu et al. “3D die shape optimisation for net-shape forging of aerofoil blades”. In: *Materials & Design* 30 (7) (2009), pp. 2490–2500.
- [23] Hengan Ou et al. “Development of a virtual die shape optimisation system for net-shape forging of aeroengine components”. In: *Steel Res Int* 79 (2) (2008), pp. 804–811.
- [24] Hengan Ou et al. “Finite element modelling and optimisation of net-shape metal forming processes with uncertainties”. In: *Computers & Structures* 90-91 (2012), pp. 13–27.
- [25] ISO 1:2002. *Geometrical Product Specifications (GPS) – Standard reference temperature for geometrical product specification and verification*. International Organization for Standardization, Geneva, 2002.
- [26] Dan Trietsch. “The Harmonic Rule for Process Setup Adjustment With Quadratic Loss”. In: *Journal of Quality Technology* 30 (1) (1998), pp. 75–84.
- [27] ISO 1101:2012/Cor 1:2013. *Geometrical product specifications (GPS) - Geometrical tolerancing - Tolerances of form, orientation, location and run-out*. International Organization for Standardization, Geneva, 2013.
- [28] M. M. Dowling et al. “Statistical Issues in Geometric Feature Inspection Using Coordinate Measuring Machines”. In: *Technometrics* 39 (1) (1997), pp. 3–17.
- [29] Christian Keck, Matthias Franke, and Heinrich Schwenke. “Werkstückeinflüsse in der Koordinatenmesstechnik (Workpiece Influence in Coordinate Metrology)”. In: *tm - Technisches Messen* 71 (2-2004) (2004), pp. 81–92.
- [30] K.D Summerhays et al. “Optimizing discrete point sample patterns and measurement data analysis on internal cylindrical surfaces with systematic form deviations”. In: *Precision Engineering* 26 (1) (2002), pp. 105–121.
- [31] P. Pedone, G. Vicario, and D. Romano. “Kriging-based sequential inspection plans for coordinate measuring machines”. In: *Applied Stochastic Models in Business and Industry* 25 (2) (2009), pp. 133–149.
- [32] Yueyang Du et al. “Measurement system for hot heavy forgings and its calibration”. In: *Optical Measurement Systems for Industrial Inspection VII*. SPIE, 2011, 80822Y–80822Y–11.
- [33] INSTITUT DR. FOERSTER GmbH & Co .KG. 2014. URL: <http://www.foerstergroup.de/> (visited on 01/28/2014).

CHAPTER 6. REFERENCES

- [34] Prueftechnik Dieter Busch AG. 2014. URL: <http://www.prueftechnik.com/> (visited on 01/28/2014).
- [35] Inc. OG Technologies. 2014. URL: <http://www.ogtechnologies.com/> (visited on 01/28/2014).
- [36] Danieli Automation. 2014. URL: <http://www.dca.it/> (visited on 01/28/2014).
- [37] Minteq International Inc. 2014. URL: <http://www.minteq.com/> (visited on 09/03/2015).
- [38] MERMEC S.p.A. 2014. URL: <http://www.mermecgroup.com/> (visited on 09/10/2015).
- [39] LIMAB. *LIMAB: Control by measurement*. 2015. URL: <http://http://www.limab.com> (visited on 09/07/2015).
- [40] NEXTSENSE GmbH. 2015. URL: <http://www.nextsense.at> (visited on 10/05/2015).
- [41] Zumbach Electronic AG. 2015. URL: www.zumbach.com (visited on 01/23/2015).
- [42] Johannes Bernstein. *Optisches Multi-Sensor-Messverfahren zur dimensionellen In-line-Messung von Strangprofilen im Fertigungsprozess*. Vol. Bd. 23. Berichte aus dem Lehrstuhl Qualitätsmanagement und Fertigungsmeßtechnik, Friedrich-Alexander-Universität Erlangen-Nürnberg. Aachen: Shaker, 2011. ISBN: 978-3844003451.
- [43] Yu-cun Zhang et al. “Measurement and control technology of the size for large hot forgings”. In: *Measurement* 49 (2014), pp. 52–59.
- [44] Xian-bin Fu, Bin Liu, and Yu-cun Zhang. “An optical non-contact measurement method for hot-state size of cylindrical shell forging”. In: *Measurement* 45 (6) (2012), pp. 1343–1349.
- [45] Jun He et al. “Measure dimension of rotating large hot steel shell using pulse laser on PRRR robot”. In: *Measurement* 45 (7) (2012), pp. 1814–1823.
- [46] Wei Liu et al. “Fast dimensional measurement method and experiment of the forgings under high temperature”. In: *Journal of Materials Processing Technology* 211 (2) (2011), pp. 237–244.
- [47] Youssef Bokhabrine et al. “3D characterization of hot metallic shells during industrial forging”. In: *Machine Vision and Applications* 23 (3) (2012), pp. 417–425.

-
- [48] Youssef Bokhabrine et al. “3D reconstruction of hot metallic surfaces for industrial part characterization”. In: *Machine Vision and Applications*. Vol. 23. 3. SPIE, 2010, pp. 417–425.
- [49] S.B Dworkin and T.J Nye. “Image processing for machine vision measurement of hot formed parts”. In: *Journal of Materials Processing Technology* 174 (1-3) (2006), pp. 1–6.
- [50] Dirk Stöbener et al. “Distance measurements with laser-triangulation in hot environments”. In: *XVII IMEKO World Congress*. 2003, pp. 1898–1902.
- [51] K. Määttä, J. Kostamovaara, and R. Myllylä. “Profiling of hot surfaces by pulsed time-of-flight laser range finder techniques”. In: *Applied Optics* 32 (27) (1993), pp. 5334–5347.
- [52] Zhenyuan Jia et al. “An improved image acquiring method for machine vision measurement of hot formed parts”. In: *Journal of Materials Processing Technology* 210 (2) (2010), pp. 267–271.
- [53] H. Huang, D. Gutchess, and T.-S. Chang. “Imaging Based In-Line Surface Defect Inspection for Bar Rolling: Iron & steel technology conference proceedings”. In: *AISTech*. 2004, pp. 717–728.
- [54] Heinrich Schwenke et al. “Optical Methods for Dimensional Metrology in Production Engineering”. In: *CIRP Annals - Manufacturing Technology* 51 (2) (2002), pp. 685–699.
- [55] A. Keith Turner. “What’s the Difference Among 2-D, 2.5-D, 3-D and 4-D?” In: *Applied Geoscience Forum* (1997), p. 54.
- [56] Jun Zhang et al. “Process adjustment with an asymmetric quality loss function”. In: *Journal of Manufacturing Systems* 33 (1) (2014), pp. 159–165.
- [57] ISO 10360-2:2010-06. *Geometrical product specifications (GPS) – Acceptance and reverification tests for coordinate measuring machines (CMM) – Part 2: CMMs used for measuring linear dimensions*. International Organization for Standardization, Geneva, 2010.
- [58] P. F. Bariani, Stefania Bruschi, and T. Dal Negro. “Prediction of nickel-base superalloys’ rheological behaviour under hot forging conditions using artificial neural networks”. In: *Journal of Materials Processing Technology* 152 (3) (2004), pp. 395–400.

CHAPTER 6. REFERENCES

- [59] Badrinarayan K. Belur and Ramana V. Grandhi. “Geometric deviations in forging and cooling operations due to process uncertainties”. In: *Journal of Materials Processing Technology* 152 (2) (2004), pp. 204–214.
- [60] S. K. Choi et al. “Optimization of open die forging of round shapes using FEM analysis”. In: *Journal of Materials Processing Technology* 172 (1) (2006), pp. 88–95.
- [61] Jonathan E. Makem, Hengan Ou, and Cecil G. Armstrong. “A virtual inspection framework for precision manufacturing of aerofoil components”. In: *Computer-Aided Design* 44 (9) (2012), pp. 858–874.
- [62] James A. Polyblank, Julian M. Allwood, and Stephen R. Duncan. “Closed-loop control of product properties in metal forming: A review and prospectus”. In: *Journal of Materials Processing Technology* 214 (11) (2014), pp. 2333–2348.
- [63] D. Recker, M. Franzke, and G. Hirt. “Fast models for online-optimization during open die forging”. In: *CIRP Annals - Manufacturing Technology* 60 (1) (2011), pp. 295–298.
- [64] Frank M. Gryna and J. M. Juran. *Quality planning and analysis: From product development through use*. 4th ed. McGraw-Hill series in industrial engineering and management science. Boston: McGraw-Hill, 2001. ISBN: 978-0070393684.
- [65] Bianca Maria Colosimo, Rong Pan, and Enrique Del Castillo. “Setup adjustment for discrete-part manufacturing processes with asymmetric cost functions”. In: *International Journal of Production Research* 43 (18) (2005), pp. 3837–3854.
- [66] D. Xu and S. L. Albin. “Manufacturing start-up problem solved by mixed-integer quadratic programming and multivariate statistical modelling”. In: *International Journal of Production Research* 40 (3) (2002), pp. 625–640.
- [67] Harriet Black Nembhard and John R. Birge. “A startup procedure for process industries using a multiple objective nonlinear program”. In: *IIE Transactions* 30 (4) (1998), pp. 291–300.
- [68] F. E. Grubbs. “An Optimum Procedure for Setting Machines or Adjusting Processes: (reprint)”. In: *Journal of Quality Technology* 15 (4) (1983), pp. 186–189.
- [69] D. Xu and S. L. Albin. *Comparison of Partial Least Squares Model and Response Surface Model in Optimizing Batch Settings*. 2004.
- [70] Nirmal Govind et al. *An Approach to Multivariate Bounded Process Adjustment*.

-
- [71] Liping Liu et al. “Research on Setup Adjustment Problem with Random Adjustment Error and Unknown Parameters”. In: *International Journal of Advancements in Computing Technology (IJACT)* 4 (17) (2012), pp. 360–367.
- [72] Zilong Lian and Enrique Del Castillo. “Setup adjustment under unknown process parameters and fixed adjustment cost”. In: *Journal of Statistical Planning and Inference* 136 (3) (2006), pp. 1039–1060.
- [73] Zilong Lian and Vanli, Arda, del Castillo, Enrique. “Setup Adjustment for Asymmetric Cost Functions Under Unknown Process Parameters”. In: *Quality Technology and Quantitative Management* 11 (4) (2014), pp. 471–489.
- [74] George Runger, Zilong Lian, and Enrique Del Castillo. “Optimal multivariate bounded adjustment”. In: *IIE Transactions* 42 (10) (2010), pp. 746–752.
- [75] S. P. Ladany. “Optimal set-up of a manufacturing process with unequal revenue from oversized and undersized items”. In: *Engineering Management Conference*. 1995, pp. 428–432.
- [76] C.-H. Chen and C.-Y. Chou. “Determining the Optimum Manufacturing Target Based on an Asymmetric Quality Loss Function”. In: *The International Journal of Advanced Manufacturing Technology* 21 (3) (2002), pp. 193–195.
- [77] Qiu Jin, Shaogang Liu, and Ping Wang. “Optimal tolerance design for products with non-normal distribution based on asymmetric quadratic quality loss”. In: *The International Journal of Advanced Manufacturing Technology* (2014).
- [78] C. C. Wu and G. R. Tang. “Tolerance design for products with asymmetric quality losses”. In: *International Journal of Production Research* 36 (9) (1998), pp. 2529–2541.
- [79] Box, G. E. P. and G. M. Jenkins. “Further contributions to adaptive quality control: Simultaneous estimation of dynamics: Non-zero costs”. In: *Proceedings of the ISI World Statistics Congresses*. Vol. 1963. 1963, pp. 943–974.
- [80] Stephen V. Crowder. “An SPC Model for Short Production Runs: Minimizing Expected Cost”. In: *Technometrics* 34 (1) (1992), pp. 64–73.
- [81] Liping Liu, Yizhong Ma, and Yiliu Tu. “Multivariate setup adjustment with fixed adjustment cost”. In: *International Journal of Production Research* 51 (5) (2013), pp. 1392–1404.
- [82] Dan Trietsch. “The Five-Ten Rule: A constrained-Loss Economic Process Adjustment Procedure”. In: *Quality Engineering* 10 (1) (1997), pp. 85–95.

CHAPTER 6. REFERENCES

- [83] Dan Trietsch. “Process setup adjustment with quadratic loss”. In: *IIE Transactions* 32 (4) (2000), pp. 299–307.
- [84] Alexander Schöch et al. “Fast measurement of freeform parts at elevated temperature using laser-triangulation principle”. In: *11th IMEKO TC14 Symposium on Laser Metrology for Precision Measurement and Inspection in Industry, LMPMI*. 2014, pp. 174–178.
- [85] Alexander Schöch et al. “High-Speed Measurement of Complex Shaped Parts at Elevated Temperature by Laser Triangulation”. In: *International Journal of Automation Technology* 9 (9) (2015), pp. 558–566.
- [86] Alexander W. Koch. *Optische Messtechnik an technischen Oberflächen: Praxisorientierte lasergestützte Verfahren zur Untersuchung technischer Objekte hinsichtlich Form, Oberflächenstruktur und Beschichtung ; mit 4 Tabellen und 418 Literaturstellen*. Renningen-Malmsheim: Expert-Verl., 1998. ISBN: 9783816913726.
- [87] Optris GmbH. 2015. URL: <http://www.optris.de> (visited on 04/19/2015).
- [88] Z. Zhang. “A flexible new technique for camera calibration”. In: *IEEE Transactions on Pattern Analysis and Machine Intelligence* 22 (11) (2000), pp. 1330–1334.
- [89] Richard Hartley and Andrew Zisserman. *Multiple view geometry in computer vision*. 2nd ed. Cambridge, UK and New York: Cambridge University Press, 2003. ISBN: 0521540518.
- [90] R. Tsai. “A versatile camera calibration technique for high-accuracy 3D machine vision metrology using off-the-shelf TV cameras and lenses”. In: *IEEE Journal on Robotics and Automation* 3 (4) (1987), pp. 323–344.
- [91] Jeffrey J. McConnell. *Computer graphics: Theory into practice*. Boston: Jones and Bartlett Publishers, 2006. ISBN: 9780763722500.
- [92] Luc Van Gool and Gabor Szekely. *Computer Vision and Visual Inspection script*. 2009.
- [93] Duane C. Brown. “Close-range camera calibration”. In: *Photogrammetric Engineering* 37 (8) (1971), pp. 855–866.
- [94] Klaus Frick and Claudio Wolfer. *Camera Calibration Algorithm of a PMM80 System*. 2014.
- [95] H. C. Longuet-Higgins. “A computer algorithm for reconstructing a scene from two projections”. In: *Nature* 293 (5828) (1981), pp. 133–135.

-
- [96] R. B. Fisher and D. K. Naidu. “A Comparison of Algorithms for Subpixel Peak Detection”. In: *Image Technology*. Ed. by Jorge L. C. Sanz. Springer Berlin Heidelberg, 1996, pp. 385–404. ISBN: 978-3-642-63528-1.
- [97] Aqsense. 2015. URL: <http://www.aqsense.com/> (visited on 02/27/2015).
- [98] AIA Global Association For Vision Information. *GigE Vision® Specification*. 2013.
- [99] Albert Weckenmann et al. “Multisensor data fusion in dimensional metrology”. In: *CIRP Annals - Manufacturing Technology* 58 (2) (2009), pp. 701–721.
- [100] Yang Chen and Gérard Medioni. “Object modelling by registration of multiple range images”. In: *Image and Vision Computing* 10 (3) (1992), pp. 145–155.
- [101] H. von Weingraber. “Über die Eignung des Hüllprofils als Bezugslinie für die Messung der Rauheit”. In: *CIRP Annals - Manufacturing Technology* 5 (1956), pp. 116–128.
- [102] H. Edelsbrunner, D. Kirkpatrick, and R. Seidel. “On the shape of a set of points in the plane”. In: *IEEE Transactions on Information Theory* 29 (4) (1983), pp. 551–559.
- [103] X. Jane Jiang and David J. Whitehouse. “Technological shifts in surface metrology”. In: *CIRP Annals - Manufacturing Technology* 61 (2) (2012), pp. 815–836.
- [104] Harry Blum and Weiant Wathen-Dunn. “A Transformation for Extracting New Descriptors of Shape”. In: *Models for the Perception of Speech and Visual Form* (1967), pp. 362–380.
- [105] B. Delaunay. “Sur la sphere vide.” In: *Akad. Nauk SSSR, Otdelenie Matematicheskii i Estestvennyka Nauk* 7 (1934), pp. 793–800.
- [106] Chua Chee Kai, Gan G. K. Jacob, and Tong Mei. “Interface between CAD and Rapid Prototyping systems. Part 2: LMI – An improved interface”. In: *The International Journal of Advanced Manufacturing Technology* 13 (8) (1997), pp. 571–576.
- [107] Peter Shirley and Steve Marschner. *Fundamentals of computer graphics*. 3rd ed. Natick, Mass.: A K Peters/CRC Press, 2009. ISBN: 978-1568814698.
- [108] Xin Chen and Jie Shen. “A Tetrahedral Mesh Generation Algorithm from Medical Images”. In: *2008 International Symposium on Information Science and Engineering (ISISE)*. 2008, pp. 414–417.

CHAPTER 6. REFERENCES

- [109] Chandrajit L. Bajaj, Edward J. Coyle, and Kwun-Nan Lin. “Arbitrary Topology Shape Reconstruction from Planar Cross Sections”. In: *Graphical Models and Image Processing* 58 (6) (1996), pp. 524–543.
- [110] Nina Amenta, Sunghee Choi, and Ravi Krishna Kolluri. “The power crust”. In: *the sixth ACM symposium*. Ed. by David C. Anderson and Kunwoo Lee. 2001, pp. 249–266.
- [111] F. Bernardini et al. “The ball-pivoting algorithm for surface reconstruction”. In: *IEEE Transactions on Visualization and Computer Graphics* 5 (4) (1999), pp. 349–359.
- [112] Michael Kazhdan, Matthew Bolitho, and Hugues Hoppe. “Poisson Surface Reconstruction”. In: *Proceedings of the Fourth Eurographics Symposium on Geometry Processing*. SGP '06. Eurographics Association, 2006, pp. 61–70. ISBN: 3-905673-36-3.
- [113] Jha Kailash. “A New Method for Reconstruction of Smooth Branching Surface from Contours”. In: *International Journal of CAD/CAM* 12 (1) (2012).
- [114] Amit Bermano, Amir Vaxman, and Craig Gotsman. “Online reconstruction of 3D objects from arbitrary cross-sections”. In: *ACM Transactions on Graphics* 30 (5) (2011), pp. 1–11.
- [115] Robert W. Brown et al. *Magnetic resonance imaging: Physical principles and sequence design*. Second edition. 2014. ISBN: 978-0471720850.
- [116] B. G. Bang and F. B. Bang. “Graphic reconstruction of the third dimension from serial electron microphotographs”. In: *Journal of Ultrastructure Research* 1 (2) (1957), pp. 138–146.
- [117] Winfried Denk and Heinz Horstmann. “Serial block-face scanning electron microscopy to reconstruct three-dimensional tissue nanostructure”. In: *PLoS biology* 2 (11) (2004), e329.
- [118] Leonardo De Chiffre et al. “Industrial applications of computed tomography”. In: *CIRP Annals - Manufacturing Technology* 63 (2) (2014), pp. 655–677.
- [119] Ying-Cheng Chen et al. “A reliable surface reconstruction system in biomedicine”. In: *Computer methods and programs in biomedicine* 86 (2) (2007), pp. 141–152.
- [120] Ming-Yu Shih and Din-Chang Tseng. “Versatile surface model reconstruction from serial planar contours”. In: *22nd Annual International Conference of the IEEE Engineering in Medicine and Biology Society*. 2000, pp. 2910–2913.

-
- [121] David Meyers, Shelley Skinner, and Kenneth R. Sloan. “Surfaces from contours”. In: *ACM Transactions on Graphics* 11 (3) (1992), pp. 228–258.
- [122] E. Keppel. “Approximating Complex Surfaces by Triangulation of Contour Lines”. In: *IBM Journal of Research and Development* 19 (1) (1975), pp. 2–11.
- [123] Henry Fuchs, Zvi M. Kedem, and Samuel P. Uzelton. “Optimal surface reconstruction from planar contours”. In: *Communications of the ACM* 20 (10) (1977), pp. 693–702.
- [124] Soo-Won Chae and Gyu-Min Lee. “Volume triangulation from planar cross sections”. In: *Computers & Structures* 72 (1-3) (1999), pp. 93–108.
- [125] H. N. Christiansen and T. W. Sederberg. “Conversion of complex contour line definitions into polygonal element mosaics”. In: *SIGGRAPH '78 Proceedings of the 5th annual conference on Computer graphics and interactive techniques*. Ed. by S. H. Chasen and R. L. Phillips. 1978, pp. 187–192.
- [126] S. Ganapathy and T. G. Dennehy. “A new general triangulation method for planar contours”. In: *SIGGRAPH '82 Proceedings of the 9th annual conference on Computer graphics and interactive techniques*. Ed. by R. Daniel Bergeron. 1982, pp. 69–75.
- [127] Gill Barequet and Micha Sharir. “Piecewise-Linear Interpolation between Polygonal Slices”. In: *Computer Vision and Image Understanding* 63 (2) (1996), pp. 251–272.
- [128] Gill Barequet, Daniel Shapiro, and Ayellet Tal. “History Consideration in Reconstructing Polyhedral Surfaces from Parallel Slices”. In: *Proceedings of the 7th Conference on Visualization '96. VIS '96*. IEEE Computer Society Press, 1996, 149–ff. ISBN: 0-89791-864-9.
- [129] T. Todd Elvins. “A survey of algorithms for volume visualization”. In: *ACM SIGGRAPH Computer Graphics* 26 (3) (1992), pp. 194–201.
- [130] Herb Sutter. “The free lunch is over: A fundamental turn toward concurrency in software”. In: *Dr. Dobb's Journal* 30 (3) (2005).
- [131] Scilab Enterprises. *Scilab: Free and Open Source software for numerical computation*. Orsay, France, 2012.
- [132] Inc. The MathWorks. *MATLAB Release 2015a*. Natick, Massachusetts, United States, 2015.

CHAPTER 6. REFERENCES

- [133] Mark Tratnig et al. “Positional and orientational referencing of multiple light sectioning systems for precision profile measurement”. In: *Electronic Imaging 2005*. SPIE Proceedings. SPIE, 2005, pp. 74–85.
- [134] Weiguang Zhang. “Multiresolution three-dimensional measurement system with multiple cameras and light sectioning method”. In: *Optical Engineering* 49 (12) (2010).
- [135] GOM - Gesellschaft für Optische Messtechnik mbH. *GOM Inspect*. 2015. (Visited on 10/06/2015).
- [136] JCGM 100. *Evaluation of measurement data – Guide to the expression of uncertainty in measurement*. Bureau international des poids et mesures, Sèvres, 2008.
- [137] Frank Chen, Gordon M. Brown, and Mumin Song. “Overview of three-dimensional shape measurement using optical methods”. In: *Optical Engineering* 39 (1) (2000), p. 10.
- [138] Nikola Vukašinović, Marjan Korošec, and Jože Duhovnik. “The Influence of Surface Topology on the Accuracy of Laser Triangulation Scanning Results”. In: *Journal of Mechanical Engineering* 2010 (1) (2010), pp. 23–30.
- [139] Simone Carmignato et al. “Experimental study on performance verification tests for coordinate measuring systems with optical distance sensors”. In: *Three-Dimensional Imaging Metrology*. Vol. 7239. SPIE Proceedings. SPIE, 2009.
- [140] Alessandro Voltan. “Metrological performance verification of optical coordinate measuring systems”. Dissertation. Padua, Italy: University of Padua, 2010.
- [141] Tilo Pfeifer and Robert Schmitt. *Fertigungsmesstechnik*. 3., überarb. und erw. Aufl. München: Oldenbourg, 2010. ISBN: 3486592025.
- [142] DIN 1333. *Presentation of numerical data*. German Institute for Standardization, Berlin, 1992.
- [143] IEEE 754-2008. *IEEE Standard for Floating-Point Arithmetic*. Piscataway, NJ, USA, 2008.
- [144] IEC 60751:2008. *Industrial platinum resistance thermometers and platinum temperature sensors*. International Electrotechnical Commission, Geneva.
- [145] DIN EN 60751:2009-05. *Industrielle Platin-Widerstandsthermometer und Platin-Temperatursensoren (IEC 60751:2008); Deutsche Fassung EN 60751:2008*. German Institute for Standardization, Berlin.

-
- [146] P. E. Ciddor. “Refractive index of air: new equations for the visible and near infrared”. In: *Applied Optics* 35 (9) (1996), pp. 1566–1573.
- [147] Bengt Edlén. “The Refractive Index of Air”. In: *Metrologia* 2 (2) (1966), pp. 71–80.
- [148] K. P. Birch and M. J. Downs. “An Updated Edlén Equation for the Refractive Index of Air”. In: *Metrologia* 30 (3) (1993), p. 155.
- [149] K. P. Birch and M. J. Downs. “Correction to the Updated Edlén Equation for the Refractive Index of Air”. In: *Metrologia* 31 (4) (1994), p. 315.
- [150] J. A. Stone and J. H. Zimmerman. *Engineering Metrology Toolbox*. 2011.
- [151] Alessandro Salvadori. “Modellazione degli errori e studio dell’asse di movimentazione per un sistema di misura senza contatto per pezzi ad alta temperatura”. Master’s thesis. Padua, Italy: University of Padua, 2014.
- [152] F. Cverna. *ASM Ready Reference: Thermal properties of metals*. ASM Ready Reference Series. ASM International, 2002. ISBN: 9780871707680.
- [153] Edgar Dietrich and Michael Radeck. *Prüfprozesseignung nach VDA 5 und ISO 22514-7*. 1. Aufl. Pocket power. München: Hanser, 2015. ISBN: 3446443770.
- [154] Timothy A. Clarke et al. “Laser-based triangulation techniques in optical inspection of industrial structures”. In: *Optical Testing and Metrology III: Recent Advances in Industrial Optical Inspection*. SPIE Proceedings. SPIE, 1991, pp. 474–486.
- [155] Schott AG. 2015. URL: www.schott.com (visited on 10/15/2015).
- [156] Inc. Ansys. *ANSYS v.15*.
- [157] ISO/TS 23165:2006. *Geometrical Product Specifications (GPS) – Guidelines for the Evaluation of Coordinate Measuring Machine (CMM) Test Uncertainty*. International Organization for Standardization, Geneva, 2006.
- [158] Enrico Savio. “Uncertainty in testing the metrological performances of coordinate measuring machines”. In: *CIRP Annals - Manufacturing Technology* 55 (1) (2006), pp. 535–538.
- [159] A. K. Sahoo, M. K. Tiwari, and A. R. Mileham. “Six Sigma based approach to optimize radial forging operation variables”. In: *Journal of Materials Processing Technology* 202 (1-3) (2008), pp. 125–136.
- [160] Zakaria Allam et al. “Forging Process Control: Influence of Key Parameters Variation on Product Specifications Deviations”. In: *Procedia Engineering* 81 (2014), pp. 2524–2529.

CHAPTER 6. REFERENCES

- [161] TRANSVALOR S.A. *Forge 2011*.
- [162] P. F. Bariani and Stefania Bruschi. “Modelling the forging and post-forging cooling of C70S6 conrods”. In: *Journal of Materials Processing Technology* 167 (2-3) (2005), pp. 529–535.
- [163] P. F. Bariani, Stefania Bruschi, and T. Dal Negro. “Integrating physical and numerical simulation techniques to design the hot forging process of stainless steel turbine blades”. In: *International Journal of Machine Tools and Manufacture* 44 (9) (2004), pp. 945–951.
- [164] Albert Weckenmann and M. Rinnagl. “Acceptance of processes: do we need decision rules?” In: *Precision Engineering* 24 (3) (2000), pp. 264–269.
- [165] María Villeta et al. “An alternative method to achieve metrological confirmation in measurement process”. In: *The 4th Manufacturing Engineering Society International Conference (MESIC 2011)*. AIP Conference Proceedings. AIP, 2012, pp. 181–188.
- [166] María Villeta et al. “New criterion for evaluating the aptitude of measurement systems in process capability determination”. In: *The International Journal of Advanced Manufacturing Technology* 50 (5-8) (2010), pp. 689–697.
- [167] Zilong Lian, Bianca Maria Colosimo, and Enrique del Castillo. “Setup Adjustment of Multiple Lots Using a Sequential Monte Carlo Method”. In: *Technometrics* 48 (3) (2006), pp. 373–385.
- [168] Enrique Del Castillo, Rong Pan, and Bianca Maria Colosimo. “A unifying view of some process adjustment methods”. In: *Journal of Quality Technology* 35 (3) (2003), p. 286.
- [169] Rong Pan and Enrique Del Castillo. “Scheduling methods for the statistical setup adjustment problem”. In: *International Journal of Production Research* 41 (7) (2003), pp. 1467–1481.
- [170] Christopher M. Bishop. *Pattern recognition and machine learning*. Information science and statistics. New York: Springer, 2006. ISBN: 9780387310732.
- [171] Genichi Taguchi, A. Elsayed, and Thomas C. Hsiang. *Quality engineering in production systems*. McGraw-Hill series in industrial engineering and management science. New York: McGraw-Hill, 1989. ISBN: 9780070628304.
- [172] T. Lindeberg. “Scale-space for discrete signals”. In: *IEEE Transactions on Pattern Analysis and Machine Intelligence* 12 (3) (1990), pp. 234–254.

-
- [173] Jeffrey C. Lagarias et al. “Convergence Properties of the Nelder–Mead Simplex Method in Low Dimensions”. In: *SIAM Journal on Optimization* 9 (1) (1998), pp. 112–147.
- [174] Ronald Cools. “Advances in multidimensional integration”. In: *Journal of Computational and Applied Mathematics* 149 (1) (2002), pp. 1–12.
- [175] ISO 14253-1:2013. *Geometrical product specifications (GPS) - Inspection by measurement of workpieces and measuring equipment – Part 1: Decision rules for proving conformity or nonconformity with specifications*. International Organization for Standardization, Geneva, 2013.
- [176] Denis Choquet, Pierre L’Ecuyer, and Christian Léger. “Bootstrap confidence intervals for ratios of expectations”. In: *ACM Transactions on Modeling and Computer Simulation* 9 (4) (1999), pp. 326–348.